Title
Pervasive Health Monitoring

Author
Naima, Reza

Publication Date
2012

Pervasive Health Monitoring

by

Reza Naima

A dissertation submitted in partial satisfaction of the

requirements for the degree of

Joint Doctor of Philosophy
with the University of California, San Francisco

in

Bioengineering

in the

Graduate Division

of the

University of California, Berkeley

Committee in charge:

Professor John F. Canny, Chair
Professor Greg Niemeyer
Professor David Saloner

Fall 2012

Pervasive Health Monitoring

Abstract

Pervasive Health Monitoring

by

Reza Naima

Doctor of Philosophy in Bioengineering

University of California, Berkeley

Professor John Canny, Chair

Pervasive health monitoring is the application of non-invasive ambulatory monitoring technologies towards continuous physiologic monitoring. These technologies can be used for the detection of sudden, acute, health problems and the management of chronic disease. For people at risk for specific incidents, such as a heart attack in an individual with heart disease or a fall from an elderly individual, being able to detect a potentially life threatening incident and alerting a care provider can mean the difference between life and death. Likewise, individuals who have chronic health conditions, such as congestive heart failure, can benefit from tracking the progress of their disease. Feedback provided from an ambulatory monitor can be used to help manage the treatment of the disease with the goal of keeping the individual out of the hospital. Currently, people wait until a health problem manifests itself in a way which necessitates a visit to a doctor or a hospital. This type of management is the antithesis of early detection. Often, many conditions have simpler, more effective, and less costly treatments if detected and diagnosed at an early stage. Not only does this result in a better quality of life, but can help to by reducing the costs to the healthcare system. In 2010, U.S. healthcare costs were $2.6 trillion, and it is expected to grow to an incredible $4.6 trillion by 2020.

In order to enable a wide range of pervasive monitoring applications, a highly integrated ambulatory physiologic monitor was developed and used in a number of studies. The hardware platform is called *The Berkeley Tricorder*, and is capable of acquiring a high resolution data from a number of physiologic sensors including an electrocardiograph, an electromyography, a photoplethysmograph, a bioimpedance spectrometer, and an accelerometer. In addition, *The Berkeley Tricorder* is capable of storing data on an SD memory card, or transmitting it wirelessly over Bluetooth to a local target, or to a remote target using the dial-up-networking Bluetooth profile and a mobile phone. The latest version of the hardware measures 1.4”x1.85”.

The first chapter explores a number of acute and chronic health conditions to better understand which physiologic monitors are of the most value in an ambulatory system. Next, the physiologic basis of the biosignals are examined, along with the technology which enables their measurement. Based on the methodology used to measure the biosignals, a detailed set of requirements for the implementation of the ambulatory monitor is derived. The requirements are then translated into a physical implementation along with a set of lessons learned along the way. The hardware is then examined to see how it compares to the original design and to quantify its signal quality. Finally, a study used to explore the physiology of stress is using the ambulatory monitor is discussed.

Contents

List of Figures

List of Tables

Abbreviations

-3dB	-3dB Cuttoff frequency
ADC	Analog to Digital Converter
ADL	Activities of Daily Living
AF	Atrial Fibrillation
AFE	Analog Front End
ANS	Autonomic Nervous System
API	Application Programming Interface
BGA	Ball Grid Array
bioZ	Bioimpedance
BioZ	Bioimpedance
BJT	Bipolar Junction Transistor
BP	Blood Pressure
BW	Bandwidth
CHF	Congestive Heart Failure
CMRR	Common-Mode Rejection Ratio
COPD	Chronic Obstructive Pulmonary Diease
DAC	Digital to Analog Converter
DB9	D-suBmnituature 9-Pin
DLP	Digital Light Processing
DPST	Double Pole, Single Throw
DUN	Dial-Up-Networking
ECG	Electrocardiogram
EDA	Electrodermal Activity
EDC	Electrodermal Conductivity
EDR	Electrodermal Response
EEG	Electroencephalograph
EMG	Electromyogram
EMI	Electromagnetic Interference
EOG	Electrooculography
FET	Field-Effect Transistor
FEV1	percentage of predicted Forced Expiratory Volume in 1 second
GI	Gastro-Intestinal
GPIB	IEE-488 General Purpose Interface Bus
GPS	Global Positioning System
Hb	deoxygenated Hemoglobin
$\mathbf{HbO_2}$	oxygenated Hemoglobin
HPF	High-Pass Filter
HR	Heart Rate
HRV	Heart Rate Variablity
$\mathbf{I^2C}$	Inter-Integrated Circuit
I/O	Input/Output
IC	Integrated Circuit

IR	Infra-Red
LED	Light-Emitting Diode
LiPo	Litihum-Polymer Ion
LPF	Low-Pass Filter
MCU	Microcontroller
MEMS	Microelectromechanical Systems
MI	Myocardial Infarction
NICU	Neonatal Intensive Care Unit
OSA	Obstructive Sleep Apnea
PANA	Positive Affect and Negative Affect
PC	Personal Computer
PCB	Printed Circuit Board
PNS	Parasympathetic Nervous System
POTS	Plain Old Telephone System
PPG	Photoplethysmograph
PSD	Power Spectral Density
PTT	Pulse Transit Time
REM	Random Eye Movement
RF	Radio-Frequency
RFI	Radio Frequency Interference
RIP	Respiratory Inductive Plethysmography
RSA	Respiratory sinus arrhythmia
SD	Secure Digital
SEM	Standard Error of the Mean
SIDS	Sudden Infant Death Syndrome
SNR	Signal to Noise Ratio
SNS	Sympathetic Nervous System
SPI	Serial Peripheral Interface
SpO$_2$	Oxygen Saturation Percentage
STAI	State Trait Anxiety Inventory
TIA	Transimpedance Amplifier
TNS-α	Tumor Necrosis Factor Alpha
TSST	Trier Social Stress Test
UML	Unified Modeling Language
VF	Ventricular Fibrillation
VT	Ventricular Tachycardia
WPS	WiFi-Based Positioning System

Chapter 1

Introduction

Pervasive health monitoring refers to the technologies and practices involving the collection of physiological metrics through non-invasive means continuously or at a much higher frequency than normally collected. Pervasive health monitoring presents a fundamental paradigm shift in healthcare. Traditionally, one's health is managed by spot-checking vitals during routine checkups which are very infrequent or by waiting until a health problem necessitates a visit to a physician or emergency room. With spot-checking vitals, only a small set of health problems can be detected. And many health problems that result in a physician or hospital visit can be avoided with early detection.

Pervasive health monitoring technologies can address these issues by continuously monitoring a range of vitals for early detections of asymptomatic conditions which would not show up during a routine checkup. Additionally, by providing early warning of impending serious conditions, it allows for treatment in the early stages of a disease which often allows for simpler management options.

Aspects of pervasive health monitoring exist in contemporary healthcare, but only as a means of diagnosing conditions which can not be diagnosed through a visit to a physician. The most common example is that of a patient who suffers infrequent chest pain or episodes of presyncope. In these cases, a Holter monitor is connected to the patient to continuously record the patient's electrocardiographic signal with the goal of recording the infrequent arrhythmia and aid in diagnosis. Another common example is that of a sleep lab where a range of physiological instrumentation is connected to the patient to detect problems that occur only while asleep such as sleep apnea. In both these cases, the purpose of the monitoring is to provide a diagnosis, and the duration of the monitoring is limited to the point at which a diagnosis can be made.

In the true sense of pervasive monitoring, continuous monitoring offers the potential to detect arrhythmias or sleep apnea well before the patient feels any symptoms, track the progress of the conditions over time and evaluate the efficacy of various treatments.

Early detection of health conditions does not only have the potential for improving the quality of life, but it also has the potential to provide a solution to the healthcare crisis in the United States and abroad. In 2010, the healthcare costs in the US were $2.6 trillion (17.6% of GDP) and are expected to reach $4.6 trillion (19.8% GDP) by 2020 (figure 1.1). The incredible growth in the cost of healthcare is fueled by a combination of a rapidly increasing elderly population and advancements in costly technologies that allow the elderly to live longer lives. Pervasive monitoring technologies offers to combat this trend by allowing for preventative care through early detec-

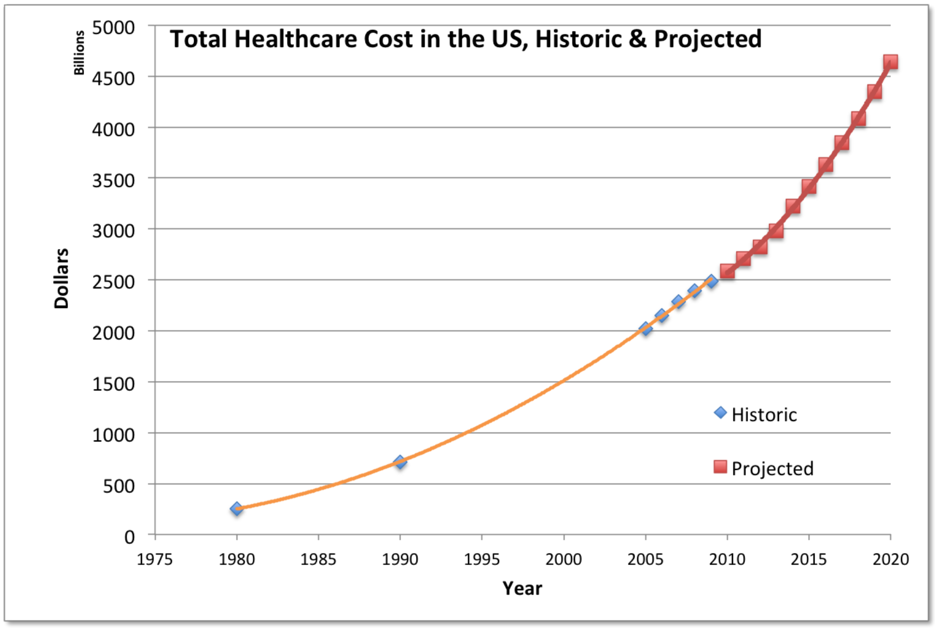

Figure 1.1: Total Healthcare Cost in the US, Historic & Projected. Data from the Centers for Medicare & Medicaid Services.

tion, disease diagnosis and management of care through telemedicine, and in-home monitoring for chronic conditions and the elderly.

Beyond traditional modalities of physiological monitoring, pervasive monitoring enables new paradigms such as the ability to continually monitor stress levels. Stress has been linked to a myriad of health problems including cardiovascular disease, inflammatory disease, and mental health issues. Traditionally, this is performed by a physician asking the patient for their perceived stress level. By continuously monitoring a number of physiological parameters, a stress metric can be derived which can be used to correlate stress to the activities and location of the patient. This type of objective feedback can be quite powerful in helping reduce stress for the patient.

In developing countries, thousands of people die each year due to lack of proper healthcare. This is especially true in remote rural areas where rapid transportation to a hospital is not available. For example, in India, 75% of the healthcare infrastructure is located in urban areas, whereas 73% of the population live in rural areas. Consequently, incidence of disease is double in rural areas as compared to urban areas[91]. A robust, low cost, multi-modal health monitor capable of remote telemetry through the near ubiquitous cellular network can enhance telemedicine in these regions.

There are quite a few applications of pervasive health monitoring technologies. When this project was initially started, the motivation was remote monitoring of elderly patients, but the project expanded and evolved over the years. The following sections describe the various use cases that were considered in designing *The Berkeley Tricorder*.

1.1 Chronic Monitoring

Once it is known that problem/disease exists, monitoring it's condition and providing that information in the form of feedback to the user or to the care provider can be invaluable. Based on the information, the care provider can alter medications, or initiate new/different treatments.

The ability to detect a problem at an early stage typically makes it much more treatable than later detection. The benefits are to both the patient in terms of quality of life as well as the healthcare system as it is typically less costly to provide early treatment.

Additionally, for a number of diseases, there are signs that one needs to monitor which would require immediate attention. An example of this would be patients with Congestive Heart Failure (CHF) which exhibit an increase in fluid volume. Early detection of this condition is easily treatable with medication; left untreated, a life threatening condition can manifest requiring hospitalization.

Immediate telemetry of the diagnosis is not required in most cases; rather, it is sufficient to gather data over a period of time and do offline analysis for any problems or to provide a summary of the data to the care provider. Even in the case of patients with CHF and fluid overload, a several hour delay in treatment is not critical - though a several day delay is.

1.1.1 Cardiovascular Disease

Cardiovascular disease is the #1 killer in the United States, responsible for 36% of all deaths[125], or one death every 37 seconds[126]. Furthermore, from [56, 125, 126] :

- 73 million Americans have high blood pressure, with a 50% prevalence in Americans over 45.
- 16 million Americans have coronary heart disease.
- 5.3 million Americans have heart failure, with a 20% lifetime risk of developing the condition by the age of 40.
- 789,000 new heart attacks will occur each year.

Continuous monitoring for a number for these high-risk populations can provide an early warning resulting in early treatment which can minimize the severity of the disease/attack and even possibly save the individual's life. For example, before experiencing a myocardial infarction (aka heart attack), an individual will often experience a condition referred to as an ST elevation. An ST elevation results from damage or inflammation of the cardiac tissue resulting in alteration in the electrical properties of the tissue and subsequently, premature ending of the systole period of an heart beat. Early detection of ST elevation from a continuous ECG monitor can lead to more rapid treatment, and thus less damage to the heart from the infarct.

Ventricular Fibrillation (VF) is a condition where the heart experiences disorganized electrical activity in the ventricle, and is no longer able to pump blood to the body. A defibrillator is used in this situation to reset the electrical activity of the heart, otherwise an individual can die in just a few minutes. Often times, VF are preceded by a period referred to as VT. An individual remain in VT for up to 24 hours before experiencing a life threatening VF. Thus, early detection of VT can lead to treatment to mitigate an episode of VF. And in the case where there is a support staff nearby, detection of VF can illicit a rapid life-saving response.

AF is like VF, but occurs in the atrium. Blood can still be pumped to the rest of the body, but inefficiently. However, the erratic contractions of the atrium can result in blood clot formations which can travel to the brain and cause a stroke, to the leg to cause deep vein thrombosis, or even back into the coronary arteries to cause an infarct. Early detection of this condition can result in treatment to alleviate the condition.

Beyond these conditions, many other types of arrhythmias can be detected. The detection of asymptomatic arrhythmia is the impetus behind the creation of the ambulatory Holter monitor, one of the first ambulatory monitors used for the diagnosis of heart disease. Thus, and ECG is an invaluable addition to any ambulatory health monitor.

Blood Pressure

Ninety percent of individuals over 60 years of age will develop hypertension[127]. It is possible to noninvasively monitor relative blood pressure in individuals for feedback and management of the disease by measuring a metric called PTT. When the heart contracts, a pulse wave is generated and travels down the arteries to the rest of the body. The velocity of this pulse wave is dependent on the elasticity of the arteries, which become more stiff as the blood pressure increases. Thus, by measuring the pulse wave velocity, one can derive a relative value for blood pressure. This measurement can be made with a Doppler ultrasound, but a simpler technique only requires measurement of the time between the ventricular contraction (the *R-wave* in figure 2.5b) and the arrival of the pulse wave at a distal location. A PPG (section 2.2) located on the body can detect the arrival of the pulse wave, and thus can be used to compute the pulse wave velocity by computing the ratio of the distance between the heart and the location of the PPG and the time between the measurement of the *R-wave* and the peak of the PPG signal.

1.1.2 Chronic Obstructive Pulmonary Disease

Chronic Obstructive Pulmonary Diease (COPD) encompasses a class of diseased (such as emphysema and chronic bronchitis) which result in inflammation and scarring of the lungs, reducing airflow. According to the World Health Organization, COPD is the 5th most common cause of death, and the 10th most burdensome disease worldwide[38]. The prevalence of COPD was found to be over 10% globally through an international 12-site study[18].

Early detection of COPD exacerbations[1] have been associated with faster recovery times and reduced hospitalizations. Additionally patients who reported more more exacerbations to their care provider experienced a higher quality of life[123]. For late stage COPD[2] patients, monitoring of blood oxygen (SpO_2) becomes important, and would require immediate attention.

1.1.3 Stress Monitoring

It is generally agreed upon that chronic stress is detrimental to one's health. However, most people would be surprised at the range of physical and mental problems that have been associated to extended periods of stress. Chronic stress has been associated with cardiovascular disease, cancer, diabetes, infection diseases and immune system dysregulation[22, 30, 31]. Additionally, there is

---

[1] The author defines exacerbations as an increase in dyspnea, sputum purulence, or sputum amount.

[2] When percentage of predicted Forced Expiratory Volume in 1 second (FEV1) < 40%, respiratory failure is indicated, or right heart failure

strong evidence linking stress with a range of mental diseases such as depression, anxiety, and schizophrenia [33]. For additional background on this topic, please consult section 6.1.

It would be advantageous to continually monitor stress levels for a number of reasons. For people with conditions which are worsened by stress, such as Chron's disease or inflammatory bowel disease[22, 77, 79], having a system that can track stress throughout the day can be used to help train the individual how to avoid stress. Such as system could track stress over the course of days tracking both geographic location and time of day in order to provide feedback about activities in the daily life of an individual were most stressful. Such a device can also track instantaneous stress levels and trigger an alert to the individual that they modulate their stress levels. Such a system could incorporate methodologies by which to directly reduce stress - such as prompting the individual to play a game on their smartphone.

Many systems have been developed in order to help quantify stress and emotion [13, 28, 54, 60, 69, 75, 92]. The typical approach is to measure a number of physiologic parameters and attempt a correlation between the physiologic data and a ground truth of stress. The ground truth can consist of measured stress hormones such as cortisol, through well-established stress induction techniques such as the *Trier Social Stress Test*[62], or through self-report from the subject.

Although just about any metric can be used for developing a subjective stress score – from eye blink rate to speech pattern analysis – the most effective measures of stress are those affected by the sympathetic branch of the Autonomic Nervous System (ANS) responsible for the fight or flight response. These include a number of non-invasive metrics such as Heart Rate (HR), HRV[3], Electrodermal Activity (EDA)[4], and respiration patterns.

The system would also need to be able to distinguish between stress induced activation of the Sympathetic Nervous System (SNS) as compared to increase in heart rate through exercise. As discussed in section 1.1.4, an accelerometer can help distinguish physical activity and thus would be of use in such a system.

A telemetry system would also be required to communicate the information to a display. The near-ubiquitous smartphone is an ideal target for a display, and a low-powered Bluetooth transmitter can be used to communicate data to the smartphone. Additionally, the Global Positioning System (GPS) and WiFi-Based Positioning System (WPS) based systems in a smartphone can be used to complement the stress data by attempting to map stress levels to locations, such as work or locations of traffic congestion.

1.1.4 Activity Monitoring

Physical activity has been demonstrated to be critical for the physical and mental well being of elderly individuals[17]. There has been significant research in different forms of interventions to increase the level of physical activity in the elderly[61]. For individuals not actively involved in some form of physical intervention, it would be of great value to evaluate their level of physical activity as a form of feedback to themselves as a motivator and to their healthcare provider. There are numerous commercial devices on the market to for tracking activity (figure 1.2) which underlies the importance of this metric. All these devices work using only an accelerometer.

---

[3] HRV is derived from a frequency analysis of the HR, and optionally of the respiration signal. HRV is further discussed in section 6.3.3.

[4] EDA is a measure of the conductivity of the skin as a result of sweat production, and is further discussed in section 2.4.

(a) Fitbit (b) Jawbone UP (c) Nike Fuelband

Figure 1.2: Examples of commercially available activity monitors

Beyond simply gauging activity, a body-worn accelerometer has a number of other advantages. It is also possible to use an accelerometer to detect the type of activity being performed[78, 86], such as sitting, walking, going up stairs, etc. This is of importance for individuals with dementia where detection of erratic behavior can lead to earlier diagnosis and better management of the condition.

An individual moves around quite a bit while sleeping, except while in Random Eye Movement (REM) sleep. By monitoring motion while in bed, the quantity and duration of REM sleep states can be determined. This correlates with the quality of sleep and is another important metric used to gauge the overall health of an individual

1.2 Acute Health Monitoring

There are a number at risk populations for which monitoring for specific events and alerting when the condition is detected can mean the difference between life and death. These events can range from detecting the fall of an elderly patient to apnea in infants and alerting a caregiver to provide aid.

All the analysis must be performed locally for detection of a problem. Depending on what is being monitored, this can be computationally intensive which might require a faster (and more power-hungry) processor to perform the computation. However, the telemetry system uses considerably more power and reducing the required telemetry bandwidth is an advantageous trade-off.

1.2.1 Telemetry

For acute problems, there must exist a way to both localize the patient and report to an authority who can handle the acute condition in a timely manner. There are multiple approaches by which such a telemetry system can be implemented.

Location tracking is complicated in indoor environments where the GPS does not work, and some other type of location triangulation based system is required, possibly requiring an additional receiver [27, 70]. One solution is to leverage WPS built into most contemporary cellular phones when used in conjunction with an ambulatory monitor.

The transmitter on the ambulatory monitor can either be high-powered (i.e. utilizing a cellular

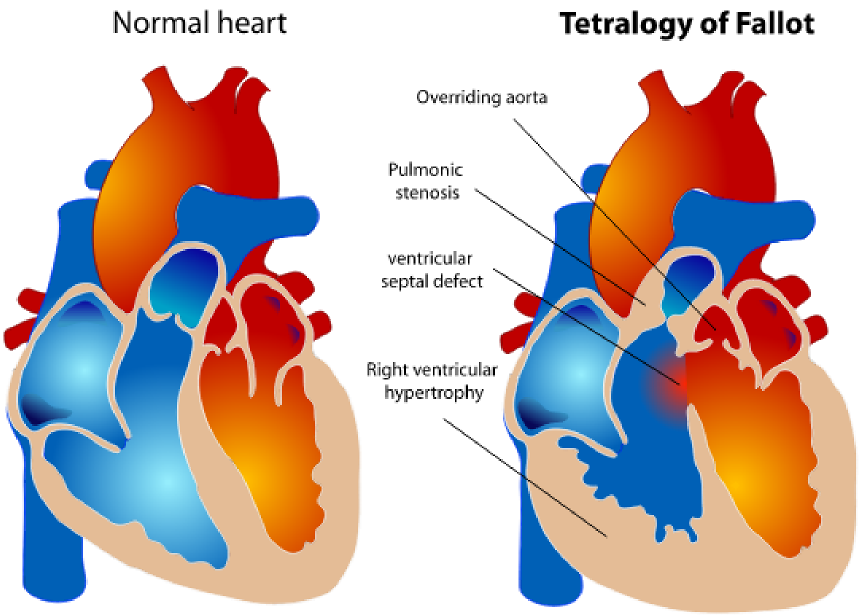

Figure 1.3: A normal heart compared to one with tetralogy of Fallot. From Wikipedia

modem) in order to relay data, or low powered and designed to interface with local receivers or to relay the data through a mobile phone which incorporates both a low-power receiver (such as Bluetooth) and a high-powered cellular transmitter.

1.2.2 Infants

Infants under 60 days of age are highly susceptible to a number of life-threatening conditions, such as apnea or infections. The importance of monitoring for these events increases if the infant has congential defects, such as tetralogy of fallot.

Children can stop breathing, or experience apnea. This can be a life threatening event, and it is belived that apnea is a cause of Sudden Infant Death Syndrome (SIDS)[40]. A PPG and ECG can be used to monitor for these conditions, and in fact, many such commercial systems exit in the marketplace. When such an event is detected, cardiopulmonary resuscitation can be initiated in order to save the child's life.

Tetralogy of the fallot (figure 1.3) is a congenital heart defect in which oxygenated and deoxygenated blood mix in the heart, resulting in low blood oxygen saturation. Children with this condition are susceptible to actue hypoxia resulting in syncope, or fainting, brain injury, and death. Using a PPG, it is possible to monitor blood oxygen saturation and provide intervention with drugs, oxygen, or physical manipulation to serious consequences.

Additionally, at home monitoring technologies can reduce the burden at Neonatal Intensive Care Units (NICUs). An average night in the NICU costs $2,500, and children are often kept longer than necessary to provide additional "just-in-case" monitoring. Often times, early discharge is possible with an ECG and PPG monitor.

1.2.3 Pregnant Women

Pregnant women have a number of additional high-risk situations which warrant monitoring. In the United States, it is estimated that 2%-6% of pregnant women experience preeclampsia[106], with a global rate of incidence between 5%-14%. Preeclampsia is a vascular endothelial disease which causes an increase in Blood Pressure (BP) which can lead to liver and renal failure. Left untreated, preeclampsia can cause seizures, known as eclampsia, as finally results in death.

Early detection by monitoring for a sudden increase in blood pressure (via the PTT proxy for blood pressure; see section 1.1.1) can provide life saving treatments such as medications, inducing labor, or performing a C-section.

Pregnant women may also be hypercoagulable, or have a very active blood-clotting system. An undesired blood-clot can enter the the lungs and form a pulmonary embolism which can lead to syncope, low BP, and death. A pulmonary embolism can causes an increase in the respiration rate and heart rate as well as a decrease in blood oxygen saturation. Early detection of a pulmonary embolism can lead to treatments with life-saving anticoagulant medication.

1.2.4 Immunosupressed Individuals

Immunosupressed individuals are at high risk for an infection, however, the fact that they are immunosupressed means that an infection does not manifest itself with a fever, making it difficult for an individual to notice. However, there are other physiologic manifestations of an infection which can be detected. These include an increase in heart rate, an increase in respiration rate, and possibly a reduction of blood oxygen saturation if a chest infection is involved. Once detected, antibiotic or other treatments can be initiated.

1.2.5 Elderly Patients

Elderly individuals are at high risk for a number of conditions including infections (see previous section) and falls. Infections often result in hospitalizations as infections can lead to AF in the elderly, but often times antibiotics with at home ECG and PPG monitoring are sufficient, improving the quality of life and reducing the burden on the health care system.

Fall Detection

Falls represent a serious problem for the elderly. They are a leading cause of fatal injuries and hospitalizations[39]. When an elderly person falls, they may not be able to get help due to injury or loss of consciousness. A system that can automatically detect a fall and request assistance can be invaluable in such a situation.

A lot of research exists in this field[16, 74, 88]. The inputs to these systems are typically accelerometers, though gyroscopes and magnetometers can also be used. Additionally, more than one sensor can be deployed on the body.

For our application, a single three-axis accelerometer was used. Gyroscopes are typically significantly more expensive and power hungry than accelerometers. And multiple sensors become more cumbersome for the user, require multiple devices to be charged independently, and increase

Figure 1.4: Patient undergoing a polysomnogram

the network complexity. Most contemporary Microelectromechanical Systems (MEMS) based accelerometers are capable of performing fall detection in hardware for use in hard drives which can potentially simplify the fall detection algorithms. As there are many systems that have been demonstrated to operate based on only accelerometer data with good results, the need for additional sensors was not justified.

1.3 Diagnosis

The first ambulatory ECG designed by Norman Holter was made to diagnose transient arrhythmias. For transient health problems, it becomes difficult for the physician to diagnose the cause of the problem if the symptoms do not manifest themselves during the office visit. This includes conditions such as seizures, cardiac problems, and sleep disorders. Ambulatory Electroencephalographs (EEGs) are used to help diagnose the nature of the seizure, Holter monitors are used to diagnose arrhythmias, and sleep study centers are used to diagnose the sleep disorder.

However, sleep study centers involve a very invasive procedure (figure 1.4) that forces the subject to spend the night at a special facility. One application of a multi-modal health monitor is to help diagnose sleep disorders in the comfort of one's own home.

Besides traditional ambulatory monitoring where just one metric is monitored, there is potential benefits for a more complete ambulatory picture for diagnosis by monitoring for a number of conditions.

1.3.1 Sleep Apnea

Obstructive Sleep Apnea (OSA) is a sleep disorder characterized by pauses or interruptions in breathing resulting in a reduction of oxygen intake. OSA is a serious health problem with medical consequences including hypertension, coronary vascular disease, congestive heart failure, cerebrovascular disease, glucose intolerance, impotence, and cognitive impairment [52]. It is also estimated that only 10% of the US population has been adequately screened for OSA, and the prevalence of the disease is much higher.

Early detection and treatment of this condition can significantly increase the quality of life of the individual and prevent the formation of other serious life-threatening diseases. Traditionally, OSA is diagnosed in a sleep center through a costly and uncomfortable procedure known as a polysomnography (also referred to as a sleep study; figure 1.4). A polysomnograph typically involves the patient being connected to a wide range of sensors including an ECG, EMG, Electrooculography (EOG) (a specialized form of EMG), EEG, airflow, pulse oximetry, and respiration monitoring. However, a simple pulse oximeter (PPG) has been demonstrated to be capable of detecting sleep apnea with a sensitivity of 98%[68], though low specificity. A single lead ECG has been demonstrated at being ~86% accurate in detecting sleep apnea in a few studies using different techniques[81, 104]. A combination of PPG and breathing sounds have demonstrated a 96% correlation to polysomnography[128]. Thus, having the full range of sensing modalities as a polysomnograph is not required for sleep apnea detection, though the additional signals can lead to better diagnosis.

In terms of noninvasive measurements, implementation of all of these metrics is possible with the exception of the airflow monitor. Though airflow detection is not technically difficult, it involves placement of a sensor near the nose of an individual and is significantly more invasive the remaining measurements. Additionally, a dedicated EOG was not deemed necessary as a general-purpose EMG can be used for this application.

1.3.2 Multi-Modal Ambulatory Diagnosis

Patients who have transient arrhythmias are given a Holter monitor to try to detect the irregular beats and determine what the problem is. However, a Holter monitor provides no information beyond the ECG. Being able to monitor the exertion levels of the individual, the blood oxygen saturation, and respiratory patterns during the arrhythmia can provide additional information that can help a physician better diagnose the patient.

1.4 Summary

Based on the analysis of the aforementioned use cases, a list of physiological sensing modalities has been determined (figure 1.5).

In addition to these sensing modalities, in a number of use cases, the accessibility to a smartphone to act as a display or gateway for telemetry would be required.

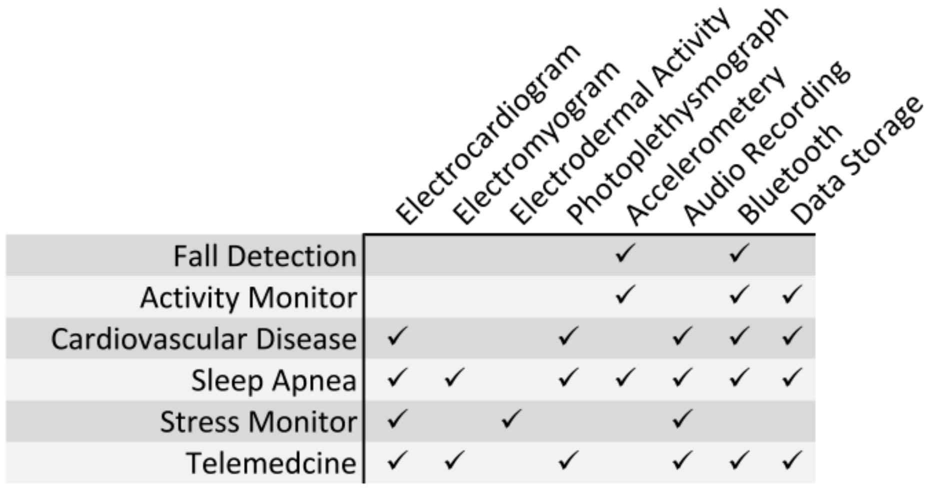

	Electrocardiogram	Electromyogram	Electrodermal Activity	Photoplethysmograph	Accelerometery	Audio Recording	Bluetooth	Data Storage
Fall Detection					✓		✓	
Activity Monitor					✓		✓	✓
Cardiovascular Disease	✓			✓		✓	✓	✓
Sleep Apnea	✓	✓		✓	✓	✓	✓	✓
Stress Monitor	✓		✓			✓		
Telemedcine	✓	✓		✓		✓	✓	✓

Figure 1.5: Physiologic sensing modalities for a number of use cases.

Chapter 2

Non-invasive Physiological Measurements

There are many forms of non-invasive physiological measurement possible, however, only a subset of these are amenable to ambulatory settings for truly pervasive monitoring. Additionally, the same physiologic parameter (i.e. heart rate) can be derived from a number of different measurement techniques (i.e. electrical or optical). This chapter highlights various implementations and the underlying physics and physiology underlying the measurements, the derived physiologic parameters (or metrics) and the utility of said metrics.

This chapter is broken into sections based on the type of technology required to make the various measurements.

2.1 Skin Potential Measurements

Given that the body is driven by and controlled through electrochemical reactions, a wealth of information can be gained by interfacing to the body through a galvanic, or electrical, interface. This includes both passive measurements that can be made by measuring differential electrical potentials, as well as active ones which involve measuring how an electrical signal sent through the body is modulated by the body.

2.1.1 Signal Transduction - Electrodes

For all such measurements, electrodes are used to transduce electrical potential in the body to the relevant electronics. The two extremes of electrode types are polarizable and non-polarizable, with real electrodes falling somewhere in the that range. Polarizable electrodes are effectively capacitativly-coupled and do not allow for any charge transfer across the skin – any current passing is a result of displacement current. Conversely, nonpolarizable electrodes allow for charge transfer through a reduction-oxidation reaction at the skin-electrode interface.

With polarizable electrodes, no charge is capable of being transferred from the electrode to the electrolyte, and thus a potential difference exists. In order to balance the electrostatic forces, ions of the opposite charge will accumulate at the electrode/electrolyte interface and effectively shield the the remainder of the electrolyte from the charge. This is referred to as the Helmholtz electrical double layer.

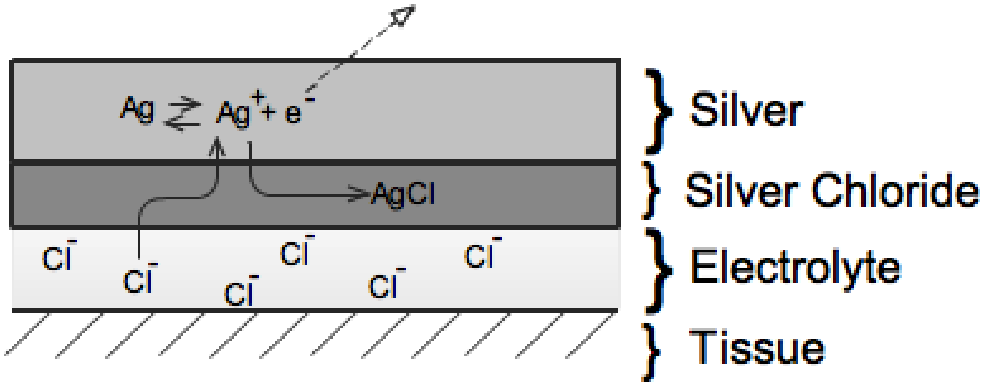

Figure 2.1: Silver-SilverChloride Electrode Redox Reaction

Polarizable, or capacitative, electrodes do not have a galvanic connection[89]. These electrodes can be fabricated with a thin layer of non-conducting dielectric material and offer benefits including being able to sense potential differences though clothes, but suffer from a very high sensitivity to external noise and an attenuation in the low-frequency components of the signal. Additionally, any electrode motion causes a redistribution of charge and introduces noise into the signal referred to as motion artifacts.

Non-polarizable electrodes are capable of transferring charge through oxidation-reduction reactions at the electrode-electrolyte interface, and thus do not form the electrical double layer. However, all real electrodes have some polarizable characteristics, thus it is impossible to fully avoid the formation of the electrical double layer.

In non-polarizable electrodes, ionic potentials in the body are converted into electrical potentials through a reduction/oxidation reactions which follow the basic form

$$C \rightleftharpoons C^{n+} + ne^- \tag{2.1}$$

$$A^{m-} \rightleftharpoons A + me^- \tag{2.2}$$

Where C and A represent the cation and the anion, respectively, and m and n represent their respected valencies. These reactions can are reversible for most electrode/electrolyte combinations, but not all. As a result, it is wise to not be too creative with electrode choices. There are many electrode/electrolyte combinations which various advantages and disadvantages, but we will focus on the most commonly used one: the Silver-Silver Chloride (Ag-AgCl) electrode. Among other benefits, the electrode chemistry will help minimize the effects of motion artifacts[121].

Silver-SilverChloride (Ag-AgCl) Electrodes

The Ag-AgCl electrode consists of a layer of silver surrounded by a very thin layer of silver chloride. A gel containing a high concentration of Cl^- ions and saturated with AgCl is often used in conjunction with the Ag-AgCl electrodes (Fig. 2.1).

The interface of the Ag-AgCl electrode, the electrolyte, and the skin form a equilibrium which is governed by the following equations.

$$Ag \rightleftharpoons Ag^{+} + e^{-} \tag{2.3}$$

$$Ag^{+} + Cl^{-} \rightleftharpoons AgCl \tag{2.4}$$

Metallic sliver will give up electrons, and spontaneously combines with free chloride ions to form silver chloride, which due to it's limited solubility, will precipitate out of solution adding to the silver chloride layer. These reactions occur constantly and reversibly, but the concentrations of the various constituents remain the same averaged over time resulting in no net current. However, if the potential of the tissue at the location of the electrode changes, then the reactions will be driven in one direction or another causing a net flow of electrons into or out of the electrode which can be measured.

2.1.2 Electrocardiogram (ECG)

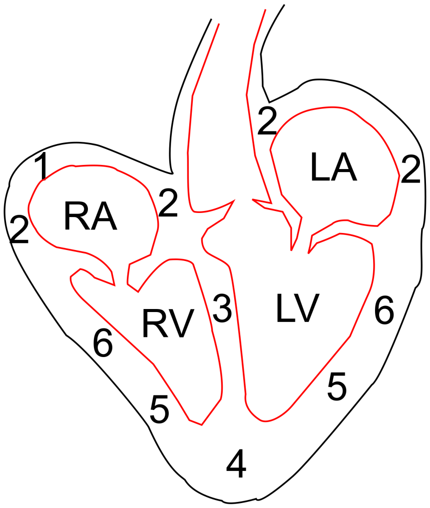

Figure 2.2: The order of depolarization in the heart. Point 1 represents the sino-atrial node, or pacemaker. The order of depolarization follows the numbers from 1 to 6.

The most common example of a surface potential measurement is that of the Electrocardiogram (ECG). The ECG is a device that measures the electrical activity of the heart.

The heart can be thought of as four distinct pumps which are synchronized to beat in a specific order. Blood from the body first fills the right atrium (RA) which is a essentially a low-pressure pump that fills the right ventricle (RV). The right ventricle is a higher pressure pump that pumps blood into the lungs. When blood returns from the lungs, it similarly fills the left atrium (LA), which fills the left ventricle (LV) who's job it is to pump blood at high pressure throughout the body (figure 2.2).

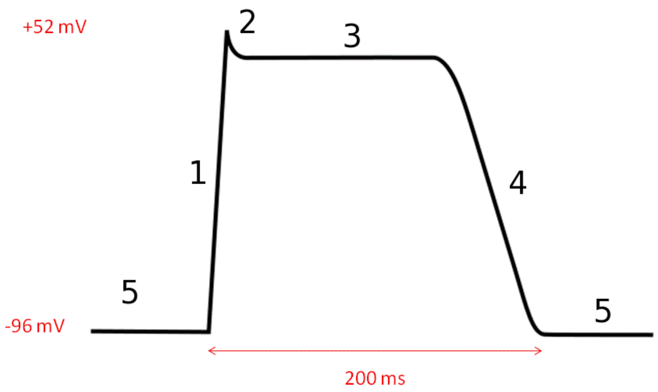

Figure 2.3: Myocyte internal potential relative to outside during the various stages of stimulation.

The electrocardiograph measures the electrical potential of the depolarization of the heart associated with the contraction and relaxation of the myocardium, or heart the muscle. The myocardium is unique in that when it is stimulated (also referred to as depolarization) it not only contracts, but stimulates adjacent muscle fibers to also contract. This starts a wave of propagating contractions that spread through the heart. In order to prevent runaway contractions (fibrillation), the muscle requires a period to reset before it can be re-stimulated. Additionally, the geometry and the addition of various types of tissues in the heart help guide the wave of depolarization to contract the appropriate parts of the heart in the right order (figure 2.2).

Physiology

At rest, the inside of the myocardium is negative in potential relative to it's exterior (~ -90mV). When stimulated, the myocardium undergoes a number of changes/stages (figure 2.3) as a result of various ion gates and pumps being activate on the cell membrane. The stages are as follows:

1. Opening of Na^+ channels on the membrane causing a large influx of Na^+ion. This is the depolarization phase.
2. Inactivation of Na^+ channels
3. Balanced influx of Ca^{2+} and outflow of K^+ions
4. Closing of Ca^{2+} channels. This is the repolarization phase.
5. Closing of K^+ channels. Resting (unstimulated) potential

The large number of myocytes undergoing synchronized depolarization can be modeled as a moving dipole in an anisotropic inhomogeneous volume conductor. The voltage difference at two points on the body can be approximated as the dot product of the dipole vector through the volume conductor with the vector formed by the electrode locations [93]. Different placements of the electrodes provide different views of the heart's electrical activity.

A heart that is damaged, as is the case after a heart attack, can result in problems with the propagation of the wave of electrical depolarization resulting in a number of chronic conditions. By utilizing an ECG to detect how the electrical activity of a heart has been altered, a cardiologist can determine how the heart has been damaged.

There are many additional uses for an ECG, such as measuring Heart Rate (HR). HR can be derived from the inverse of the duration between the occurrence of two sequential R-waves, corresponding to a ventricular contraction.

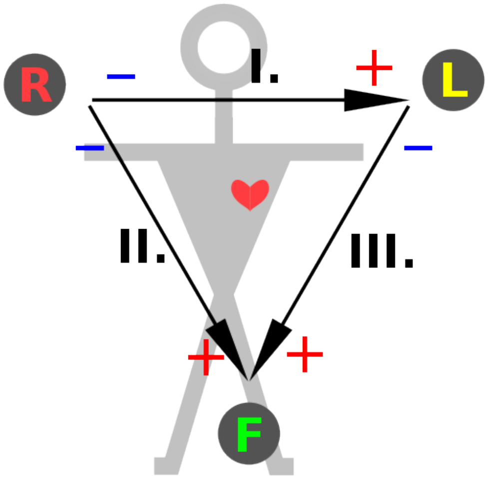

Figure 2.4: Einthoven ECG Lead Locations. From Wikipedia.

ECGs are described by either the number of channels or the number of electrodes. A channel refers to the number of different differential pairs, whereas the number of electrodes simply refer to the number of electrodes. The same electrode can be used a reference for multiple differential pairs, but when people speak about 5 or 12 electrode ECGs, standard known configurations are used. At a minimum, two electrodes are required to generate an ECG trace, but 3-electrode, 5-electrode and 12-electrode configurations can provide additional views of the heart's electrical activity to aid in monitoring and diagnosis. In this section, we will detail the implementation of a single channel ECG.

Measurement

The ECG signal bandwidth depends on the application. Often, the distinction is made between monitoring-ECG and diagnostic-ECG. Monitoring-ECG is used for routine examination of the ECG waveform, and is more heavily filtered to remove noise artifacts with a pass-band of 0.5Hz to 40Hz. Diagnostic-ECG is filtered less to provide a more detailed waveform for diagnosing cardiac problems, and typically ranges from .05Hz-150Hz[26]. You can see the relative contributions at the various frequencies in the power spectrum in figure 2.5a.

The heart is a large muscle capable of generating a strong signal on the surface of the skin, in the range of several millivolts in amplitude which makes it a fairly easy signal to detect. For a two-electrode configuration, placing an electrode on either side of the chest will work, however, it will be useful to understand the logic behind some standard ECG configurations in determining where to place the electrodes.

The first electrode configuration proposed was by Einthoven (Fig. 2.4), and uses two channels and three electrodes. The electrodes are placed on the left arm, right arm, and the left leg, and forms a triangle with the heart in the center. The differential voltage between any two electrode locations defines a view from the lead defined by electrodes, denoted as I, II, and III. Given the

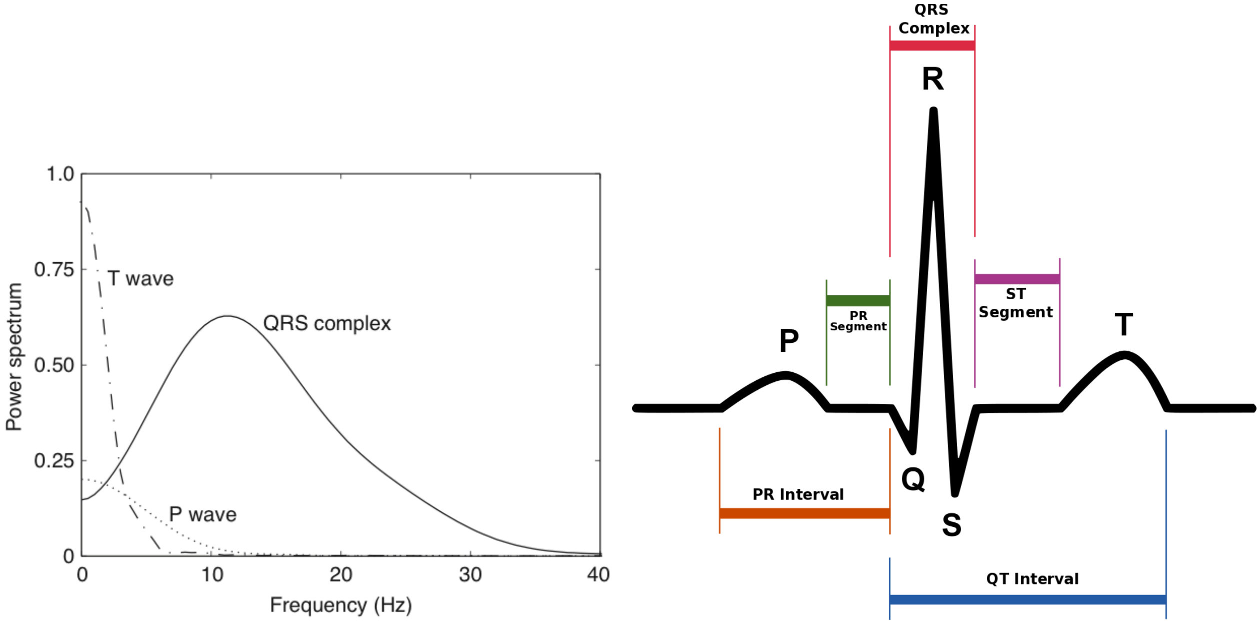

(a) ECG power spectrum of the various components. From Grimnes and Martinsen [48]

(b) Standard ECG waveform. From wikicommons.

Figure 2.5: ECG waveform and power spectrum

symmetry of the triangle, only two differential pairs are required to be measured, and the third lead can be determined from the sum or difference of the two differential measurements[124]. For example, if both positive electrodes are placed on the right foot (V_F), and the negative lead from one channel is placed on the left arm (V_L) and the other is placed on the right arm (V_R) then you have the following relationships.

$$V_{II} = V_F - V_R \tag{2.5}$$

$$V_{III} = V_F - V_L \tag{2.6}$$

It can then be shown that the difference of equation 2.6 from 2.5 will yield V_I.

$$V_{II} - V_{III} = (V_F - V_R) - (V_F - V_L)$$

$$V_{II} - V_{III} = V_L - V_R = V_I \tag{2.7}$$

There are a number of other electrode configurations worth considering[19, 45, 76].

2.1.3 Electromyogram (EMG)

An Electromyogram (EMG) is very similar to an ECG with the distinction that the electrical source is skeletal muscle rather than the heart. There are a large number of muscles that can be measured, all with different applications ranging from kinesiology studies of motion [3] to stress detection[72].

Physiology

When motor neurons are activated, they release the molecule acetylcholine which binds to receptors on the muscle fibers, and start an electrochemical cascade similar to what happens in the myocardium – ion channels open and begin a wave of depolarization resulting in muscle contraction. The dominant ion is Ca^{++}, and as long as it is present, the muscle fiber will continue to contract. If the frequency of stimulation from the motor neurons increase, the levels of Ca^{++} build up, increasing the force the muscle fiber generates until the force reaches a maximum (tetanus)[83]. Multiple motor neurons innervate adjacent muscle fibers, and the more motor neurons are activated, the more force is generated by the muscle fiber bundles. Thus, the force generated by a muscle can be though of as the sum of the product of the motor neurons (N_i) and their firing frequency (f_i).

$$Force = \sum (N_i f_i)$$

The EMG is capable of recording the electrical activity associated with initial depolarization of the muscle fiber. Given that there are quite a few muscle fibers in close proximity, and the firing between muscle fibers is uncorrelated, the EMG signal represents the summation of many muscle fibers depolarizing with the amplitude being proportional to the number of muscle fibers depolarizing.

2.2 Pulse Oximetry (Photoplethysmography)

Blood oxygenation is a critical parameter which can help diagnose conditions of pulmonary distress, hypovolemia[103], vascular perfusion, among others. The technique used to derive blood oxygenation is photoplethysmography, or the measurement of the volume of an organ through optical means. The essence of this measure is to determine the volume of the blood in the capillary bed near the skin in the area of interest as a function of time, which varies with the pulsation of the heart. Thus, this technique also allows one to derive the heart rate. The combination of this feature, along with the ECG allows one to derive the pulse transit time (PTT), or the amount of time between the ejection of blood from the heart to the pulse arrival time at a peripheral location. It has been shown that there is a direct correlation between PTT and arterial blood pressure[43].

Background

Pulse oximetry is a method by which the variation in the absorption of light by tissue is used to determine the percentage saturation of blood hemoglobin by oxygen. It is a specific type of Photoplethysmograph (PPG) used to measure Oxygen Saturation Percentage (SpO_2), and the two terms will be used interchangeably.

$$SpO_2 = \frac{OxegenatedHemoglobin}{TotalHemoglobin} = \frac{[HbO_2]}{[Hb] + [HbO_2]} \tag{2.8}$$

The modern technique was invented by Takuo Aoyagi, and works based on the following two principals. The first involves the macromolecule responsible for oxygen transport, hemoglobin (Hb). The iron containing Hb found inside blood cells binds to oxygen molecules and helps transport them at much higher concentrations than possible with freely dissolved oxygen in the blood.

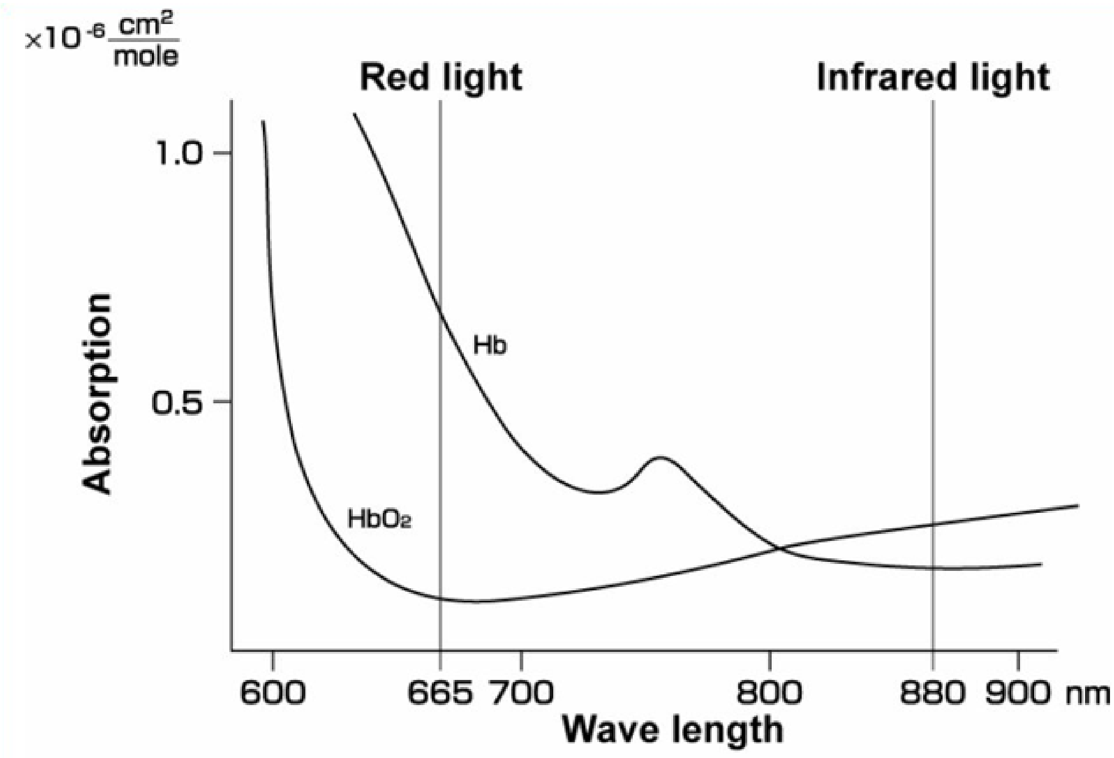

Figure 2.6: Hemoglobin Light Absorption Curves

Deoxygenated hemoglobin absorbs more red light than oxygenated hemoglobin (HbO_2), giving HbO_2 a brighter red color. The opposite is true for infrared light, where HbO_2 absorbs infrared light more than Hb (Fig. 2.6). This means that by measuring the ratio of absorption of red versus infrared light, the percentage oxygenation of the hemoglobin can be determined in samples of blood. However, there are many other types of tissues found in the body that also absorb varying levels of red and infrared light, and must be compensated for.

The second principal, which was the key to Takuo's discovery, was that it is possible to measure the variation in amplitude of light being absorbed due to the pulsatile nature of blood. As the heart beats, a pressure wave travels through the arteries to the capillaries which change in volume as they fill and empty with blood. By examining the ratio of absorption for just the pulsatile portion of the signal, you are able to compare red and infrared light absorption by the portion of blood that is changing, allowing for a direct measurement of a component of blood rather than that of any other tissue components.

Measurement

The implementation of this technique is simple: measure the ratio of the pulsatile portion of red to infrared light as it passes and is absorbed by tissue, multiplied by a calibration value. Both these steps are performed by shining alternating red and infrared light from closely mounted LEDs[1] through tissue (i.e. finger, ear) and measure intensity of transmitted light by a photodiode. The

---

[1] Ideally the LEDs will be on the same die as to maintain equal light paths through the tissue.

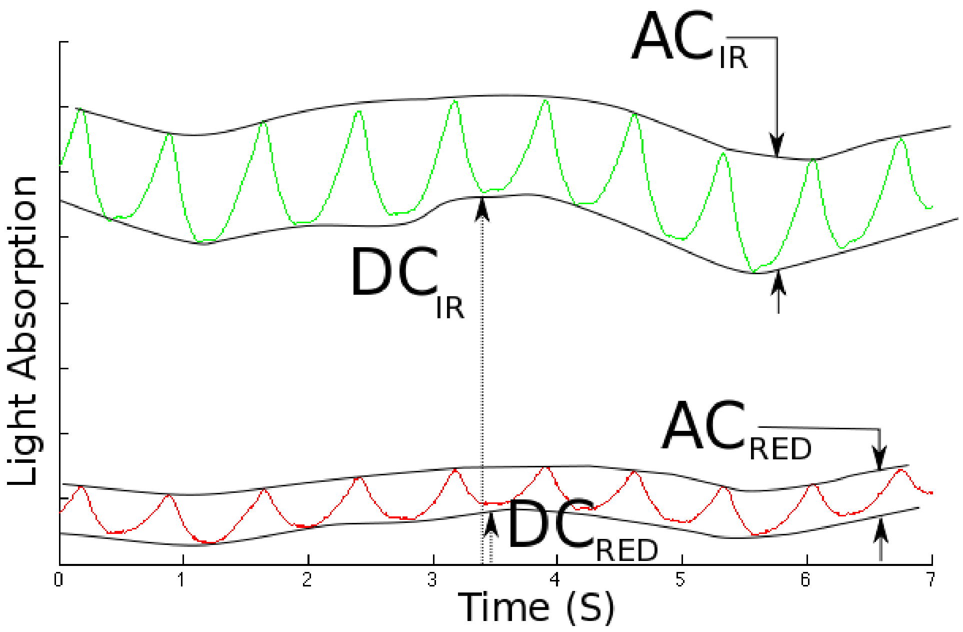

Figure 2.7: Light absorbed though tissue by Infrared (top curve) and red (bottom curve) light

resulting waveform will resemble Fig. 2.7. Next, in software, the amplitude of the waveform is measured for both light frequencies (AC_{RED}, AC_{IR}) as well as the DC bias of the waveforms (DC_{RED}, DC_{IR}).

The ratio $\frac{AC_{RED}}{AC_{IR}}$, based on our earlier reasoning, will relate to the concentration of oxygenated hemoglobin. However, this ratio needs to be corrected for variations in light intensity from the differed LEDs, the difference in absorption of the different frequencies of light by the tissue, as well as the varying sensitivity of the photodiode to the different frequencies of light. The ratio of DC biases ($\frac{DC_{IR}}{DC_{RED}}$) takes into account all of these variables, and the product of $\frac{AC_{RED}}{AC_{IR}}$ and $\frac{DC_{IR}}{DC_{RED}}$ will result in the ratio[2] :

$$R = \frac{DC_{IR}}{DC_{RED}} \frac{AC_{RED}}{AC_{IR}} \tag{2.9}$$

The ratio, R, directly corresponds to the percentage saturation of hemoglobin by oxygen (SpO_2). The exact relationship between blood oxygen saturation and R needs to be empirically derived by comparing the computed R ratio to blood oxygen content derived from blood samples taken from subjects while being deprived oxygen (figure 2.10).

Derivation

This relationship can also be derived through the application of the Beer-Lambert law, which states that a uniform (colinear) light will attenuate as it passes through a liquid containing molecules that absorb light based on the relationship:

---

[2] In most literature, you will find R expressed as the ratio of the logs of the ratios. The reasoning behind this is evident in the next section. However, as the relationship between R and the blood oxygen saturation is empirically derived, this ratio is sufficient.

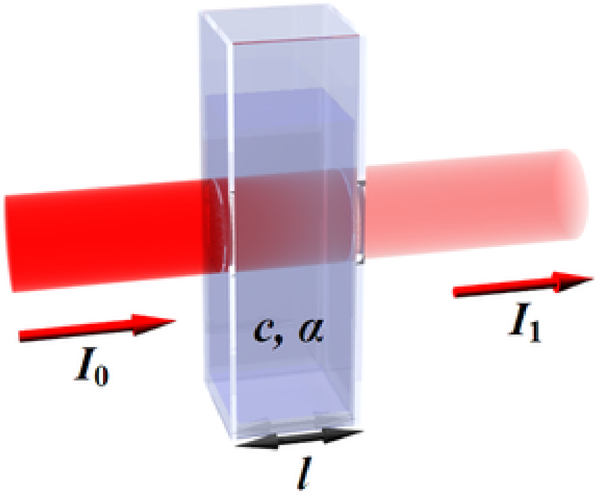

Figure 2.8: Beer-Lambert Law Example (image from wikicommons)

$$I_1 = I_o 10^{-(\alpha Cl)} \tag{2.10}$$

Where I_1 is the intensity of light (with an initial intensity I_o) as it passes through a liquid containing a concentration, c, of molecules with an extinction coefficient (how well it absorbs photons) of α and a length l (figure 2.8). For solutions containing multiple light absorbing particles, the transmitted light intensity can be calculated as the product of the light intensity from solutions containing only one species.

$$I_{c1} = I_o 10^{-(\alpha_{\lambda 1,c1} C_1 l)}$$

$$I_{c2} = I_o 10^{-(\alpha_{\lambda 1,c2} C_2 l)}$$

$$I_{\lambda_1} = I_{c1} I_{c2}$$

Applying equation 2.10 to the case of blood containing both Hb and HbO$_2$ for light of wavelength λ_1 yields

$$I_{\lambda_1} = I_o 10^{-(\alpha_{\lambda 1,c1} c_1 + \alpha_{\lambda 1,c2} c_2)l} \tag{2.11}$$

Where $c_1$and c_2 represent the concentrations of the Hb and HbO$_2$, respectively, and α_{λ_1,c_1} and α_{λ_1,c_2}correspond to the respective extinction coefficients for Hb and HbO$_2$ at a wavelength of λ_1.

Light with an initial intensity of I_o will be absorbed by the tissue, venous blood, stationary arterial blood, as well as the pulsatile arterial blood (figure 2.9) to yield an intensity I_{dc}. Light with intensity I_{dc}will then be absorbed by the pulsatile arterial blood and the amount of light transmitted will be I_{ac}.

$$I_{ac,\lambda_1} = I_{dc,\lambda_1} 10^{-(\alpha_{\lambda 1,c1} c_1 + \alpha_{\lambda 1,c2} c_2)l}$$

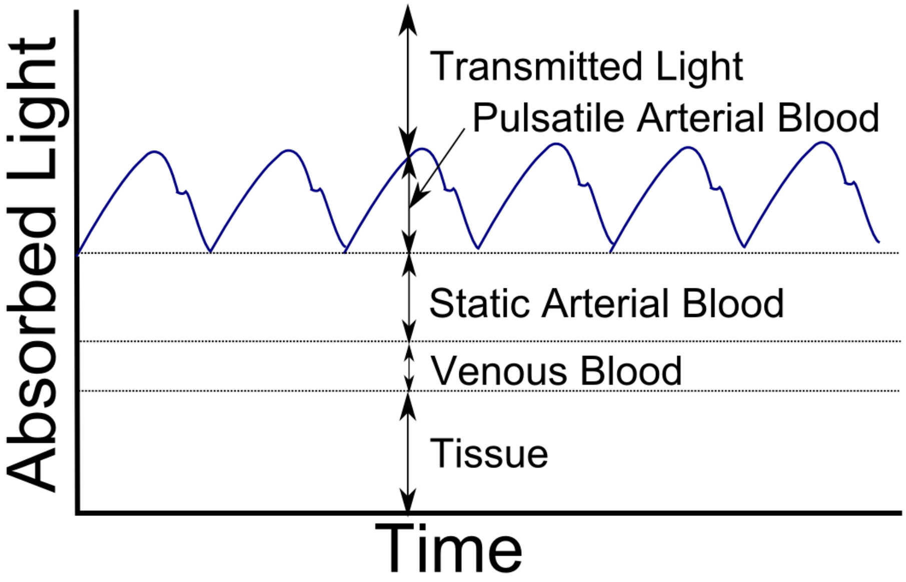

Figure 2.9: Light Absorption Through Tissue and Blood

By computing the log of the ratio $\frac{I_{ac,\lambda_1}}{I_{dc,\lambda_1}}$ we can eliminate the dependance on the incident light, I_o

$$log\left(\frac{I_{ac,\lambda_1}}{I_{dc,\lambda_1}}\right) = -(\alpha_{\lambda 1,c1}c_1 + \alpha_{\lambda 1,c2}c_2)l \tag{2.12}$$

By looking at the the ratio of of equation 2.12 at two different frequencies, and assuming that the LEDs are in close enough proximity such that the photon path is equal for the two different frequencies, we can remove the dependance on the length, l.

$$R = \frac{log\left(\frac{I_{ac,\lambda_1}}{I_{dc,\lambda_1}}\right)}{log\left(\frac{I_{ac,\lambda_2}}{I_{dc,\lambda_2}}\right)} = \frac{\alpha_{\lambda 1,c1}c_1 + \alpha_{\lambda 1,c2}c_2}{\alpha_{\lambda 2,c1}c_1 + \alpha_{\lambda 2,c2}c_2} \tag{2.13}$$

Where R is the ratio of ratios. Equation 2.13 can be rearranged to

$$\frac{c_2}{c_1 + c_2} = \frac{R\alpha_{\lambda 2,c1} - \alpha_{\lambda 1,c1}}{R(\alpha_{\lambda 2,c1} - \alpha_{\lambda 2,c2}) - \alpha_{\lambda 1,c1} + \alpha_{\lambda 1,c2}} \tag{2.14}$$

Note that c_2/c_1+c_2 is equal $[HbO_2]/[Hb]+[HbO_2]$, or the percentage of oxygenated hemoglobin (equation 2.8). Thus, the ratio R can be used to compute the blood oxygenation.

Caveats

Equations 2.13 and 2.14 make a number of assumptions. Namely that light does not scatter (it is collinear). This results in a deviation from the theoretical relationship between R and the blood oxygenation concentration (figure 2.10.

Additionally, this analysis assumes that only two types of hemoglobin are involved in the absorption of light. In fact, there several additional species of hemoglobin which also absorb light

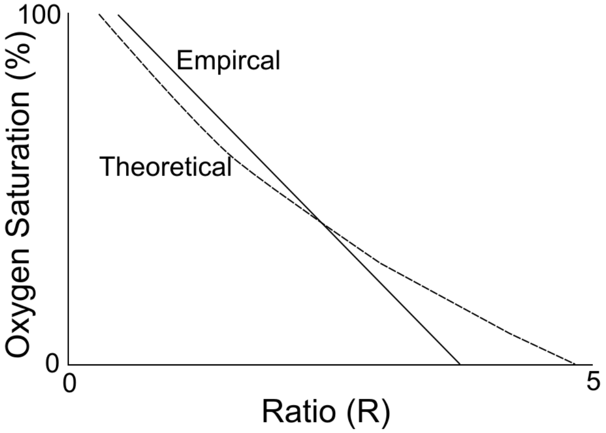

Figure 2.10: Theoretical vs. empirical relationship between the ratio *R* (equation 2.13) and the blood oxygen saturation percentage.

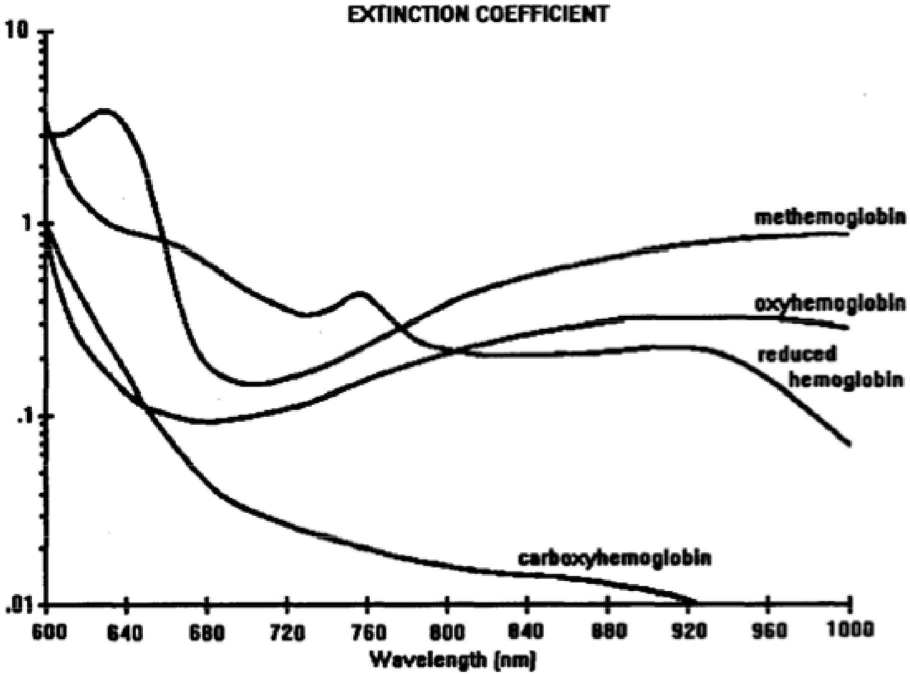

Figure 2.11: Extinction curve for oxyhemoglobin, reduced hemoglobin, methemoglobin, and carboxy-hemoglobin. (from [12])

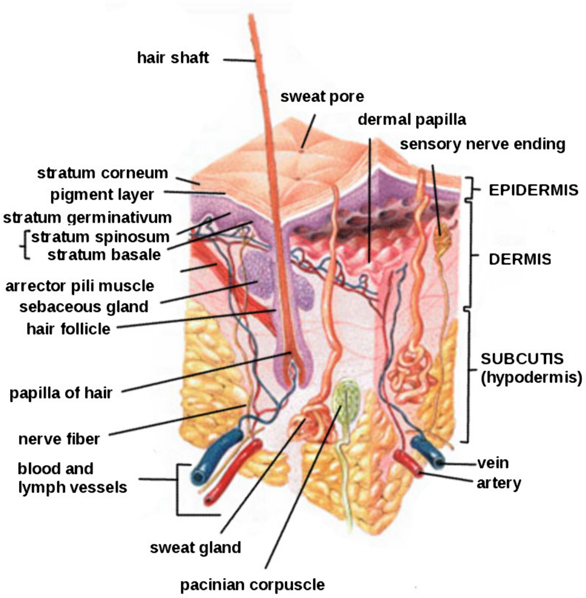

Figure 2.12: The anatomy of the skin. From Wikipedia

in the range of frequencies of interest (figure 2.11) . However, these other forms are not found in significant concentrations in a healthy average individual.

The calibration curves are generally only valid down to 80% oxygen saturation as they must be derived by measuring the ratio R while taking blood samples from a subject being deprived oxygen, and it is unsafe to reduce the oxygen saturation below 80% in test subjects.However, given that there are number of commercially available and calibrated pulse oximeters, it sufficient to use one of these devices to derive a R-SpO2 mapping, rather than drawing and analyzing blood from test subjects.

The description thus far has been for a transmissive pulse oximeter that works by measuring the levels of light absorbed by blood as light passes through tissue. There exists another type referred to as a reflective pulse oximeter which works by measuring the levels of light absorbed by blood as the light travels through tissue and backscatters back to the same side of the tissue where the LEDs are. Although the light-path differs, the same theoretical considerations apply. The most prominent placement for such a sensor is the forehead, but other locations have also been evaluated[113].

2.3 Bioimpedance

Bioimpedance (bioZ) refers to the act of measuring the impedance of tissue at various frequencies, and it is useful for a wide range of applications. Some sample applications include the ability to measure cardiac stroke volume [107], cardiac output[36], lung fluid content [42, 105, 129, 130], respiration rate and volume [101], body water/muscle/fat compartmentalization [6, 41, 51, 109], and blood glucose concentration [71].

The basic theory behind bioZ is that the flow of current through tissue is a function of the current frequency, the composition of the tissue, and the geometry of the tissue. Thus, by examining the impedance to the current flow at various frequencies, information can be derived about the

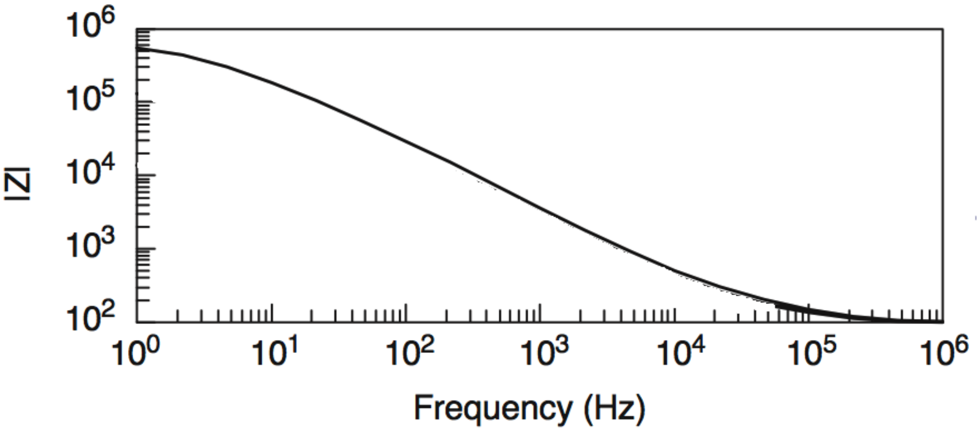

Figure 2.13: Skin impedance as a function of frequency. Ag-AgCl electrodes applied to dry skin on the forearm. From [4]

composition and geometry of the tissue. By varying the location of the electrodes on the body, you can control the current path and thus determine the target tissue.

The outermost layer of skin, the stratum corneum (figure 2.12), consists of a layer of dead epidermis cells and provides a high resistance to DC current (R_e in figure 2.14; $300k\Omega$ - $1M\Omega$) [4, 47] (figure 2.13). In order to overcome this high impedance, bioZ typically uses frequencies > 1kHz in order to shunt current through C_e.

There are also different methods by which current can be measured. The simplest way is to use two electrodes to inject the current and to measure the impedance between the electrodes. However, this method measures the impedance of everything in the path, from the wires and electrodes and it is highly susceptible to motion artifacts.

A more robust method requires 4 electrodes and is referred to as the tetrapolar electrode configuration. In this configuration, two electrodes are used as a current source/sink, and supply a fixed current independent of the impedance of the tissue. Another pair of electrodes are used to measure a differential voltage along the current path, which is proportional to the impedance of the tissue. The differential electrodes are connected to a very high impedance amplifier, such that practically no current crosses the measurement electrodes, and thus the electrode/skin impedance does not influence the measurements significantly.

2.3.1 Respiration

During respiration, the volume and geometry of the chest changes, and as a result, the impedance also changes. By measuring the impedance of the chest over time, we can determine the respiration rate and tidal volume[102]. For respiration, $50kHz$ is typically used with either the 2-electrode or 4-electrode configuration. Most commercial ECG monitors that include the ability to track respiration use the 2-electrode configuration and use the same electrodes as being used for ECG detection. As the frequency content of the ECG signal is less than 150Hz, the 50kHz bioZ current does not interfere with the ECG recordings. Likewise, the electrical ECG signal does not interfere with the 50kHz bioZ signal. However, as the heart pumps blood, there is a pulsatile increase and decrease in blood volume in the chest, which affects the impedance and can be measured if the

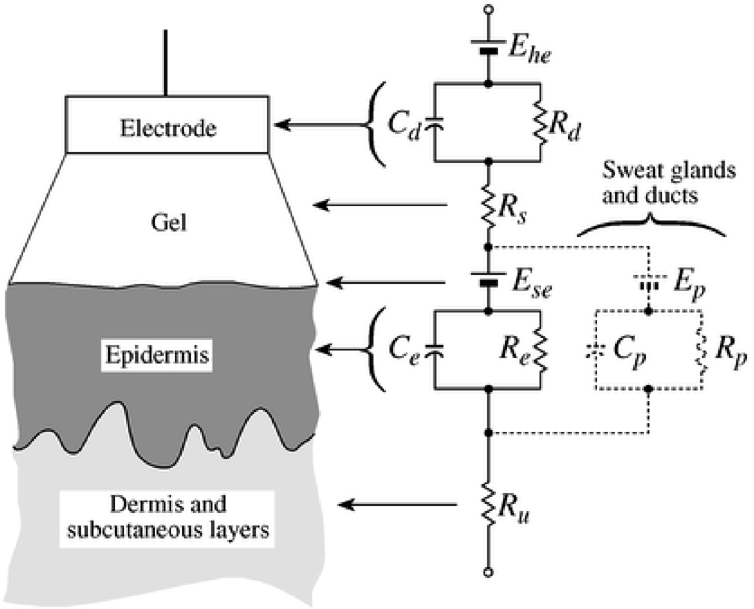

Figure 2.14: Equivalent circuit of an electrode placed on skin with an electrolyte gel. From [120]

major arteries are in the current path. Also, in the hospital setting where these devices are used, the subject is motionless and thus the sensitivity to motion artifacts is not an issue. Most ambulatory implementations of BioZ for respiration monitoring use the tetrapolar electrode configuration as it is more robust to motion artifacts.

2.3.2 Water Compartmentalization (Edema Measurement)

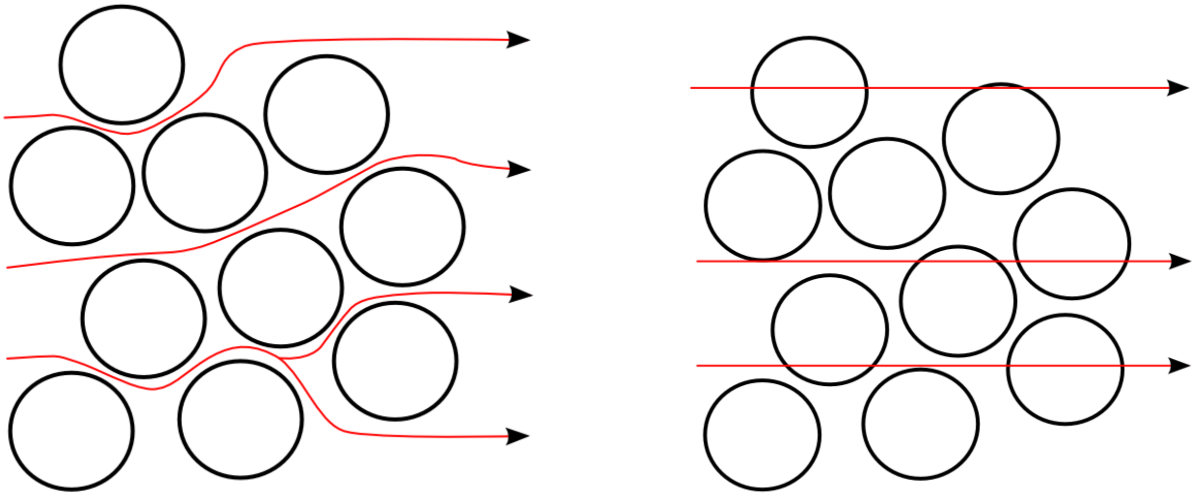

(a) Low frequency

(b) High frequency

Figure 2.15: Current flow around and through cells

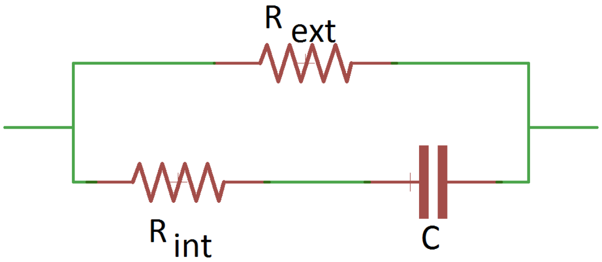

Figure 2.16: Electrical model of tissue

The ability of bioZ to determine water compartmentalization is based on the notion that the cellular wall, which is a lipid bilayer, does not allow the free flow of conductive electrolytes and thus acts like a capacitor. Thus, at low frequencies (figure 2.15a), the cell wall behaves as an insulator (high impedance), and the current flows predominantly around the cells through the extracellular fluid. At high frequencies (figure 2.15b), the cell wall behaves as a conductor (low impedance), and the current flows through both the intracellular and extracellular fluid.

The electrical model representation for such a system is presented in figure 2.16. R_{int} represents the intracellular resistance, R_{ext} represents the extracellular resistance, and C represents the cell wall capacitance. Thus, the impedance ,Z, of the electrical model is defined as

$$Z = \frac{(R_{int} + {}^{1}/_{j\omega C})R_{ext}}{R_{int} + {}^{1}/_{j\omega C} + R_{ext}} \tag{2.15}$$

We will further define $R_o = R_{ext}$ as the tissue impedance at DC, and $R_\infty = \frac{R_{ext}R_{int}}{R_{ext}+R_{int}}$ as the tissue impedance at infinite frequency. Equation 2.15 can be rewritten [34] as

$$Z = R_\infty + \frac{R_o - R_\infty}{1 + j\omega\tau} \tag{2.16}$$

Where $\tau = (R_{ext} + R_{int})C$ and ω is the angular frequency in radians. Decomposing the complex impedance in equation 2.16 into resistance, R, and reactance, X, yields

$$R = R_\infty + \frac{R_o - R_\infty}{1 + \omega^2\tau^2} \tag{2.17}$$

$$X = -\frac{\omega\tau(R_o - R_\infty)}{1 + \omega^2\tau^2} \tag{2.18}$$

Plotting equation 2.16 on a resistance vs. negative reactance[3] over a range of frequencies yields what is refereed to as a cole-cole plot[4] (figure 2.18a). For the circuit in figure 2.16, the plot will yield a semi-circle with intercepts on the X-Axis at R_o and R_∞.

However, cell walls have channels that do allow the flow of select ions, and vary in size and physical properties. Thus, it is generally not possible to determine a fixed value for the equivalent capacitance of the cell, C. This can be compensated for [32] by introducing an α variable into equation 2.16

$$Z = R_\infty + \frac{R_o - R_\infty}{1 + j\omega\tau^{(1-\alpha)}} \tag{2.19}$$

---

[3] Negative reactance is generally plotted, mostly for aesthetic reasons.

[4] Named after the work by Kenneth S. Cole and Robert H. Cole [32]

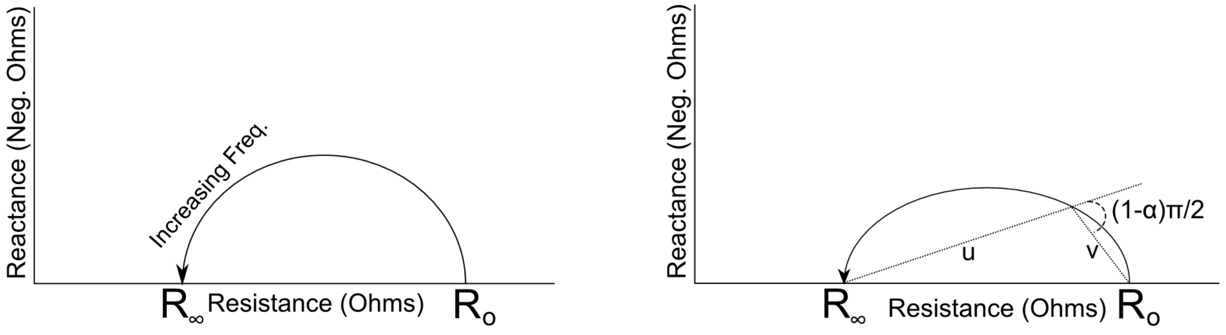

(a) Ideal capacitor

(b) Non-ideal capacitor.

Figure 2.18: Cole-Cole plot of resistance vs reactance for a range of frequencies

The variable α can range from 0 to 1, and results in a depression of the semicircle (figure 2.18b). The value of α can be derived by plotting the log of the ratio of cords (u/v) to the log of the frequency (w) (figure 2.17)[34].

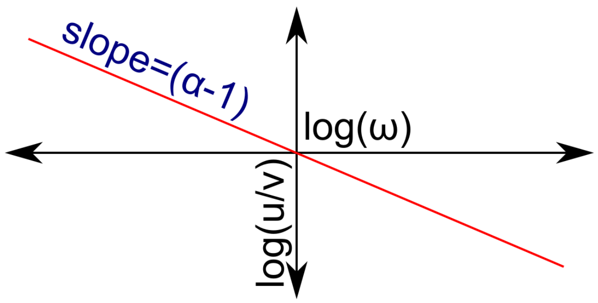

Figure 2.17: Determination of α from cole-cole plot.

Thus, by collecting bioZ data from the tissue in question, plotting the results and fitting the data to equation 2.19, we can determine both R_{int} and R_{ext}, which are proportional to the intra-cellular and extr-cellular water volume, respectively. Note, that we can not measure the impedance at DC due to the high skin resistance, nor can we measure at infinite frequency - thus we must extrapolate to these points.

2.4 Electrodermal Activity

Electrodermal Activity (EDA), also referred to as Electrodermal Response (EDR), or the galvanic skin response, is a measure of the electrical activity of the skin, primarily manifested by sweat gland activity (figure 2.12). The importance of this this measure is that the sweat gland activity is controlled via sympathetic nerve activity, and thus provides a mechanism to monitor autonomic nervous activity[66]. EDA has been used as method for measuring the level of arousal[49], emotion[60, 90], and stress[28] - all related to the autonomic nervous system. The hands are typically used as sites for the measurement due to the large number of sweat glands located there (figure 2.19).

Measurement

The simplest measure of EDA is to measure changes in the skin resistance, or it's inverse, conductance. As sweat gland activity increases, it decreases the resistance of the skin by filling the

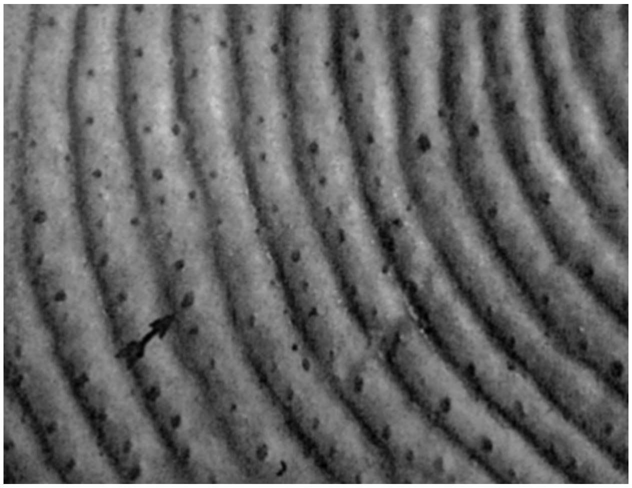

Figure 2.19: Distribution of sweat gland pores on finger tip. From [97]

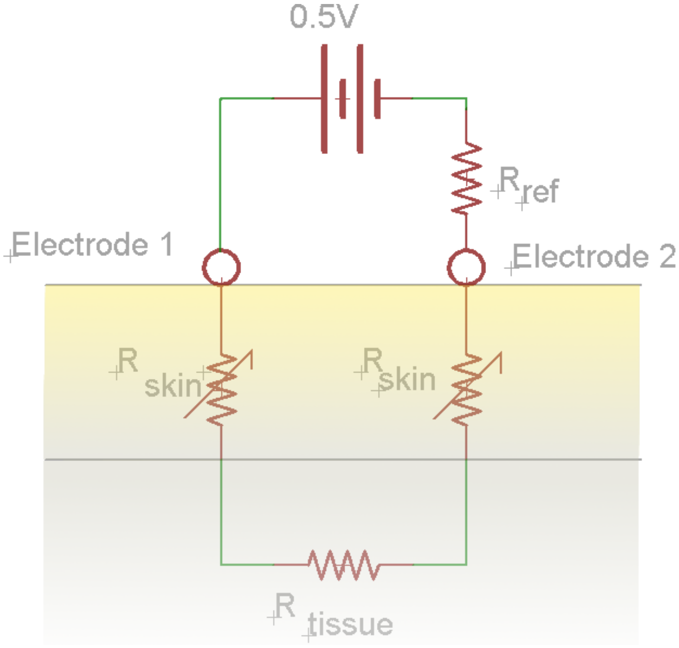

Figure 2.20: Measuring skin resistance using voltage divider

sweat ducts with a weak electrolyte solution, as well as by hydrating the corneum. For this type of measurement, it is sufficient to consider the skin a resistor, and to measure the resistance. This can be accomplished by placing two electrodes on the skin (typically on the hand, given the large number of sweat glands present), and by adding a voltage source (typically 0.5V) and another resistor of known value in series with the electrodes to form a resistive divider circuit (figure 2.20). The skin resistance (R_{skin}) is much higher than the tissue resistance (R_{tissue}), and thus the contribution from R_{tissue} can be neglected. Also, assuming that the electrode locations are close together, it is reasonable to approximate resistance for the current going into the tissue is equal to the resistance of the current leaving the tissue - thus we can define $R_{effective}$ as the sum of ($2R_{skin} + R_{tissue}$). Let I be the current flowing through the circuit,

$$0.5V = IR_{effective} + IR_{ref} \tag{2.20}$$

$$R_{effective} = \frac{0.5V}{I} - R_{ref} \tag{2.21}$$

Additionally, the voltage across R_{ref} is equal to $V_{R_{ref}}$

$$V_{R_{ref}} = IR_{ref} \tag{2.22}$$

$$I = \frac{V_{R_{ref}}}{R_{ref}} \tag{2.23}$$

Using equation 2.23 to simplify equation 2.21

$$R_{effecitve} = R_{ref}(\frac{.05V}{V_{R_{ref}}} - 1)$$

For an effective measurement, a high impedance amplifiers need to be used such as not to interfere with the resistance being measured. Additionally, the system must either implement a variable gain amplifier or the analog to digital converter with 24 bits of resolution is required as $R_{effective}$ can vary over many orders of magnitude.

Chapter 3

Design Rationale

The design of sensing modalities requires an understanding of the requirements for the signal. For example, the derivation of Heart Rate (HR) from an Electrocardiogram (ECG) only requires a low Signal to Noise Ratio (SNR) signal whereas detection of conditions such as an ST elevation requires much higher SNR. Based on the use cases discussed in chapter 1, the following requirements and trade-offs have been determined for the development of *The Berkeley Tricorder*.

There are a few terms which can be used to characterize a system and are relevant to most of the sensing modalities implemented in *The Berkeley Tricorder*.

Bandwidth The bandwidth of the system represents the range of frequencies in the signal that are of interest. Typically, a Low-Pass Filter (LPF), High-Pass Filter (HPF), or some combination of the two are used to exclude undesired frequencies allow desired ones to pass through.

Sampling Rate The sampling rate defines how many analog to digital conversions occur per second. The bandwidth typically determines the minimum acceptable sampling rate as at least twice as fast[1] as the maximum signal bandwith that can pass through the Analog Front End (AFE).

Signal to Noise Ratio (SNR) The SNR is the ratio of signal power to the noise power.

Sensitivity The sensitivity of a transducer is the minimum signal intensity required to produce an output for a given SNR.

Signal Dynamic Range The dynamic range of the signal represents the range between the minimum full scale signal and the maximum full scale signal of interest generated across a broad spectrum of individuals in the population. An example of two signals with a 10:1 full scale ratio is presented in figure 3.2.

Signal Resolution The signal resolution is the minimum resolvable difference in the input signal.

Visual Granularity The visual resolution represents the ratio of the minimum signal amplitude to the signal resolution. The visual resolution defines the number quantized bits for the smallest

---

[1] This is a result of the Nyquist-Shannon sampling theorem. Failure to do so will result in aliasing, or having higher frequency components of the signal appearing in lower frequency regions of the signal and potentially corrupting it.

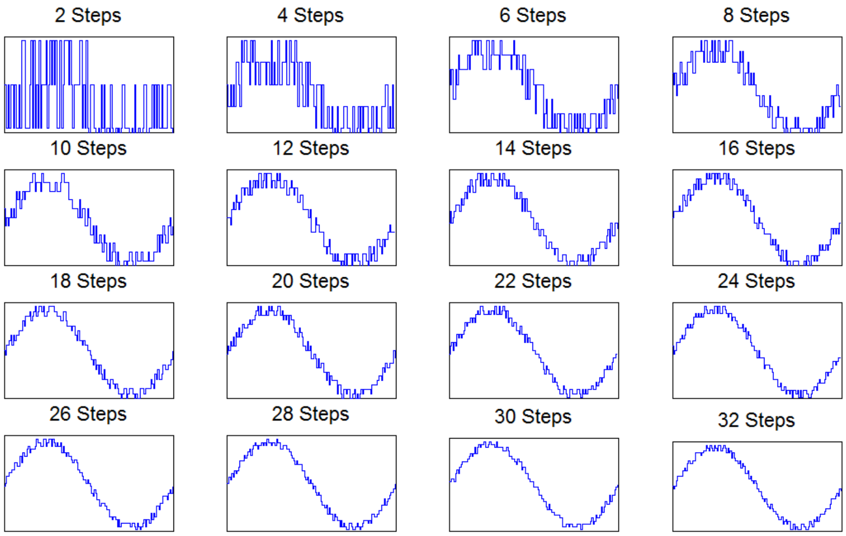

Figure 3.1: Differences in visual granularity (expressed as steps) in visualizing a sinusoidal signal with 1 bit of random noise.

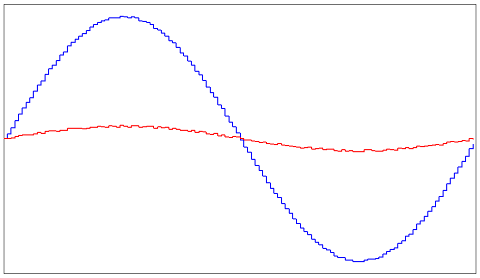

Figure 3.2: Example of different full scale signals with 1 bit of noise. The red plot is identical to the plot in figure 3.1 with 32 steps. The blue plot has a full scale amplitude 10 times as large with the same noise.

full scale signal present in the population. As many biologic signals are visually interpreted and analyzed, sufficient visual resolution is required to be able to interpret the signal. The higher the visual granularity ratio, the more discrete quantized values are used to represent the signal. Figure 3.1 demonstrates a range of different visual granularity ratios (expressed as steps) used visualize a sinusoidal signal with one bit worth of noise.

Safety Factor Before a signal is digitized, it must be within the bounds of input range of the Analog to Digital Converter (ADC). Motion artifacts can cause the signal experience a low frequency drift (figure 3.3) which can cause the signal to exceed the limits and saturate at either the high or low end of the input range. By providing an additional margin (for example: 2x the maximum signal amplitude), then the signal can shift up or down by 1/2 of it's maximum amplitude and not saturate.

The dynamic range and visual granularity help define the full scale of the signal which will be digitized. For input signals which do not have dynamic gain control, the sum of the bits required

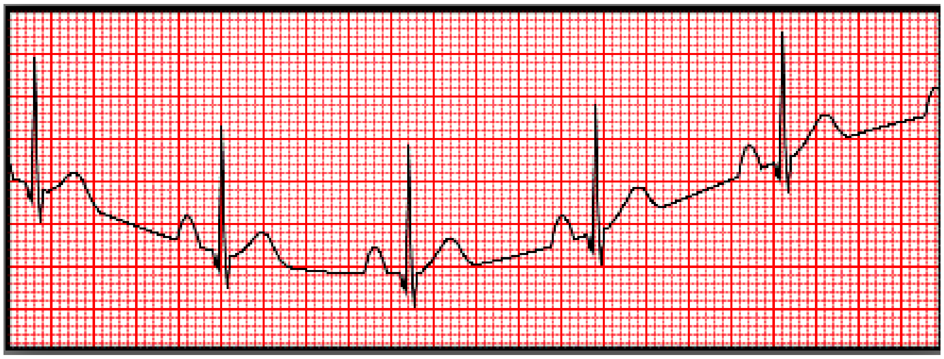

Figure 3.3: Example of wandering baseline. From http://www.mauvila.com/ECG/ecg_artifact.htm

to represent the dynamic range plus the bits required to represent the visual granularity represent the minimum number of ADC bits required to digitize the signal. For systems that have some other means of gain control, the number of bits required to represent the dynamic range can be significantly less by increasing the amplification of the smaller signals, dynamically.

Baseline Wander

One such complication is baseline wander. This is typically a result of electrode movement artifacts which disturb the charge distribution around the electrode causing transient DC offsets. The signal in question is superimposed on this DC offset, and thus appears as if the signals is “wandering” (figure 3.3). This can result in the signal saturating, even though the amplitude of the signal is less than the dynamic range of the system.

This effect can be mitigated by increasing the HPF corner frequency or increase the order of the HPF to reduce the low frequency components in the signal. Another strategy involves increasing the resolution of the ADC while reducing the system gain. This results no change in the signal dynamic range but requires a more costly ADC, as well as higher power consumption, and increase board space utilization.

Radio-Frequency Interference (RFI)

Another complication which affects the Analog Front End (AFE) is Radio Frequency Interference (RFI). RFI is a result of Radio-Frequency (RF) energy emanating from a transmitter being coupled to traces on the Printed Circuit Board (PCB) and entering an amplifier. The Common-Mode Rejection Ratio (CMRR) of an instrumentation amplifier drops of at higher frequencies and the the RF signal can be rectified inside the amplifier resulting in DC offsets[63]. Motion alters the coupling of the RF emissions between the transmitter and the PCB traces altering the DC offset and thus generating low frequency noise.

To combat this, the AFE must filter for high frequency common mode noise by implementing an RFI filter. A typical RFI filter shown in figure C.1, and is explained in appendix C.

3.1 Electrocardiogram (ECG)

The ECG[2] is useful in monitoring a wide range of conditions, as discussed in chapter 1. A relevant sampling of conditions which help define the ECG implementation in *The Berkeley Tricorder* include:

- Detection of ST elevation
- Detection of Ventricular Tachycardia (VT), Atrial Fibrillation (AF)
- Measurement of Blood Pressure (BP) through Pulse Transit Time (PTT)
- Localization of the QRS Complex, used for
  - Measurement of Heart Rate (HR)
  - Measurement of Heart Rate Variablity (HRV)

These conditions have different requirements for an ECG system, and an optimization must be performed to design the system to applicable to as many applications as possible while providing good ambulatory data.

The bandwidth of the signal is typically defined as $0.5Hz - 50Hz$ for monitoring and $.05Hz - 150Hz$ for diagnostic quality. The additional low-frequency bandwidth is required to diagnose certain diseases, and the additional high-frequency bandwidth is to monitor for the pulse from a pacemaker.

The dynamic range of the ECG signal across individuals and situations is $0.05mV - 2.8mV$[87] though this value can be higher in abnormal situations. The ratio of the largest to smallest full-scale signal is $2.8mV/0.05mV$ and it requires $\frac{ln(\frac{2.8mV}{0.05mV})}{ln(2)} = 5.8$ bits to represent. As the signal can drift due to baseline wander, it is useful to allow for a larger signal amplitude to prevent saturating the signal when amplified or digitized. Given the very low frequency component of the bandwidth, it would be useful to allow for a factor of 4 as a “safety-margin” to accommodate baseline drift. Thus the maximum system bandwidth computed as $(2.8mV)(4) = 11.2mV$. It takes an additional $\frac{ln(4)}{ln(2)} = 2$ bits to encode the safety margin.

The ECG is measured by amplifying the difference in surface potentials at two points on the body as described in section 2.1.2 using an instrumentation amplifier. The advantage of an instrumentation amplifier is high CMRR, thus being able to automatically filter much of the external RF noise, such as the strong $60Hz$[3] powerline noise. Additionally, the instrumentation amplifier has very high input impedance[4] minimizing current flow across the electrode/skin interface which can influence the measurement.

ST Elevation

---

[2] The basis of the ECG is described in section 2.1.2.

[3] The powerline noise is 60Hz in the US, and can be 50Hz in other countries.

[4] For most sensor inputs with filters preceding the amplifier, the input impedance is defined by HPF, and is typically 3 orders of magnitude smaller than the input impedance of the instrumentation amplifier.

Detection of an ST segment elevation (figure 3.4) is important for early detection of a Myocardial Infarction (MI) resulting from occlusion of a major coronary artery.

Only one lead is required to detect the ST Elevation, and it is defined as a $\geq 100uV$ or $\geq 200uV$ elevation[5] of the ST segment, depending on which electrode configuration is used. Thus, we would need to be able to clearly distinguish a difference of $100\mu V$. However, the minimum single amplitude is $50\mu V$, and thus this sets the lower bounds for determining our resolution.

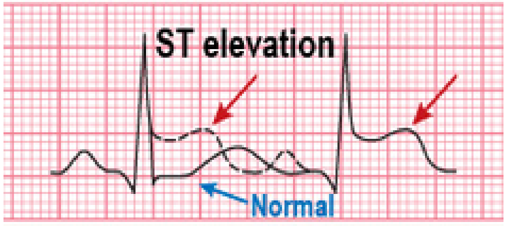

Figure 3.4: Examples of ST Elevation. From http://www.pepidonline.com/

As the interpretation of the ECG signal is visually performed, sufficient visual granularity must exist to allow for interpretation. Based on figure 3.1, a visual granularity of 25:1 should be sufficient and translates to a signal resolution of $\frac{50\mu V}{25} = 2\mu V$. A visual resolution of 25:1 requires 4.6 bits of ADC resolution.

By examining figure 2.5a, it is apparent that the T-wave is a very low frequency component, and thus the extended diagnostic bandwidth with a low frequency component of .05Hz would be ideal. However, in many cases, a 0.5Hz HPF is still sufficient to diagnose an ST elevation. The blue (upper) trace in figure 3.5 was manually digitized from an ST elevation example[6] and linearly resampled at 100Hz. A single order $0.5Hz$ Butterworth HPF was then applied and the results plotted in the green (lower) trace. The original ST elevation plot demonstrated a $139\mu V$ elevation, and the one with additional filtering demonstrates a $136\mu V$ elevation. Both these values are clinically significant to diagnose an ST elevation condition, and represent a $\frac{139\mu V - 136\mu V}{139\mu V} = 2\%$ decrease in the measured value.

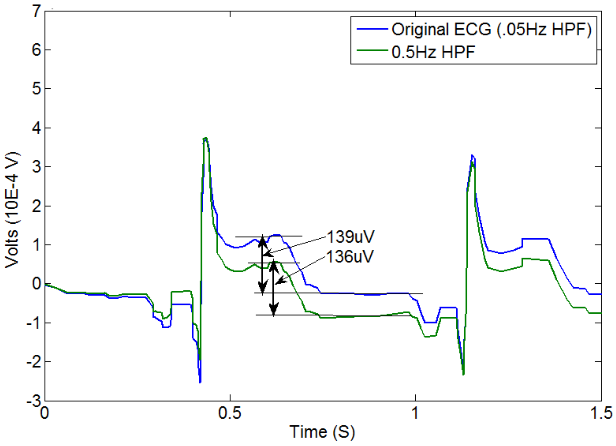

Figure 3.5: ST elevation example passed through .5Hz HPF

For the upper frequency range, 50Hz is sufficient. This predicates a minimum sampling rate of 100Hz. The required characteristics for this measurement are summarized in table 3.1.

Ideally, the noise will be quantized by one bit, and thus will have an amplitude equal to the signal resolution, or $2\mu V$ in this situation. The minimum SNR can thus be approximated as the ratio of the visual resolution, or $20\,log(\frac{25}{1}) = 27.9dB$.

Metric	Value	Bits to Encode
Bandwidth (ideal)	$0.05Hz - 50Hz$	
Sampling Rate	$100Hz$	
Signal Resolution	$2\mu V$	
Visual Resolution	$25:1$	4.6
Signal Dynamic Range	$0.05mV - 2.8mV$	5.8
Safety Margin	$4x$	2

Table 3.1: Summary of requirements for ECG to detect an elevated ST segment.

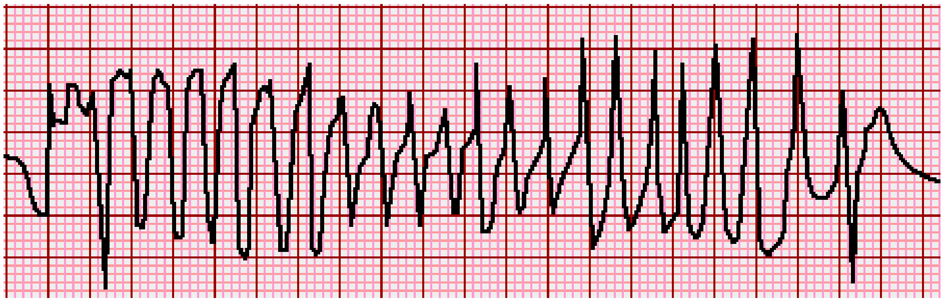

Figure 3.6: Example of Ventricular Tachycardia (VT). From http://www.cardiachealth.org/ventricular-tachycardia-vt

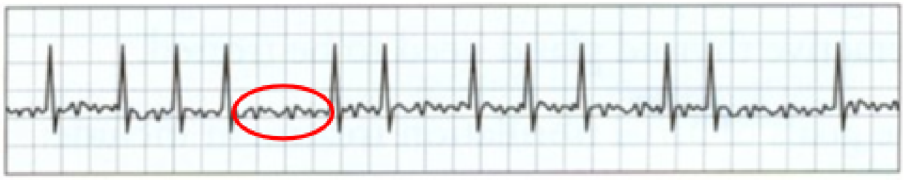

Figure 3.7: Example of Atrial Fibrillation (AF). Adapted From http://www.a-fib.com/Overview.htm

Metric	Value	Bits to Encode
Bandwidth (ideal)	$0.5Hz - 50Hz$	
Sampling Rate	$100Hz$	
Signal Resolution	$2\mu V$	
Visual Resolution	$25:1$	4.6
Signal Dynamic Range	$0.05mV - 2.8mV$	5.8
Safety Margin	$4x$	2

Table 3.2: Summary of requirements for ECG to measure heart rate.

Ventricular Tachycardia, Atrial Fibrillation

The diagnosis of Ventricular Tachycardia (VT) and Atrial Fibrillation (AF) is from a subjective evaluation of the morphology of the ECG trace. VT is a rapid, regular heart rhythm (figure 3.6). AF results from uncontrolled muscular contractions in the atrium and manifests itself as a set of irregular waves between heartbeats (figure 3.7).

A standard monitoring ECG is sufficient to diagnose these events. The requirements for ST elevation diagnosis are equally applicable towards VT and AF diagnosis, except the narrower bandwidth of $.5Hz - 50Hz$ is sufficient.

QRS Localization for Heart Rate

Heart rate is the inverse of the duration between beats of the heart. The duration is measured between successive passages of a fiduciary point on the ECG waveform. Although any point can be used, the most common is the QRS complex (figure 2.5b). Both the maximum amplitude of the R wave as well as the slope of the QR or RS segment can be used.

By examining the power spectrum of the QRS complex (figure 2.5a), we find that the energy is spread from DC to 40Hz with a peak at 10Hz. In this case, the default *monitoring* ECG bandwidth of .5Hz to 50Hz, and a sampling rate of 100Hz would be sufficient.

The minimum normal R wave amplitude is 0.05mV[87]. Approximating an visual resolution of 25:1, as per the previous section, we would like a resolution at least 25 times greater than the minimum amplitude, or $50\mu V/25 = 2\mu V$.

The requirements for heart rate extraction are summarized in table 3.2. The requirements are identical those in table 3.1, except the bandwidth is reduced.

As before, in ideal conditions, the noise will be quantified by one bit, or $2\mu V$ in this case; the SNR will remain the same as previously calculated.

QRS Localization for Heart Rate Variability Monitoring

There are a number of methods by which HRV can be quantified. The most sensitive of these methods involve analyzing the frequency domain of the heart rate inter-beat interval[7], and requires a $1ms$ accuracy. As stated, the R-wave peak is often used as a fiducial point in measuring the

---

[5] On a standard ECG strip chart, this corresponds to 1-2mm.

[6] http://www.clinicaljunior.com/cardiologyecg.html

[7] This is the time between each beat

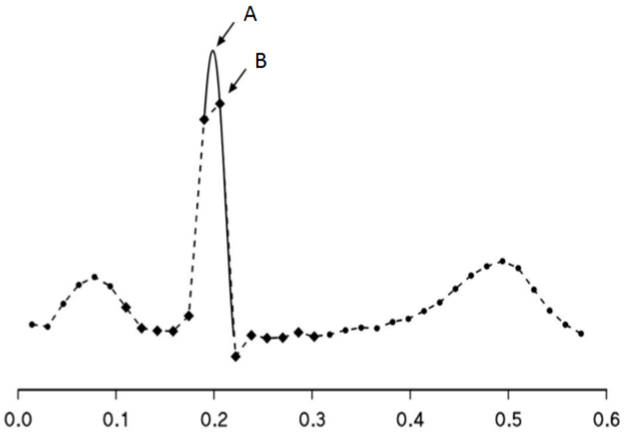

Figure 3.8: Example of misidentified ECG R-Wave peak. A sample taken at point *B* incorrectly misidentified the R-wave time. Scale is in seconds. Adapted from [25].

inter-beat interval. An issue arises if the sampling times of the ADC do not correspond with the location of the R-wave peak. Consider the example in figure 3.8, where samples are taken at the location of the dots. In the example, the R-wave peak is identified as point B, whereas the actual peak is located at point A. This results in an error of $t_B - t_A$seconds. The inter-beat interval is the difference between two sequential measurements, where the errors from the two measurements can either increase or cancel. This time-jitter will increase the high frequency component of the frequency domain and will cause erroneous errors.

In order to combat this, a number of strategies can be utilized.

1. The simplest method is to increase the sampling frequency to $1000Hz$. This will reduce the error in localizing the R-wave peak to $500\mu S$, and the maximum cumulative error between two measurements to $1ms$.
2. To interpolate in the frequency domain to better reconstruct the signal and the location of R-wave peak. One such implementation is detailed in [25].
3. To recompute the actual R-wave peak by extrapolating from the slopes just before and after the R-wave peak and determining the point of intersection. This can also be performed by spline interpolation or an interpolation filter.

Sampling the signal at a higher rate will not only satisfy the requirements for HRV analysis, but can also help increase the SNR of the signal, as detailed in the previous section.

Blood Pressure through Pulse Transit Time

The PTT is a relative measurement, and only changes in the measure are of interest. In order to derive a PTT measurement, the time between the ventricular contraction in the heart and the passage of the pulse wave in the periphery from a Photoplethysmograph (PPG) must determined.

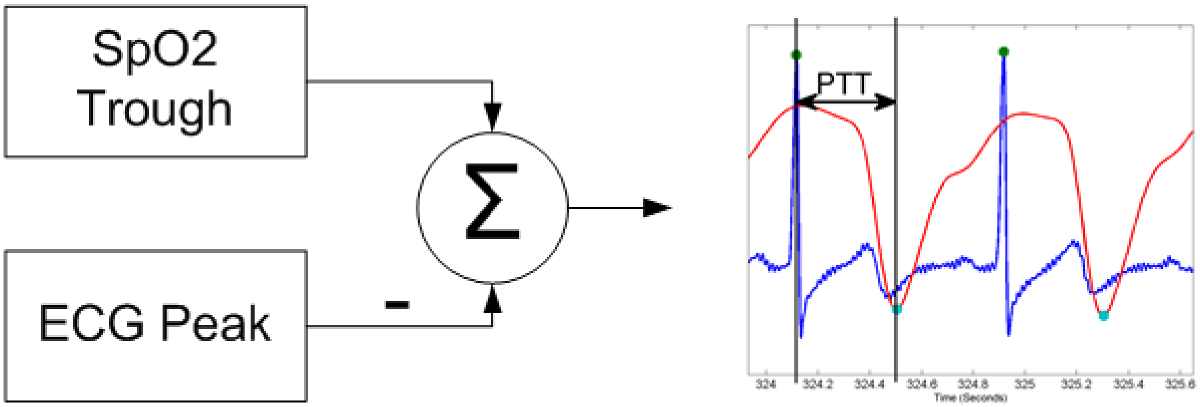

Figure 3.9: Pulse Transit Time (PTT) derivation. The raw ECG and PPG waveforms are filtered and the peak and trough are detected. The difference between these times is the PTT.

The ventricular contraction occurs during the maximum of the R-Wave peak[8], and the pulse wave is detected at a minimum point in the PPG waveform (figure 3.9).

A HRV measurement requires a $1ms$ temporal resolution of the ECG waveform, which is more than sufficient for PTT measurements, thus the same set of requirements apply for this measurement.

3.2 Electromyogram (EMG)

Electromyogram (EMG)[9] has a wide range of applications ranging from diagnosing a neuropathy, such as carpal tunnel syndrome, to aiding in rehabilitation. It has even been demonstrated to be relevant in stress detection[72].

The two implementations of EMG include surface EMG and intramuscular EMG. Intramuscular involves placing a needle into the musculature to record the electrical activity of specific muscles fibers, whereas surface EMG records a differential signal across a wider area. For surface EMG, the typical electrode spacing is 20mm. For ambulatory recording, only surface EMG was considered.

The bandwidth of an EMG signal is from $5 - 500Hz$ (figure 3.10), with a maximum amplitude of $6mV$ peak-to-peak [14]. Given that the lowest frequency of interest for an EMG is an order of magnitude greater than that of an ECG (5Hz), it enables us to implement a more aggressive HPF and mitigate the effects of baseline wander. We can thus reduce our amplitude “safty-margin” to a factor of 2. It takes an additional $\frac{ln(2)}{ln(2)} = 1$ bit to encode the safety margin.

Unlike the heart which always produces an ECG signal, the voluntary muscles of the body only generate a signal when they are active. Thus the lower bound of the amplitude is equal to the noise floor of the measurement setup.

---

[8] There is a period of isometric contraction that elapses between the R-wave peak and the ejection of blood which is typically constant and ignored in the measurement

[9] The basis of the EMG is described in section 2.1.3.

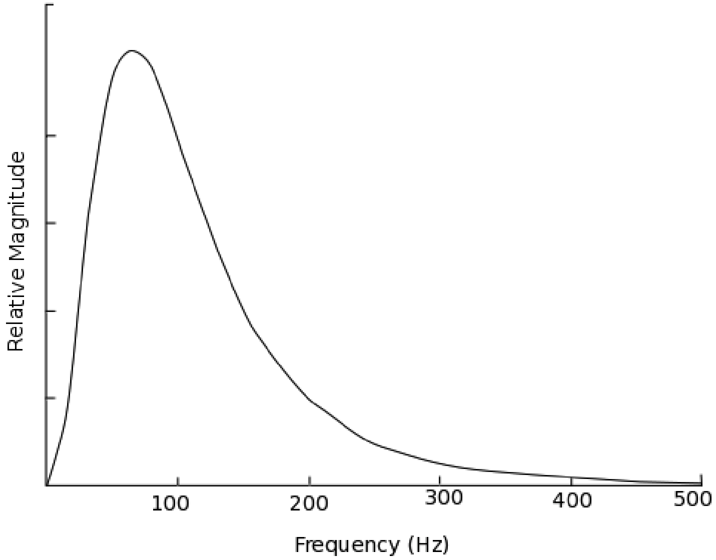

Figure 3.10: EMG Power Spectrum (Redrawn from [44])

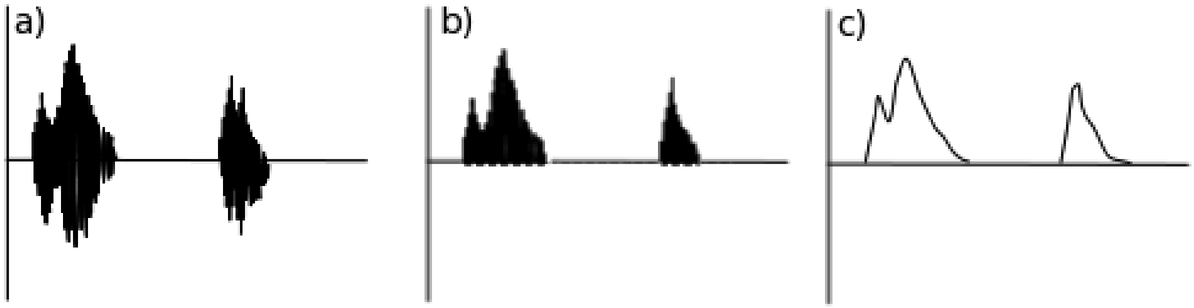

Figure 3.11: (a) Raw EMG Signal (b) Rectified EMG Signal (c) Low pass filtered

To avoid aliasing issues, we need to sample at twice the highest frequency component, or $1kHz$. A summary of the requirements to measure the EMG is found in table 3.3.

If the goal of the signal acquisition is to simply quantify relative muscle contraction, then the signal can be rectified, low pass filtered at 50Hz, and sampled at 100Hz[80] (figure 3.11). This process can also be performed in software on the high frequency data, so sampling at the higher data rate with a wider bandwidth is advantageous.

3.3 Pulse Oximeter (Photoplethysmograph (PPG))

PPG has a number of applications, and the design of the system is dependent on it's particular use. The application most people are familiar with is to measure blood Oxygen Saturation Percentage (SpO_2). The SpO_2 is useful in monitoring for respiratory failure, asthmatic attacks, Chronic Obstructive Pulmonary Diease (COPD), and acute hypoxia manifestations[84]. Additionally, a

Metric	Value
Bandwidth	$5Hz - 500Hz$
Sampling Rate	$1000Hz$
Signal dynamic range	$noise\,floor - 12mV$
Safety Factor	2x

Table 3.3: Summary of requirements for EMG.

PPG can be used to derive a a heart rate, and when used in conjunction with an ECG a secondary metric, the Pulse Transit Time (PTT) can be derived, and is used to detect relative changes in blood pressure.

The main difference between the different implementations is the number of Light-Emitting Diode (LED) light sources required, and how the light intensity is sampled. For SpO_2, two different frequencies of light are required, as detailed in section 2.2. For detection of heart rate, only one frequency of light is required and the hardware implementation is significantly simplified. As our applications include measurement of blood SpO_2, which can also be used for heart rate measurements, the implementation requirements of a two-frequency system will be detailed.

The basis of a two-wavelength PPG implementation consists of the following components:

- Two (ideally monochromatic) is a light sources in the range of 600-1300nm[10].
- Different levels of absorption by oxygenated Hemoglobin (HbO_2) and deoxygenated Hemoglobin (Hb) at the two wavelengths.
- Constant light intensity for the duration of the measurement,
- Light paths as identical as possible by two wavelengths.
- Light detector sensitive to wavelengths.
- Mechanical system to ensure light enters tissue then the detector while minimizing external light intrusion and mechanical stability.
- Shielding for cables to reduce Electromagnetic Interference (EMI) noise.

Light Source

The aforementioned requirements are fairly broad; initial implementations of a PPG utilized a wide spectrum light source with a set of rotating filters (similar to how contemporary Digital Light Processing (DLP) projectors work with a color wheel). Lasers would provide the ideal light source as they output a very narrow bandwidth of light and are very coherent. However, they are expensive, require complex optics or fiber optic cables to ensure identical light paths, and can potentially cause excessive heating of the tissue.

The most prevalent solution is to use an LED to as the light source. Although LEDs have a broader spectrum (in the order of $\pm 30nm$) than a laser and the output frequency can vary per die,

---

[10] Light is absorbed by skin pigment at wavelengths shorter than 600nm and by water for wavelengths greater than 1300nm.

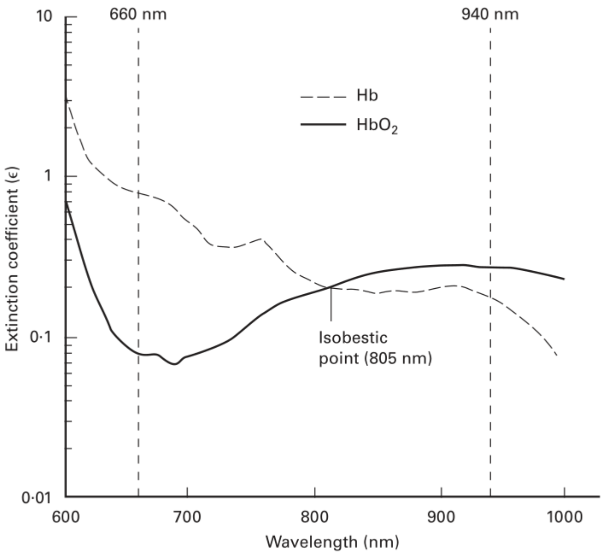

Figure 3.12: Absorption of oxygenated and de-oxygenated hemoglobin at various wavelengths. From [84]

they are inexpensive, can be made to operate at just about any frequency, are physically small, and multiple LEDs can be manufactured on the same die. Additionally, they generate very little heat, and can be switched on/off very quickly.

Although any frequency between 600-1300nm can be used, typically 660nm and 940nm are used. Light at 660nm has the advantage as it is extremely sensitive to changes in HbO_2 and Hb concentration. And light at 940nm has a relatively flat absorption, and is thus less sensitive to manufacturing variations in the peak wavelength of the LED.

The light source must also be stable in intensity, as any noise will couple to the detector and present as noise in the system. Additionally, the optics involved will ideally focus the beam as narrowly as possible to optimize light entering the tissue.

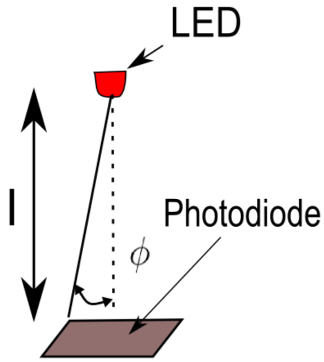

Figure 3.13: LED light incident on photodiode.

Different LEDs have different efficiencies in converting electricity to optical power. For a low-power application, it is essential to use high-efficiency LEDs where possible.

The light emanating from an LED is not collinear, rather it spreads as a function of the optics. In an ideal case, the optics will focus as much of the light energy into a tight beam directed to the photodiode, although light scattering will occur. Assuming no scattering, the intensity of light which reaches the photodiode is a function of the area of the photodiode and it's distance. Datasheets for LEDs typically specify the relative light intensity as a function of the angle from center (figure 3.13). The center of the photodiode will be aligned with the center of the LED, and

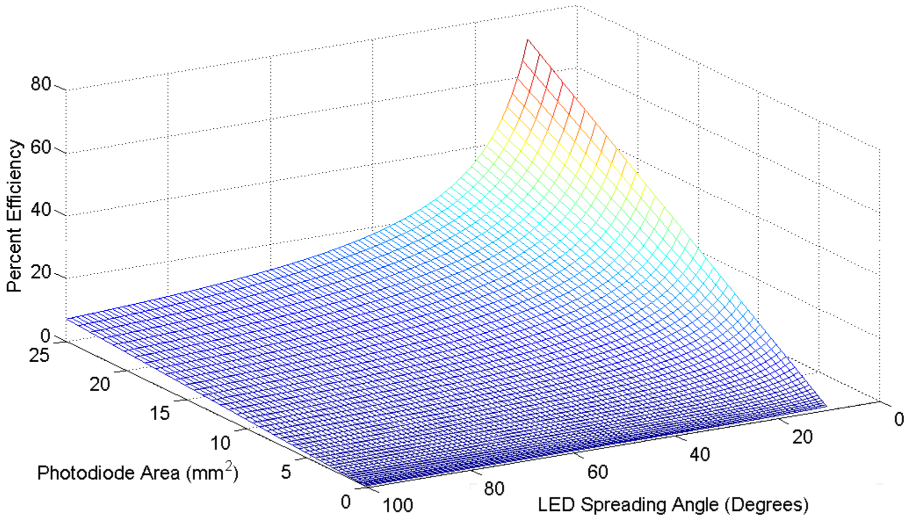

Figure 3.14: Efficiency of transmitting light to a photodiode for a range of photodiode sizes and LED spreading angles in an non-absorbing medium.

the periphery of a photodiode will have an angle of $\phi = tan^{-1}(\frac{w/2}{l})$ where w is the width of the photodiode, and l is the distance between the LED and photodiode. For a typical distance of $8mm$ (for a finger) and a typical photodiode width of $3mm$, we compute $\phi = tan^{-1}(\frac{3mm/2}{8mm}) = 10^o$. Thus the incident light on the photodiode is the sum of light intensities from $-10^o$to $+10^o$ minus the light absorbed by the tissue for this typical case.

Although the light energy is not typically spread uniformly from an LED due to it's optics, if we approximate that it is spread spherically up to it's published limits[11] we can compute the relative efficiency of transmitting light through a non-absorbing medium to the photodiode as a function of the published spreading angle. If we let I_o be the initial light intensity at the LED, we can compute I, the intensity of light received at the photodiode as the product of the light intensity spread uniformly over a sphere, $\frac{I_o}{4\pi l^2}$, with a concentration factor, $\frac{360}{\alpha}$, which assumes the light spread only over a portion of the sphere defined by it's spreading angle, α, and the surface area of the photodiode, w^2.

$$I = \frac{I_o}{4\pi l^2}\frac{360}{\alpha}w^2$$

Simple rearrangement allows us to solve for the efficiency, $\frac{I}{I_o}$. For the case of a 8mm separation distance, we can compute the effects of the spreading angle and size of photodiode on the efficiency; a summary is provided in figure 3.14.

Signal Characteristics

The ratio of pulse wave AC amplitude to the DC offset was computed for data collected from the initial human trials (see figure 2.7 for a reference). The range of ratios for the infrared light range

---

[11] LEDs are often published with a spreading angle.

from .014 − .072 and .0075 − .027 for the red light. The increased infrared amplitude is a result of lower absorption from the tissue and higher sensitivity of the photodiode to the infrared light. For a given DC offset, the ratio of the maximum to minimum amplitude ratio is $0.072/.0075 = 9.6$, which defines the dynamic range of the signal. It takes $\frac{ln(9.6)}{ln(2)} = 3.56$ bits to encode the dynamic range.

As the goal is to have a 1% resolution in the blood oxygen saturation percentage, we require a visual granularity of 100:1 in the AC pulse wave the signals. It requires $\frac{ln(100)}{ln(2)} = 6.6$ bits to encode the visual granularity.

As most SpO_2 implementations have a methodology by which to adjust the offset of the AC pulse signal, there is no requirement for a "safety-margin".

The actual amplitude of the signal is a function of the tissue and relative perfusion, however, it is also function of the LED current, the LED efficiency, the photodiode efficiency, and photodiode sensitivity which are all unknown values. Thus, it is not possible to define a minimum resolution for the system until the hardware is characterized.

Once the hardware is finalized, and the maximum light intensity incident on the photodiode, I_o, is determined, the maximum incident light can be computed from the maximum absorption coefficient and the maximum finger thickness for a population using the lambert-beer relationship as

$$I = I_o e^{-\mu_a l}$$

The incident light must then be converted into a current based on the efficiency of the photodiode for the given frequency, and then to a voltage. Assuming a value of β for the conversion and that signal to a voltage, the resulting signal will have a DC value of

$$V_{dc} = I\beta = I_o \beta e^{-\mu_a l}$$

The minimum AC amplitude can be computed from the ratio of the minimum AC to DC amplitude, $R_{ac/dc}$. Based on the previously computed data, the minimum ratio is 0.0075.

$$V_{ac} = V_{dc} R_{ac/dc} = I_o R_{ac/dc} \beta e^{-\mu_a l}$$

And given the desired 100:1 visual granularity, we can compute the minimum required resolution as

$$Resolution = V_{ac}/100 = \frac{I_o R_{ac/dc} \beta e^{-\mu_a l}}{100}$$

If it is possible to keep the noise to within one bit of resolution, the SNR can be calculated as $20\, log(\frac{100}{1}) = 40$.

Digitization

The sampling rate is typically a function of the maximum bandwidth of the signal. In the case of a PPG, the maximum frequency of interest is quite low ($0.5Hz - 2.5Hz$[98]), and one would expect a low sampling rate to be sufficient. Based on sampling theory, we expect the minimum single-wavelength sampling frequency to be twice the highest bandwidth component, or $2(2.5Hz) = 5Hz$. However, sampling rates below 70Hz can produce a visible flicker which and thus sampling

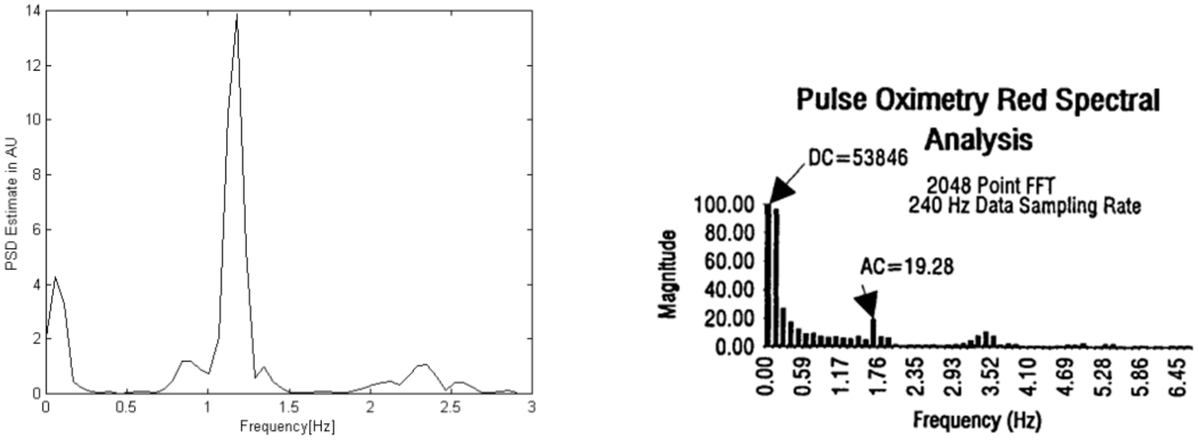

(a) From [85]

(b) From [96]

Figure 3.15: Power spectrum of a PPG signal.

rates are typically much higher. Published implementations list single-channel sampling rates of 75Hz[122], 100Hz[2].

The PPG also requires different light sources to be sampled, and thus the sampling rate must be increased to accommodate the different light wavelengths being sampled. In addition to the two wavelengths, additional samples are acquired when both LEDs are off in order to measure the level of background light that is entering the detector, and to subtract it from the other signals. Thus, the final sampling rate (multiplexing the red, infrared, and dark signals) must be at least 3x the highest as the sampling rate for each signal, and the resulting bandwidth must be twice as large as that figure.

A sampling rate of 100Hz will avoid flicker, and spread the current consumption more evenly, and thus presents a good compromise.

Other Considerations

There are a number of tradeoffs that are worth mentioning.

- The SNR is proportional to the volume of blood in the tissue being measured, thus, tissues that suffer from poor blood flow, or vasoconstriction due to cold temperatures will result in a poor signal. Localized heating of the tissue can increase the SNR but will consume significant current.
- The SNR is greater the further the LEDs and photodiode are from each other, as the light travels through and is effected by more tissue, but additional LED current is required (and LEDs that can handle higher currents) which decreases battery life.
- The faster the amplifier and ADC circuitry, the shorter the duty cycle of the LEDs which result in lower power consumption at the expense of additional noise due to higher cutoff frequency for the low pass filters

The signal amplitude also varies depending on the location and type of sensor. A list of relative SNRs for different body locations and sensor types have been compiled[114] (figure 3.16) and are

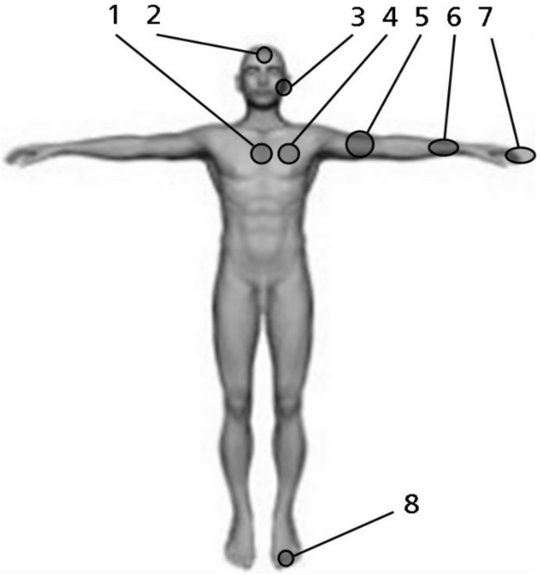

Figure 3.16: Locations for PPG mesurements. From [84]

	SNR (dB)		
Area	Finger Clip	Ear Clip	Reflectance
Chest (1)			6.3
Forehead (2)			14
Ear (3)		17.4	
Pectoral (4)			5.5
Upper Arm (5)			15.5
Wrist (6)			8
Finger (7)	23.4		15.6
Toe (8)	10.5		

Table 3.4: Relative SNR measurements from various parts of the body. From [114]

listed in table 3.4.

A summary of the results are presented in table 3.5.

3.4 BioImpedance (BioZ)

Bioimpedance (BioZ) has a wide range of applications. In the realm of ambulatory physiologic monitoring, two applications are monitoring respiration and edema.

Monitoring respiration is important in a large number of cases. It's critical to monitor respiration in patients with cardiopulmonary issues such as congestive heart failure and patients who are on medication which suppresses breathing. It's also useful in diagnosing a number of conditions such as systemic inflammatory response syndrome (SIRS). Our original attempt at respiration rate detection relied on acoustic pickup with a microphone, but we found bioimpedance to be a much

Metric	Value	Bits to Encode
Signal Bandwidth	600Hz	
Sampling Rate	100Hz x3	
Dynamic Range	9.6:1†	3.65
Visual Granularity	100:1	6.6
Safety Factor	0	0

Table 3.5: Design summary for a PPG implementation. (†)Only a ratio could be calculated.

more reliable indicator of respiration rate. Bioimpedance also allows us to measure relative breathing tidal volumes and to detect coughs.

Edema monitoring has applications ranging from measuring fluid status in dialysis patients [65], to monitoring pulmonary fluid in patients with Congestive Heart Failure (CHF)[131].

Bioimpedance can also be used for a number of other diagnostic measurements such as measuring cardiac output[35] and body fat[110], although we have not investigated these applications.

3.4.1 Respiration

There are numerous ways to measure an individual's respiration rate and/or volume. These methods are summarized below.

Spirometer The gold standard for respiration volume, and involves breathing into an airflow transducer, but does not lend itself to ambulatory monitoring as a mask is required.

Thermistor A thermistor placed under the nose can measure respiration rate by monitoring for changes in the thermistor's resistance as the airflow from the nose heats it. This method also does not lend itself for ambulatory measurements and does not quantify any air flowing through the mouth.

Resistive Stretch Band An elastic band with a resistive element in series is used to measure the deformation of the abdomen and/or thorax as an individual breathes. Such a system is relatively inexpensive, but is more invasive a measure as it needs to wrap around the chest and is sensitive to motion artifacts.

Gas Transducer This system is similar to the resistive stretch band, but uses an air bladder in the strap and a pressure transducer to measure deformation.

Respiratory Inductive Plethysmography (RIP) Conductive fibers are sewn into an elastic band which is placed around the abdomen and/or thorax. The conductive fibers in the circular configuration form a single loop inductor where the inductance is proportional to the natural log of the ratio of the loop radius to the thickness of the conductive fibers. This inductor is used to form a resonant circuit where the frequency varies as a function of the loop radius which is a function of the level of distention of the abdomen or thorax.

Impedance Plethysmography (BioZ) As the lungs deform through the process of breathing, the impedance of the lungs change. The impedance, also referred to as BioZ, is measured by transmitting a high frequency, fixed current sinusoidal signal, and measuring the impedance

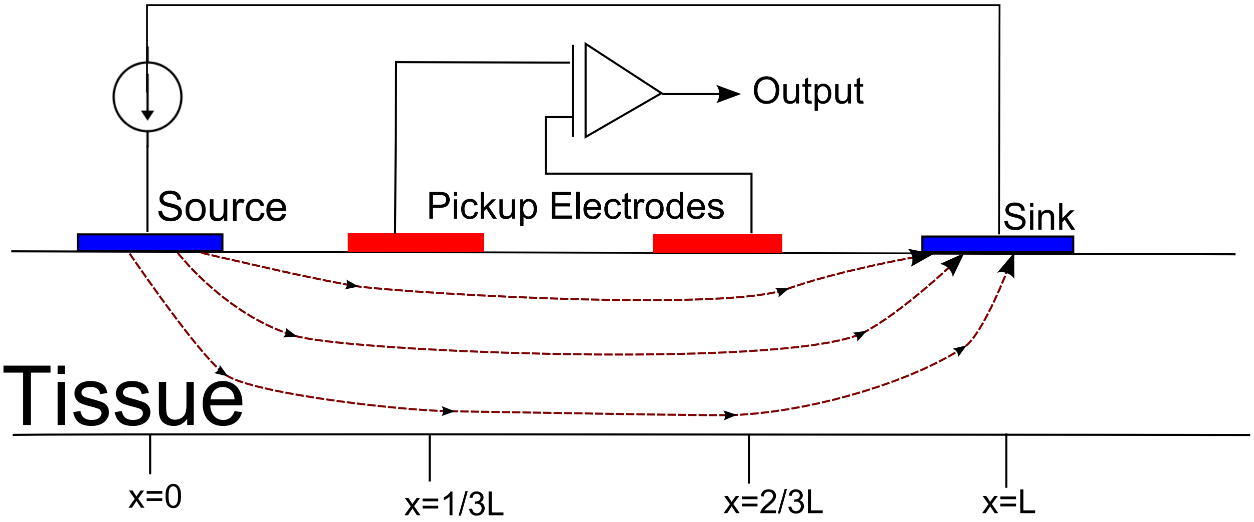

Figure 3.17: Tetrapolar electrode configuration

of the signal. This can be performed with 2, 3, or 4 electrodes. The 4-electrode configuration, referred to as the tetrapolar configuration (figure 3.17), uses a pair of electrodes as a current source/sink, and another pair as a differential pickup. In this configuration, the impedance of the source/sink electrodes do not effect the measurement. The amplifier connected to the pickup electrodes has a very high input impedance; very little current passes through the pickup electrodes and thus the impedance of the electrodes do not effect the measurement. As the tissue impedance changes through respiration, the differential voltage will also changes for a fixed current passing through the tissue. This methodology does not require a strap around the body, and has been demonstrated have have good agreement with the gold standard spirometer[5]. This measurement is susceptible to motion artifacts, yet still can produce good results while the user is undergoing heavy motion[102].

Although there are quite a few methods for assessing respiration, impedance plethysmography is the least invasive as it only uses surface electrodes. Additionally, the differential input electrodes can be shared with the ECG electrodes, requiring only two additional electrodes.

For respiration monitoring, a fixed $50kHz$ signal[8] is typically applied through the chest. A set of single order filters in the range of $10kHz - 250kHz$ will reduce the $50kHz$ signal by $0.7dB$. The $50kHz$ frequency minimizes impedance across the skin (figure 2.13). Both the source and sink electrodes are ideally capacitively coupled to galvanically isolate the subject from the electronics.

A current of $800\mu A$ is often used, though the lower the current, the better as it is safer for the subject. Our target is a current in the range of $200\mu A$.

At $50kHz$, the tissue impedance is quite low ($20\Omega - 50\Omega$ thoracic impedance[15]), and the variation due to respiration is even smaller ($0.1\Omega - 3.5\Omega$[5]). A visual granularity of 10:1 is sufficient to discriminate between inhalation and exhalation, thus our goal would be $0.1\Omega/10 = 0.01\Omega$ signal resolution. A 10:1 visual resolution will require $\frac{ln(10/1)}{ln(2)} = 3.3$ bits of ADC resolution. Assuming that the noise can be quantized to one bit, the SNR can be calculated as $SNR = 20\,log(\frac{10}{1}) = 20$dB.

The distance between the differential electrodes determines the impedance between them, which affects the amplitude of the signal being amplified by the front end. If the impedance is too high, the amplifier can saturate. The respiration signal a small change in this impedance (which

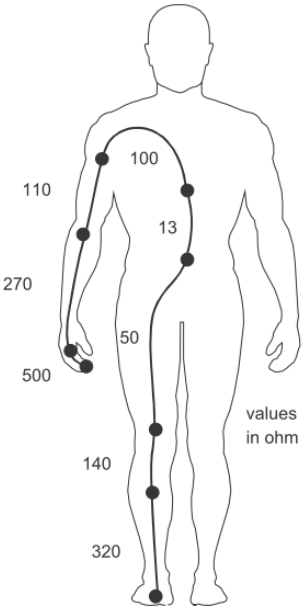

Figure 3.18: Typical body segment resistance values. From [1]

Metric	Value
Current	$200\mu V$
Bandwidth	$10kHz - 250kHz$
Sampling Rate	100Hz
Tissue Impedance	$20\Omega - 50\Omega$
Respiratory Change in Impedance	$0.1\Omega - 3.5\Omega$
Signal Resolution	0.01Ω
Visual Granularity	1:10
Safety Factor	2x

Table 3.6: Design summary for thoracic impedance plethysmography .

can range from $\frac{.1}{50}$ = .2% to $\frac{3.5}{20}$ = 17.5%).

As the signal is fairly high frequency (50kHz), we can implement an aggressive HPF to negate the effects of baseline wander, thus we require a much smaller “safety factor” as compared to the ECG signal. In this case, we can implement a 2x “safety factor”. The safety margin will require one bit of ADC resolution. A design summary is presented in table 3.6.

A sampling rate of 100Hz is sufficient to resolve the respiration signal.

3.4.2 Edema Monitoring

To perform measurements of extracellular body fluid, we need a measure of both the magnitude of the signal as well as the phase[12]. Additionally, the frequency must be swept over a wide range; typically $1kHz$ up to $100kHz$[100] - $1MHz$[41] are used for this application. As a result, the

---

[12] See section 2.3.2

input filters must be able to a much wider range of frequencies. For our application, we desired a maximum frequency of $100kHz$ resulting in a bandwidth of $500Hz - 200kHz$.

The impedance of the tissue varies greatly based on the location being measured. From figure 3.18, we can see the impedance can range from $10\Omega - 500\Omega$ depending on the location. As no short-term time-varying signal is being measured, the concept of a visual granularity does not apply. A fixed complex impedance is being performed per frequency.

3.5 Accelerometry

Physical activity has been demonstrated to be critical for the physical and mental well being of elderly individuals[17]. Body-worn accelerometers can be used to quantify said activity levels in order to provide feedback to the individual and/or the caregiver (section 1.1.4).

Additionally, an accelerometer can be use to categorize the type of activity being performed, referred to as Activities of Daily Living (ADL). Thus, not only is overall activity monitored, but it is possible to categorize the duration and type of activity, such as sitting, standing, walking, or running.

Fall detection is a type of ADL which warrants monitoring. A fall by an elderly individual can result in sever injury and prevent from calling for help. Numerous algorithms have been developed to detect a fall using a single accelerometer (section 1.2.5) .

Activity Monitoring

A waist-worn accelerometer of low complexity is sufficient for quantifying activity. Good correlation between energy expenditure and accelerometer output has been demonstrated using a single-axis $\pm 2g$ accelerometer band-limted to $0.25Hz - 2.5Hz$ and sampled using a 10-bit ADC sampling at 10Hz[37].

Activities of Daily Living

ADL is the classification of everyday activities such as sitting, standing, walking, lying down, etc. Being able to quantify and the types of activities goes a step beyond simple activity monitoring and can provide additional information to the care provider. A hierarchical binary tree has been developed that can classify a wide range of activities with a sensitivity of 97.7% and specificity of 98.7%[86]. Their system utilized a triaxial $\pm 10g$ accelerometer with a bandwidth of $0 - 500Hz$ sampled at $45Hz$.

Fall Detection

Fall detection is a very specific type of ADL, and can be performed using a single accelerometer along with one of many light-weight algorithms (figure 3.19). Sensitivities up to 97% and specificities up to 100% have been achieved using a single waist-mounted accelerometer[57].

Typically, fall detection algorithms work by measuring the magnitude and spacial distribution of accelerometer events (figure 3.20). The authors of these algorithms have validated their systems

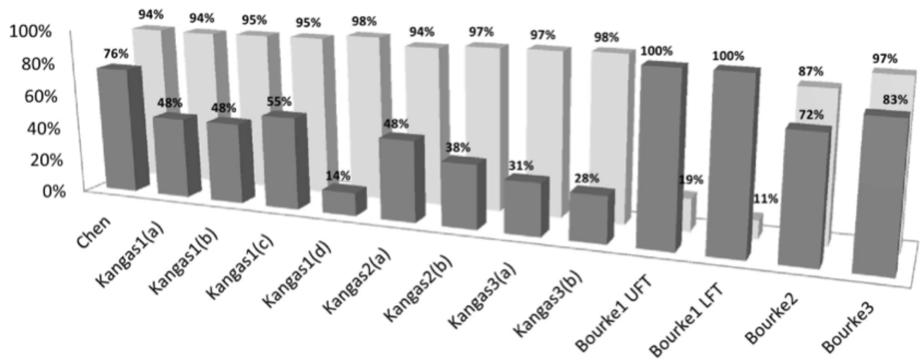

Figure 3.19: Sensitivity (dark colored bars) and specificity (light colored bars) of various fall detection algorithms. From [11]

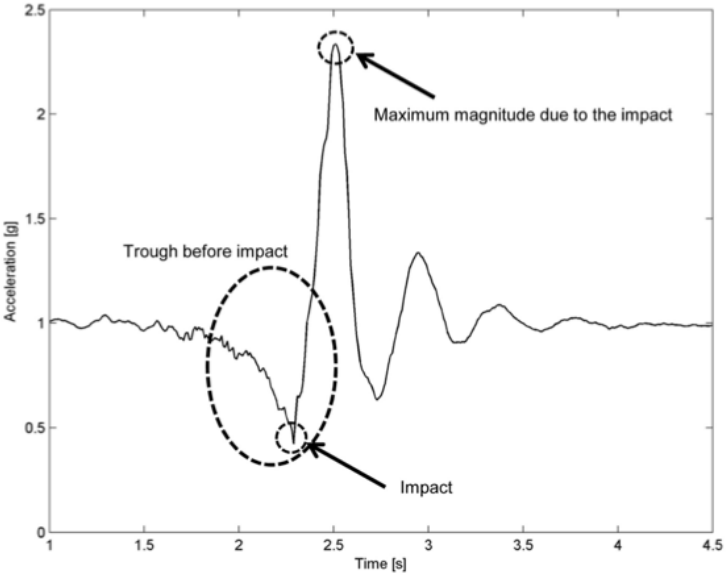

Figure 3.20: Example of accelerometer data used to detect falls. From [11]

	Activity Monitoring	Activities of Daily Living	Fall Detection
Accelerometer Dynamic Range	$\pm 2g$	$\pm 10g$	$\pm 10g$ or $\pm 12g$
Bandwidth	0.25Hz-2.5Hz	0-500Hz	

Table 3.7: Summary of accelerometer implementations for various applications.

using triaxial accelerometers mounted on either the head or the waist, sampled between $50Hz - 250Hz$ with a dynamic range of either $\pm 10g$ or $\pm 12g$ and sampled using a 12-bit ADC[11].

Summary

A summary of the requirements for various accelerometer implementations is provided in table 3.7.

3.6 Overview

In the preceding sections, the design rational was detailed for the various sensing modalities present in *The Berkeley Tricorder*. In most cases, several options and range of values were discussed. The final implementation must also take into account component cost, PCB board space requirements, and power considerations. As a result, the following tradeoffs were made. A final summary is provided in table 3.8.

	ECG	**EMG**	**PPG**	**BioZ**	**Accelerometer**
Physiologic Bandwidth	$0.05 - 150Hz$	$5 - 500Hz$	$0.5 - 2.5Hz$	$.1 - 1Hz$[82]	
Implementation Bandwidth	$0.5 - 150Hz$	$5 - 500Hz$	$0 - 600Hz$		$25Hz$
Sampling Rate	$1000Hz$	$1000Hz$	$100Hz$ per channel	$100Hz$	$1000Hz$
Visual Resolution	25:1		100:1	10:1	
Safety Margin	4x		0	2	
Signal Resolution	$2\mu V$			$.01\Omega$	$3.4mg$
Signal Dynamic Range	$0.05mV - 2.8mV$	noise floor-12mV	$9.1:1^{\dagger}$	$.6\Omega - 171\Omega$	$\pm 8g$

Table 3.8: Summary of implementation details for *The Berkeley Tricorder.* (†) *expressed as a ratio*

Chapter 4

The Berkeley Tricorder

The Berkeley Tricorder is a very small and highly integrated wireless ambulatory health monitor. It integrates an accelerometer, an Electrocardiogram (ECG), an Electromyogram (EMG), a Photoplethysmograph (PPG), a bioimpedance spectrometer, a Bluetooth wireless interface, an SD Card for data storage, and a USB interface (figure 4.1).

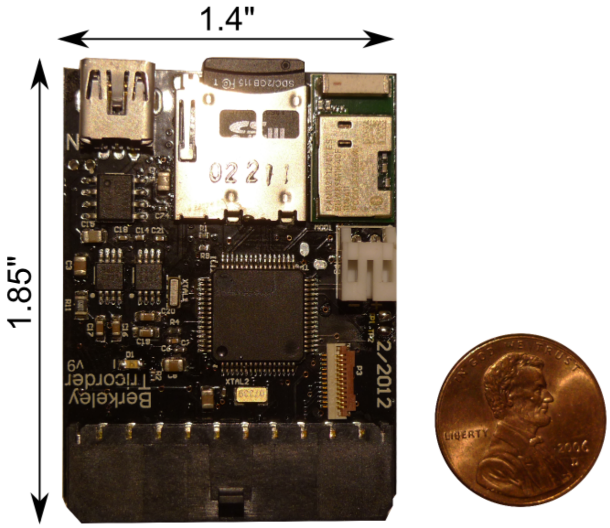

Figure 4.1: The Berkeley Tricorder (Version 9)

4.1 Design Goals

Our primary goal was to produce a highly integrated device which records multiple health parameters while minimizing size and cost. Our other high-level requirements include

- A means of data storage for at least 24 hours, and the ability to transfer the data from the device.
- A means of remote telemetry for real-time data viewing.

Metric	Values
Physiologic Bandwidth	$0.05 - 150Hz$
Implementation Bandwidth	$0.5 - 150Hz$
Sampling Rate	$1024Hz$
Gain	300
ADC Resolution	12-bits
Max Resolution	$2.68\mu V$
System Dynamic Range	$0 - 11mV$
Input Impedance	$2.5M\Omega$

Table 4.1: Summary of the ECG implementation for *The Berkeley Tricorder*

- A comfortable means of wearing the device, concealed under clothing.
- A single device capable of recording multiple biosignals.
- A built-in recharge mechanism.

4.2 Data Aquisition

The following hardware diagram (figure 4.2) is presented to guide as an aid in understanding the big picture of the architecture.

4.2.1 Electrocardiogram (ECG)

Design Goals

The ECG is designed based on the requirements defined in section 3.1 (table 4.1) and the following additional requirements for a standard ECG [116, 121] :

High Level Design

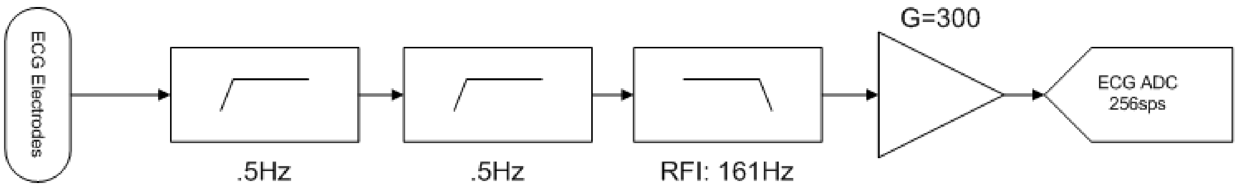

Figure 4.3: ECG front end block diagram

A block diagram of the latest ECG implementation can be found in figure 4.3.

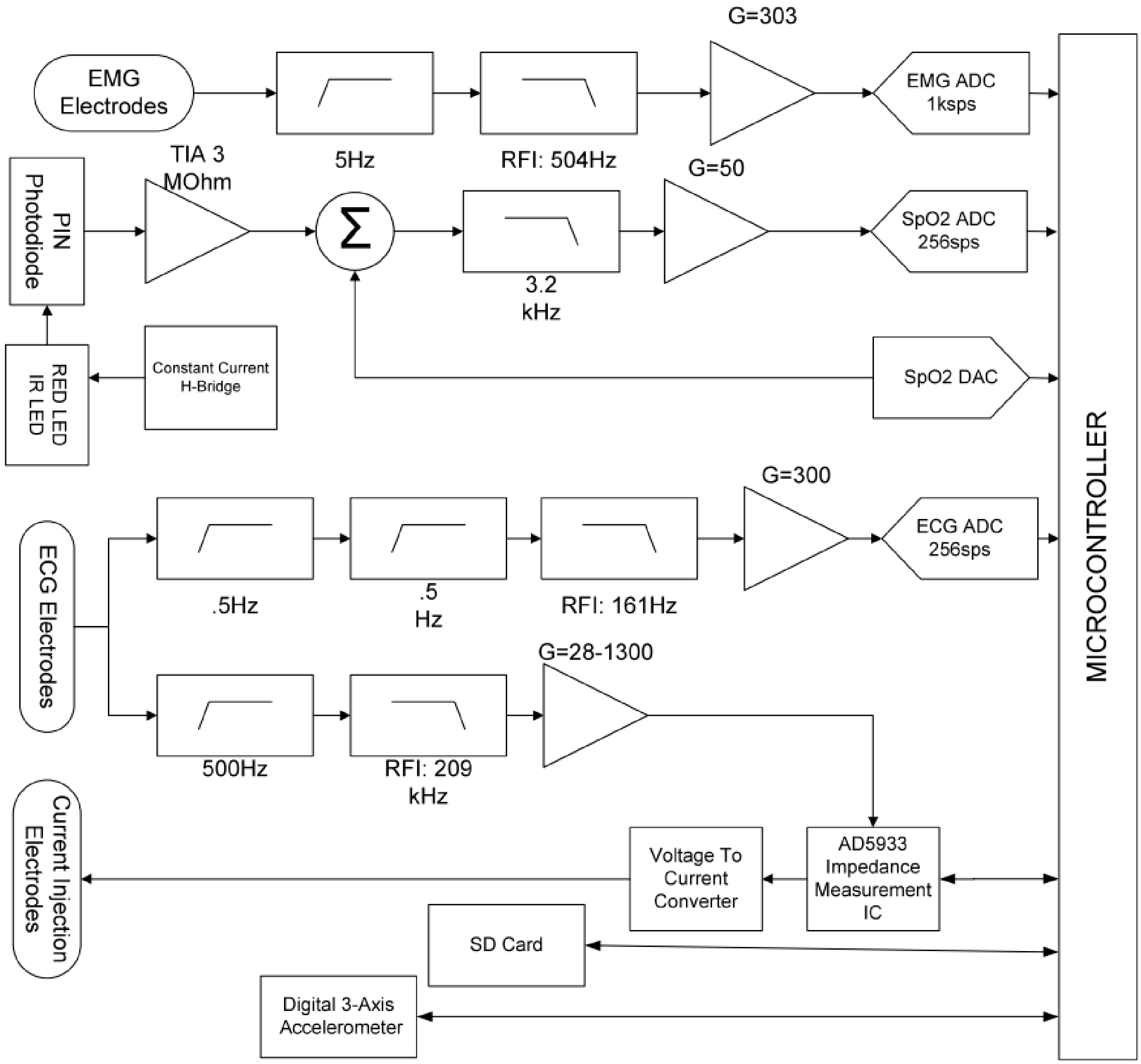

Figure 4.2: The Berkeley Tricorder Hardware Overview

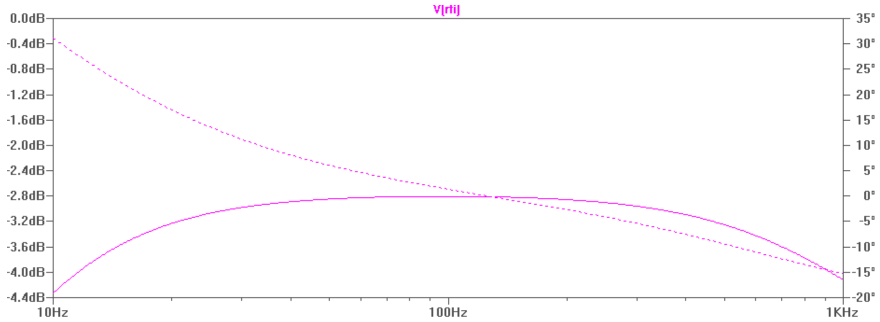

Figure 4.4: ECG filter gain/phase plot. Solid line represents the gain, dotted represents the phase.

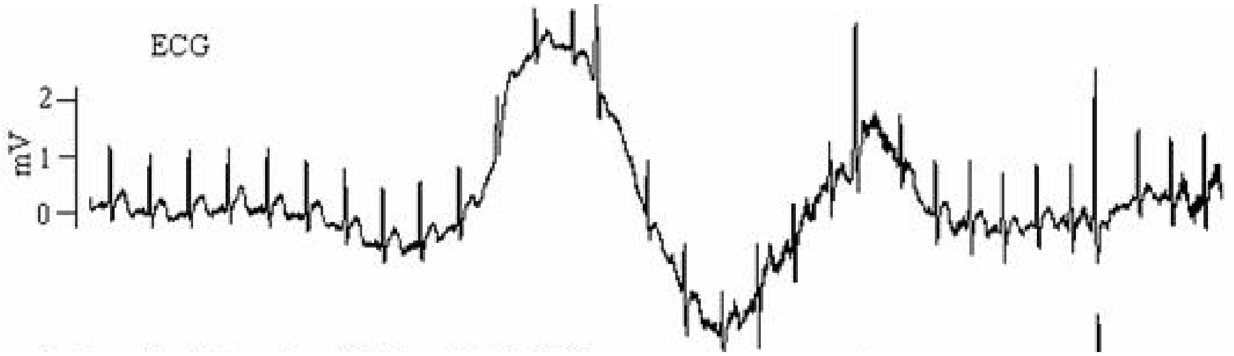

Figure 4.5: Example of ECG Baseline wander. From [29]

	AD627	**AD623**
Max Gain	$1000x$	$1000x$
Input Noise	$38nV/\sqrt{Hz}$	$35nV/\sqrt{Hz}$
Current Noise	$50fA/\sqrt{Hz}$	$100fA/\sqrt{Hz}$
Supply Current	$60\mu A$	$305\mu A$
Input Impedance	$20G\Omega$	$2G\Omega$

Table 4.2: Instrumentation amplifier specifications

Analog Front End

The original ECG implementation consisted of a single order 0.8Hz High-Pass Filter (HPF), but suffered too much offset drift, also known as baseline wander (figure 4.5) causing the signal to easily saturate.

This problem was solved by migrating from a single order to a second order high pass filter at 0.5Hz to minimize this effect. Although a .05Hz -3dB Cuttoff frequency (-3dB) HPF is required to preserve the all the features of the ST segment in the ECG (figure 2.5b), the resulting device would be too prone to motion artifacts and thus the 0.5Hz cutoff was decided upon.

The high-pass filter also has the property of isolating the patient from direct electrical contact through a capacitor, increasing patient safety.

A radio-frequency interference (RFI) filter was required to avoid the high-frequency noise present on the Tricorder (including from the Bluetooth radio) from entering the amplifier, being rectified inside the IC and causing significant low frequency noise [63] (See appendix C for implementation details). The RFI filter adds a 150Hz low pass filter resulting in the gain/phase diagram in figure 4.4.

Instrumentation Amplifier

The instrumentation amplifier needs to have high input impedance, sufficient gain, low noise, and low power consumption. The Analog Devices AD627 fits these requirements (table 4.2), and is available in an SOIC-8 package. Both a $.1\mu F$ and $10\mu F$ bypass capacitors were placed close to the supply pins for to reduce power supply noise, and the output of the is connected directly to an Analog to Digital Converter (ADC) input on the Microcontroller (MCU). The output is biased to mid-supply ($\frac{3.3V}{2} = 1.65V$) through a reference pin on the amplifier.

Metric	**Value**
Physiologic Bandwidth	$5 - 500Hz$
Implementation Bandwidth	$5 - 504Hz$
Sampling Rate	$1024Hz$
Gain	304
ADC Resolution	12-bits
Max Resolution	$2.65\mu V$
System Dynamic Range	$0 - 11mV$

Table 4.3: Summary of the EMG implementation details for *The Berkeley Tricorder*

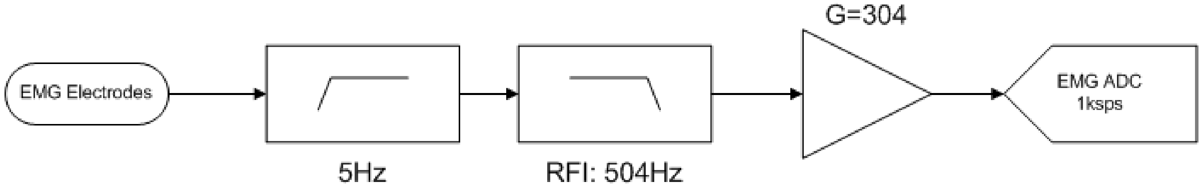

Figure 4.6: EMG front end block diagram

The gain is configured using a single resistor to 300 based on the derivation in section 3.1.

4.2.2 Electromyogram (EMG)

Design Goals

The implementation of the EMG is very similar to the implementation of the ECG in terms of filtering and amplifying a surface biopotential. The EMG is designed based on the requirements defined in section 3.2 (table 4.3)

The high level requirements include:

High Level Design

A block diagram of the latest ECG implementation can be found in figure 4.6.

Analog Front End

The analog front end is similar to the ECG front end, but as the HPF cutoff is at a higher frequency (8Hz) which obviates the need for the second order filter. An RFI filter was used with a differential LPF at 504Hz.

Like the ECG, the series capacitor in the HPF provides galvanic isolation from the Tricorder.

The overall gain/phase profile of the analog front end for the EMG is presented in figure 4.7.

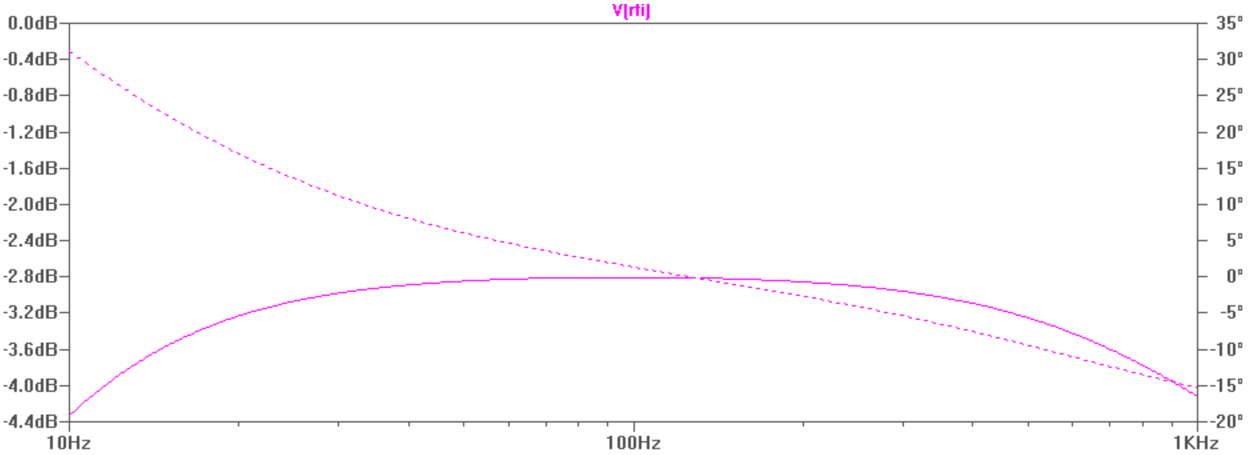

Figure 4.7: ECG filter gain/phase plot. Solid is gain, dotted is phase.

Amplifier

The instrumentation amplifier used for the EMG stage must be able to have sufficient gain at the upper end of the bandwidth, 500Hz. The AD627 used in the ECG stage is not sufficiently fast to support the EMG measurement, and thus the AD623 was chosen (table 4.2). The tradeoff for a faster amplifier is a 5x increase in power consumption, a 2x increase in current noise, and a lower impedance input.

4.2.3 Pulse Oximetry (SpO$_2$) / Photoplethysmograph (PPG)

Our goal is to measure the small variation of blood volume in the target arterial vessels by emitting light, and measuring the level of light either transmitted through the tissue or reflected due to back-scattering from the tissue. For pulse detection, we need only one light source; for blood oxygenation percentage (SpO_2) we need to use two light sources that are in close proximity. The high-level design requires

- Light-Emitting Diodes (LEDs) & PIN photodiode for the physical sensor
- Constant current source to drive LEDs
- Transimpedance amplifier to convert current from PIN photodiode to a voltage
- Circuit to remove DC offset from the signal and amplify the small AC waveform
- Minimum sampling rate [2]: 100Hz

High-Level Design

There are a number of methods by which a PPG system can be implemented for Oxygen Saturation Percentage (SpO$_2$) measurement. Some sample topologies from other implementations are presented in figures 4.8 & 4.9. The topology for the PPG implementation in *The Berkeley Tricorder* is presented in figure 4.10. All these systems require:

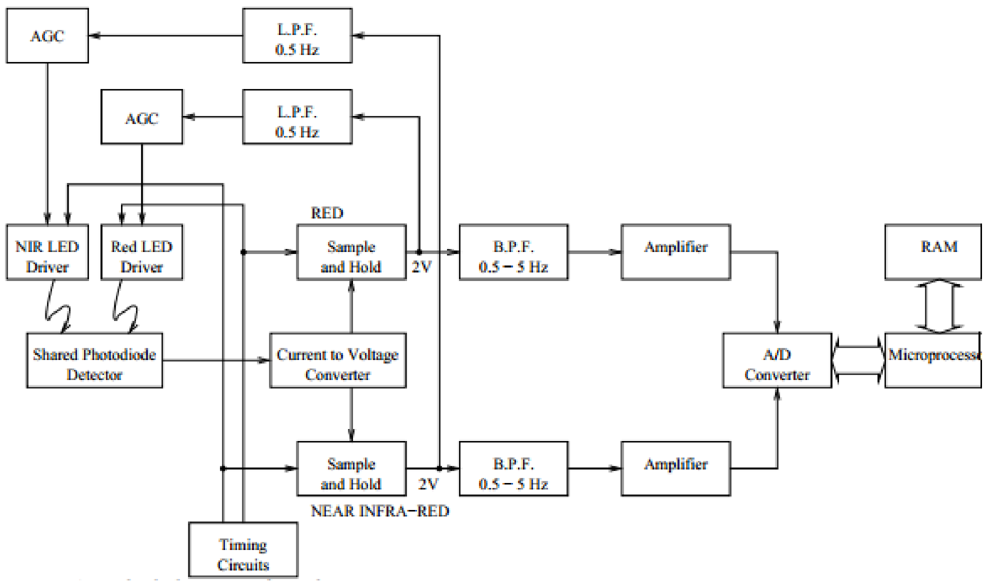

Figure 4.8: Block diagram of SpO_2 circuit. From `http://www.robots.ox.ac.uk/~neil/teaching/lectures/med_elec/notes6.pdf`

1. To generate a current to drive one of two LEDs.
2. Measure the incident light on a photodiode by converting the generated current to a voltage. This generates a DC signal with a small AC signal superimposed.
3. To measure the DC components of the two signals, and optionally adjust the LED current to make the DC values from the two LEDs equal.
4. To further amplify the AC component of the two signals in order to measure their amplitudes.
5. To compute the ratio $R = \frac{DC_{IR}}{DC_{RED}} \frac{AC_{RED}}{AC_{IR}}$ which is used to compute the oxygen saturation percentage through an empirically derived look-up table. Optionally, heart rate can be computed by measuring the time between pulses.

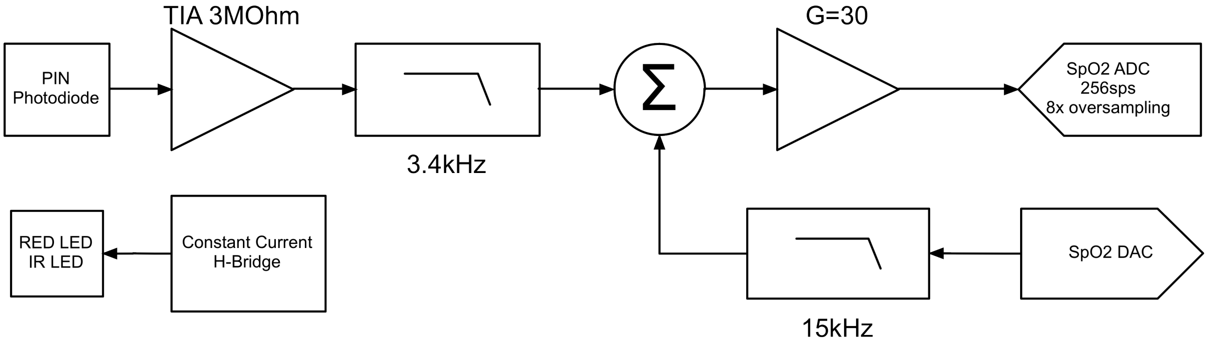

Figure 4.10: Block diagram of PulseOx Circuit

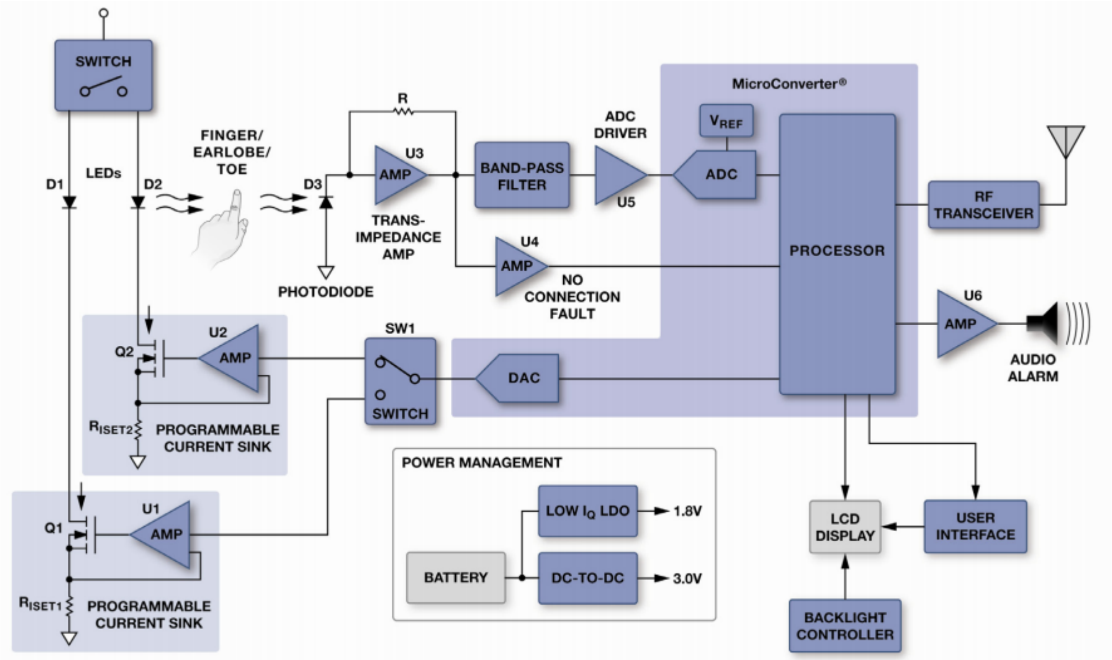

Figure 4.9: Block diagram of SpO_2 circuit. From [10]

There are multiple ways these sets of steps can be implemented. The LEDs are only illuminated at one time. The LED drive circuit depends on the configuration of the LEDs. In figure 4.9, they are driven separately, though many times they found with the anodes and cathodes connected (figure 4.11). The LEDs can be driven using a fixed current source, or a variable current source controlled by a Digital to Analog Converter (DAC) or digital potentiometer.

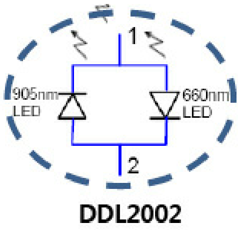

Figure 4.11: LED pair for pulse oximetry. (DDL2002 from APMK)

As stated, some implementations will adjust the DC components of the signal so that their values cancel in computing the ratio, R, so that the DC value does not need to be measured (figures 4.8, 4.9). This is performed by adjusting the ratio of the currents to the two LEDs, and a feedback loop must be deployed as these values will change over time. Otherwise, the DC voltage must be measured by an ADC or computed through some other means.

The AC signal is very small compared to the DC offset and it requires further amplification. There are many ways this can be accomplished. The simplest option is to pass it through a HPF to remove the DC offset. Or it can be adjusted by averaging it with a second signal, or by feeding it through a differential amplifier to subtract off the DC offset (as either a fixed offset subtraction or a variable offset subtraction controlled by a DAC). Or it can be fed directly into an ADC which is configured to have its $ADC_{dynamic\ range}$ vary narrow and in the range of the DC value.

The following sections describe the design choices implemented in *The Berkeley Tricorder*, and the rationale.

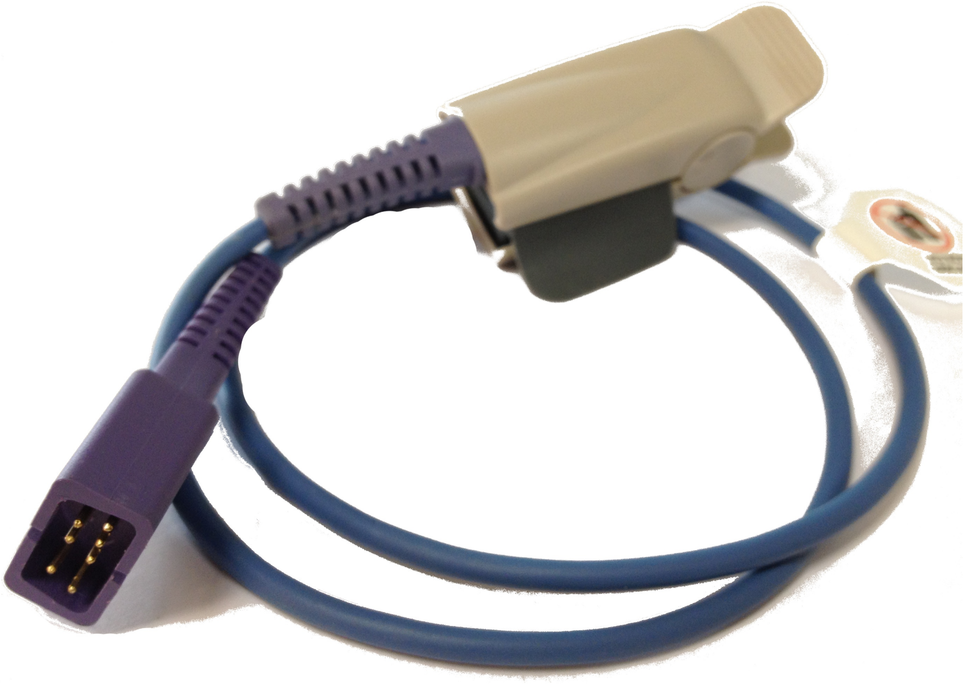

Figure 4.12: Nellcor$^{\mathrm{TM}}$transmissive finger pulse oximeter sensor with DB9 connector

Pin	**Name**	**Description**
9	Photodiode Cathode	Green Wire
5	Photodiode Anode	White Wire
7	Shield	Cable Shield
2	LED1	Red Wire; Anode of Infra-Red (IR) LED, Cathode of red LED
3	LED2	Black Wire; Cathode of IR LED, Anode of red LED

Table 4.4: Pinouts for Nellcor$^{\mathrm{TM}}$series of Pulse Oximeters (from `http://pinouts.ru`)

Sensor

By making our device compatible with existing commercial sensors, we solve a number of problems including optimizing the LED wavelength, LED optics, mechanical system, shielded cables, and photodiode selection. Many man-years of research have gone into optimizing these commercial sensors, which we can take advantage of. However, as the detailed specifications of the LEDs or photodiode used in these devices are proprietary, and thus required a number of educated guesses about the hardware specifications as well as a number of iterations to optimize the system. Additionally, they are found in different form factors for application on the finger, earlobe, and forehead – and are designed to be either reusable or disposable.

The design was based around the Nellcor$^{\mathrm{TM}}$transmissive finger pulse oximeter sensor with D-suBmnituature 9-Pin (DB9) connector (figure 4.12). Nellcor$^{\mathrm{TM}}$manufactures a wide range of sensor all using the same DB9 connector and pin configuration making them all compatible (table 4.4). Additionally, a wide range of inexpensive Nellcor$^{\mathrm{TM}}$clones exist on the market.

The internals of their sensors are quite simple (figure 4.13). They utilize a PIN photodiode

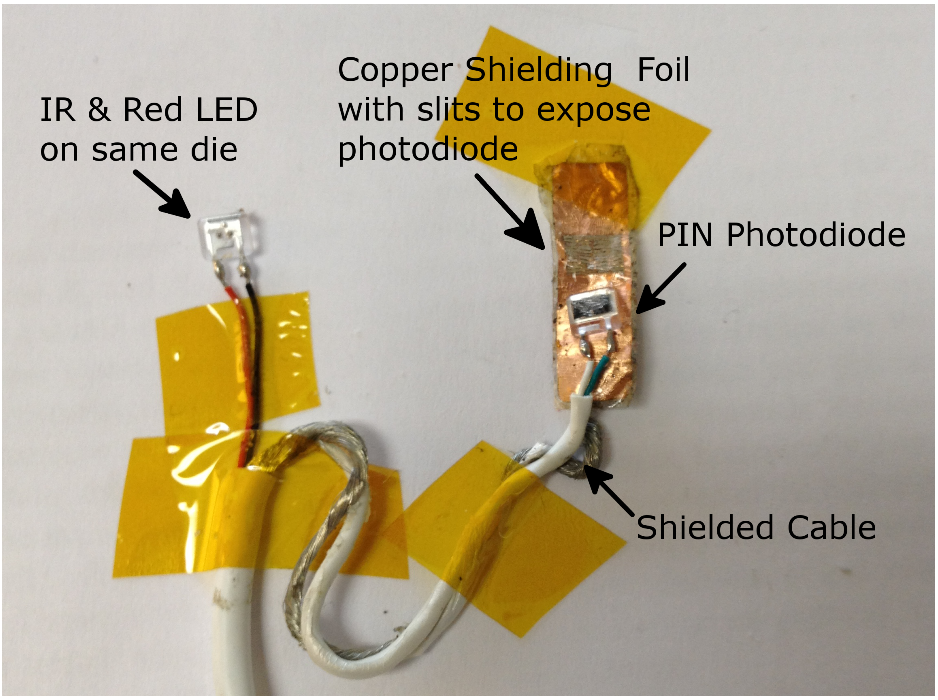

Figure 4.13: Nellcor™transmissive finger pulse oximeter sensor dissected

with a large surface area covered by a copper shield with slits cut out. The heavy shielding is required as the photoplethysmographic signal is quite small and highly susceptible to outside noise. Additionally, their light source is a dual IR & red LED on the same die to ensure that the optical path is as identical as possible for the two wavelengths of light[1]. The LED pair is configured with the anode of one connected to the cathode of the other, thus only two wires are required to drive it (figure 4.11). Depending on which line voltage is high and which is grounded, either the red or IR LED will illuminate. It is thus impossible for both LEDs to be illuminated simultaneously.

---

[1] The importance of this was described in section 2.2

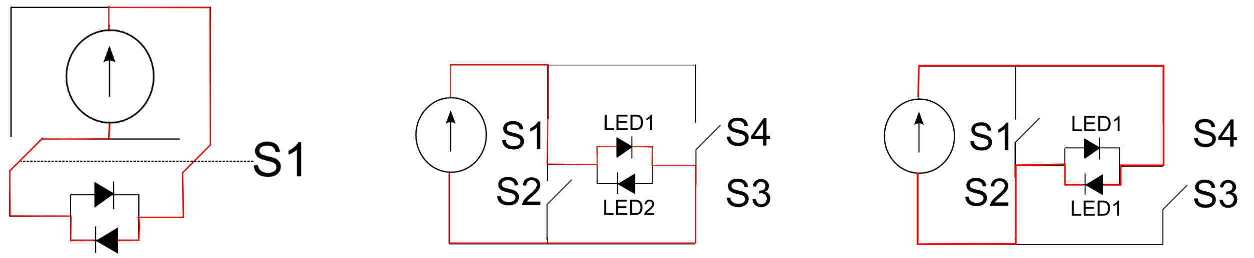

(a) A DPST multiplexer connected to a current source. Both switches are controlled by a single switch

(b) An H-Bridge with switches S1 and S3 closed. LED1 is illuminated.

(c) An H-Bridge with switches S2 and S4 closed. LED2 is illuminated.

Figure 4.15: A multiplexer and H-bridge used to control the direction of current flow.

LED Driver (Current Source)

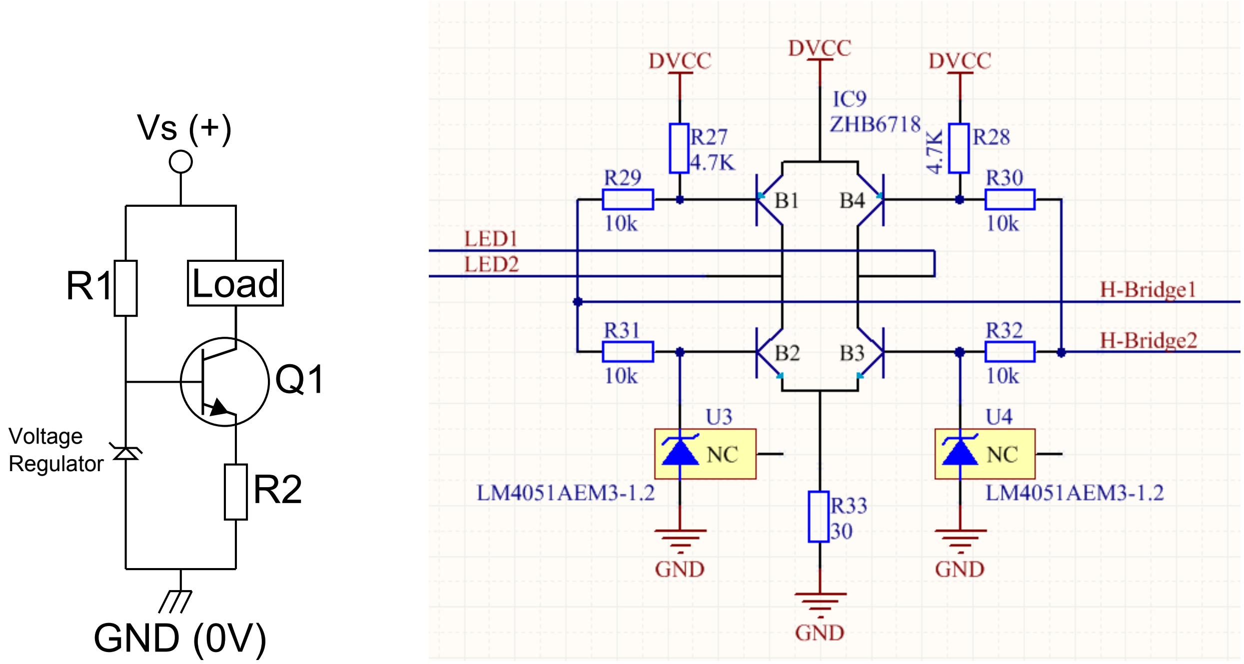

(a) BJT based constant current source. The voltage regulator pictured is a zener diode. Figure adapted from Wikipedia.

(b) Constant current LED driver

Figure 4.14: Constant Current/LED Driver Circuits

The simplest implementation would be to tie the led pair to two Input/Output (I/O) pins from the microcontroller. The microcontroller can set a pin as either as source or sink, and thus can direct the flow of current. However, the current from the microcontroller I/O pins would be sourced from the digital supply lines and thus very noisy (figure 4.31, bottom trace). The I/O pins are also limited to a few *mA* maximum current which is not sufficient. Other options include multiplexers,

Figure 4.16: Supply voltage noise from LED coupled to SpO_2 signal.

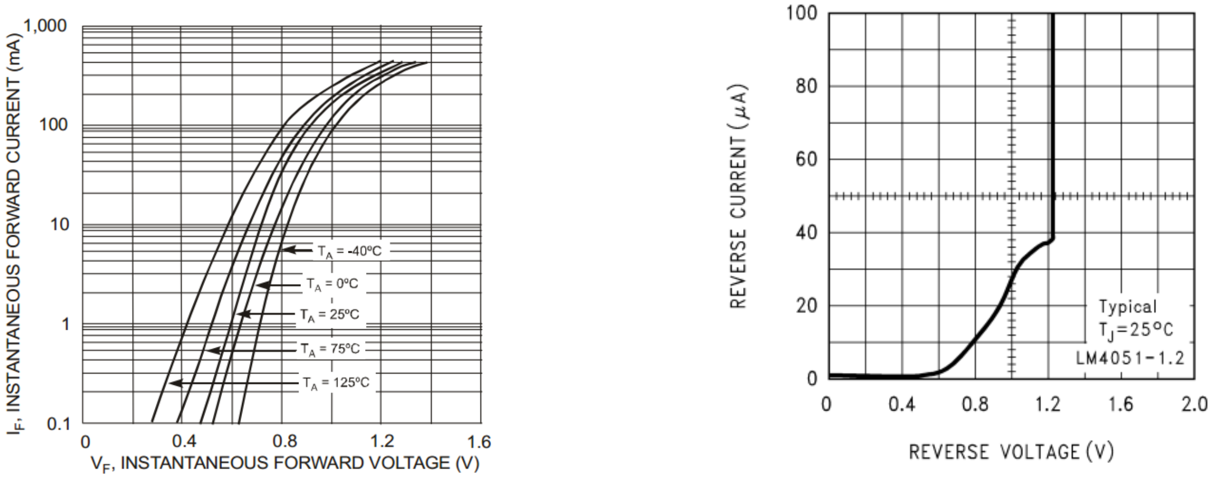

(a) I-V Curve of original diode (mmbd4448hcqw).

(b) I-V Curve of voltage reference diode (lm4051).

Figure 4.17: IV curves of diode vs. voltage reference

or digital switches, to redirect the flow of current (figure 4.15a), and an H-bridge (figures 4.15b and 4.15c). A multiplexer is typically a discrete device with a number of Field-Effect Transistors (FETs) internal to the device. H-bridges are constructed out of 4 FETs or BJTs with the express purpose of controlling the direction of current flow.

Of the many different implementations of a current source, a standard method involves a NPN BJT, a resistor, and a constant voltage source (figure 4.14a). The BJT maintains a constant voltage across the the base and emitter, referred to as V_{be}. This voltage is typically in the range $0.6 - 0.7V$. If a voltage, V_b, appears on the base, then the voltage on the emitter will be $V_e = V_b - V_{be}$. This voltage also appears on the top of resistor R_2, and induces a current to flow through the resistor equal to $I_R = \frac{V_e}{R}$, or $I_R = \frac{V_b - V_{be}}{R}$. The current flowing through the resistor comes in part from the base, and in part from the collector. The ratio of current from the collector to the current from the base is referred to as β, and is typically a large value. Thus, we can compute the ratio of current flowing through the load (or LED) to the current flowing through R_2as

$$I_{LED} = I_R(\frac{\beta}{\beta + 1})$$

Substituting I_R

$$I_{LED} = (\frac{V_b - V_{be}}{R})(\frac{\beta}{\beta + 1})$$

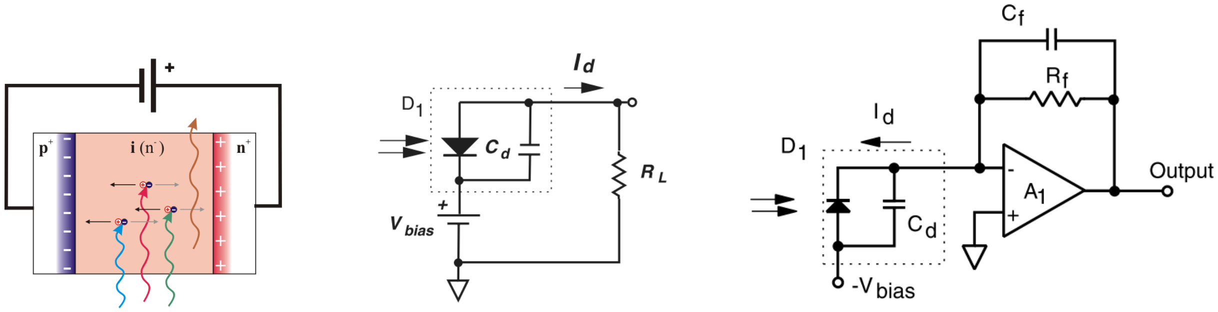

(a) PIN Photodiode. Adapted from wikipedia.

(b) PIN photodiode with load resistor. From [53]

(c) PIN photodiode with transimpedance amplifier. From [53]

Figure 4.18: PIN Photodiode and it's application.

Assuming that β is fairly large, we can approximate $\frac{\beta}{\beta+1} = 1$, thus

$$I_{LED} = (\frac{V_b - V_{be}}{R})$$

Thus we can control the current through the LED by controlling V_b.

As stated, H-bridges can be made out of 4 BJTs, with S2 and S3 consisting of NPN transistors. Thus, by using a BJT based H-bridge, we can not only control the direction of current flow, but also control the current (figure 4.14b). This configuration significantly reduces part count and cost as compared to other methodologies. A Zentex ZHB6718TA H-bridge was used for this application.

The remaining component in this design is the constant voltage source. The initial design used two diodes in series in place of the zener diode in figure 4.14a. The voltage drop across a resistor is typically fixed at around $0.6V$. Two resistors in series should produce a fixed voltage of $1.2V$. However, we found the resistors were insufficiently stable and coupled noise from the digital supply whenever the Secure Digital (SD) card was written to (figure 4.16) . This was a result of the diode not conducting fully at a fixed voltage, but rather conducting over a range of voltages (figure 4.17a).This was replaced with a precision voltage reference to maintain a constant voltage of $\sim 1.2V$ (figure 4.17b).

Based on examination of a number of other PPG implementations, a target of $20mA$ was desired for the LED. The current is set by R33 and U3/U4 (figure 4.14b). In the case mentioned where the IR LED is illuminated, B2 is conducting. U3 sets the base voltage to 1.225V. B2 has a $V_{BE,sat}$ of 0.62V resulting in a voltage across R33 of $1.225V - 0.62V = .605V$. R33 is then used to limit the current to $.605V/30\Omega = 20mA$. The LEDs are cycled on/off with an overall duty cycle of 50%, thus the LED stage draws $20mA/2 = 10mA$ of current.

Detector and Amplification

There are additionally many different light intensity detectors that can be used. Typically, one finds photodiodes and phototransistors used in these applications. Phototransistors generate signal gain internally but also generate more noise than photodiodes. Photodiodes aditionally are linear over a very wide dynamic range[21].

(a) PIN photodiode capacitance.

(b) PIN photodiode current from incident light.

Figure 4.19: Sample data from the datasheet for TEMD5010X01.

A PIN photodiode is a diode with an additional exposed middle layer consisting of lightly n-doped silicone, called the intrinsic layer (figure 4.18a). When a photon of sufficient energy strike the depletion layer, an electron is released and flows to produce current. This current needs to be converted into a voltage in order to be digitized.

Photodiode Current to Voltage

The simplest approach is to put the PIN photodiode in series with a large resistor. The resulting voltage is a product of the resistance and current ($V = IR$). Examination of figure 4.18a, you will notice the diode resembles a capacitor as well, with a positive and negative side separated by a low conductivity depletion layer. The implication is that there is a capacitor parallel with the PIN photodiode, and will form a Low-Pass Filter (LPF) in conjunction with the load resistor (figure 4.18b). This reduces the maximum bandwidth significantly, and is no longer suitable for the switching speeds required to alternate between the two LEDs. Additionally, the larger the surface area of the photodiode, the more sensitive it is to incident light. However, the larger the surface area, the larger the capacitance value of the photodiode.

One approach to reducing the effects of this capacitance, C_d, is to reverse bias the photodiode. The effect of reverse biasing it is to increase the width of the depletion layer. The capacitance of a parallel place capacitor is inversely proportional to the distance between the plates. Thus, increasing the width of the depletion layer has an equivalent effect to increasing the distance between the electric plates and reduces the capacitance. However, the effect of this is to decrease the dynamic range of the system (figure 4.21), as the resultant voltage is also equally biased. As stated, we have no knowledge of the specific PIN Photodiode used, but by examining the characteristics of a comparably sized photodiode (figure 4.19a) we can see that even half of a volt of reverse bias can reduce the diode capacitance by $30pF$. A value of $0.57V$ of reserve bias was chosen as a compromise between reduced diode capacitance while maintaining a reasonable dynamic range after amplification of $2.73V$.

Another technique used for high speed digital optics is to use a transimpedance amplifier (figure 4.18c). A Texas Instruments OP381 transimpedance amplifier is used to convert the current from

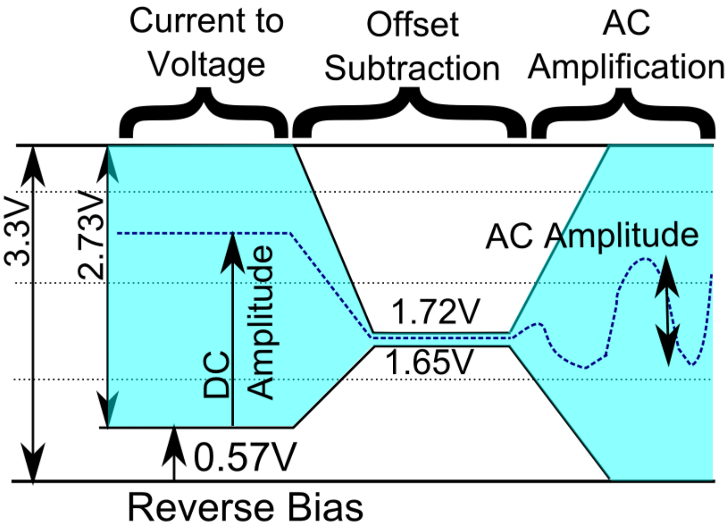

Figure 4.20: Signal voltages through PPG system. Blue color indicates a valid ranges with example signal displayed.

the photodiode to a voltage. The amplifier is very low noise and rated up to 18MHz gain-bandwidth with low current requirements. A transimpedance amplifier uses feedback to maintain the voltage across the capacitor constant[2], and thus helps to mitigate the problem associated with using only a resistor to convert the current to a voltage. A gain resistor, R_f converts converts the current to a voltage, and the addition of a capacitor, C_f, parallel with R_f sets the -3dB bandwidth of the amplifier to $\frac{1}{2\pi R_f C_f}$.

Amplification, Duty Cycle, and Timing

Unfortunately, as our design calls for the use of a 3rd party LED and PIN Photodiode, it becomes difficult to know what gain should be set. The original transimpedance gain was chosen to be $5M\Omega$ based analysis of similar implementations, and later reduced to $3M\Omega$ to minimize signal saturation. The $2.73V$ dynamic range allows us to resolve $\frac{2.73V}{3M\Omega} = 0.9\mu A$ of current from the photodiode, or about $\frac{0.01mW}{cm^2}$ based on our sample photodiode specifications (figure 4.19b).

The bandwidth of the PPG signal is quite low, in the range of $0.5 - 2.5Hz$[96] (figure 3.15), however the bandwidth of the signal does not drive the design of the Analog Front End (AFE). Rather, we need to acquire the intensity of the two LEDs as well as that of the dark current and external light that leaks into the sensor when the LEDs are turned off. As stated, the typical sampling rates for a PPG range from $75Hz$ to $250Hz$.

The pulse oximeter was added to *The Berkeley Tricorder* after version 4, and thus the PPG design was constrained so as to operate within the existing architecture. This consisted of a main sampling loop that operated at $256Hz$, or $3.9mS$ per cycle (figure 4.27). Thus, the 256Hz sampling rate was chosen in accordance with the higher published sampling rates for a PPG implementation.

Over the course of $3.9mS$, 3 measurements are required to measure the light intensity from

---

[2] This assumes infinite open loop gain from the amplifier, but serves as a reasonable assumption for the frequency range we will be operating in.

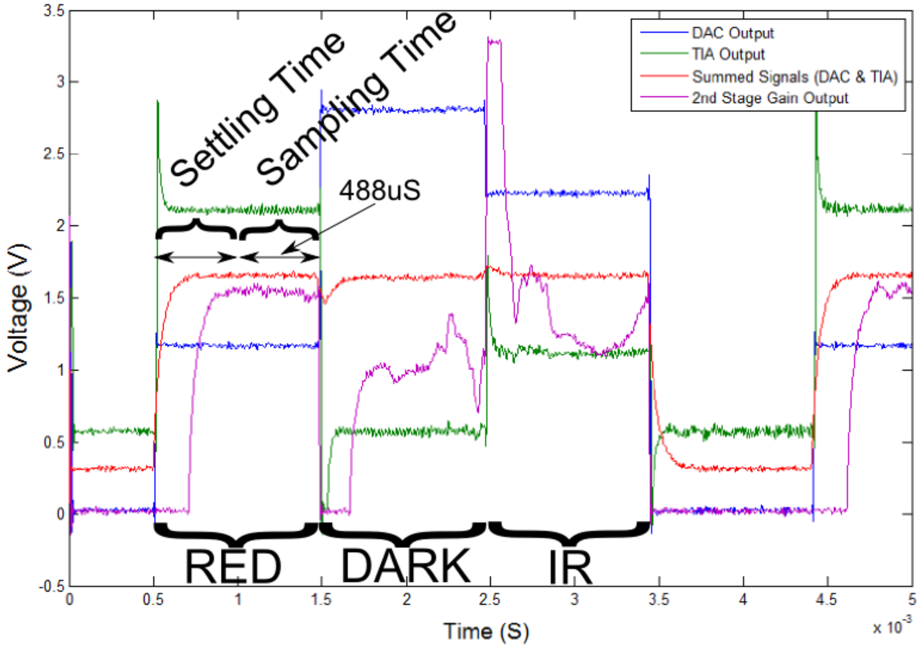

Figure 4.21: Voltages from a number of stages in the PPG acquisition cycle. The purple trace is the output that is digitized. The high level of noise is due to a very electrically noisy test environment.

the red LED, the IR LED, and when no LED is illuminated (the dark current/background light). In order to accomplish this, the LEDs need to be switched on, and time must be allotted to allow the amplifier and filters to settle followed by sampling of the signal using the ADC. In order to accomplish this, the $3.9mS$ is divided into 8 segments (each consisting of $\frac{3.9mS}{8} = 488\mu S$)[3].

In the first segment, the red LED is turned on, the DAC output is configured, and the amplifier is allowed to settle for $488\mu S$. In the following segment, 8 samples are taken by the ADC and summed to help increase the Signal to Noise Ratio (SNR). The same two steps are repeated with both LEDs off, and with the IR led turned on. No measurements are performed in the next two segments to reduce power consumption.

The implication of this system is that the AFE must settle to within 99.99% of the final voltages within 488uS. A LPF is formed by the transimpedance feedback resistor and capacitor is governed by the relationship

$$V = V_o(1 - e^{-t/\tau})$$

Where V is the output voltage,V_o is the input voltage (which is the product of the photodiode current and the feedback resistor, R_f), t is the time in seconds, and $\tau = R_f C_f$ is the time constant. The PPG circuit also implements a second LPF (to be discussed), and thus the output of the system is the product of two low-pass responses.

$$V = V_o(1 - e^{-t/\tau})(1 - e^{-t/\tau})$$

In order to get the output value to within 99.99% of the input value, we set $V = .9999V_o$ and solve for τ in terms of t.

---

[3] See section 4.3.1.1 for further details on the timing implementation.

$$.9999V_o = V_o(1 - 2e^{-t/\tau} + e^{-2t/\tau})$$

$$.9999 = (1 - 2e^{-t/\tau} + e^{-2t/\tau})$$

Substituting our setting time for $t = 488\mu S$, and solving for τ yeilds

$$\tau = 0.10t$$

$$\tau = 0.10(488\mu S)$$

$$\tau = 48.8\mu S$$

In other words, to get the filters to settle within 99.99% of the target value, the time constant (τ) of the various filter stages were set to be 1/10 of the settling time, or $\sim 50\mu S$.

As stated, DC gain of the system is set by R_f to $3M\Omega$. Thus we can solve $\tau = R_f C_f = (3M\Omega)C_f = 48.8\mu S$, or $C_f = 48.8\mu S/3M\Omega \approx 16pF$. The bandwidth of the amplifier is thus set to $\frac{1}{2\pi 48.8\mu S} = 3.2kHz$.

DC Bias Adjustment, AC Amplification

Once the photodiode current is amplified, we need to be able to amplify the small AC component. This can be accomplished through a number of methods, as mentioned. However, at this point in the design, we had access to a free DAC output from the microcontroller. Using a pair of resistors, we c average the voltages of from the Transimpedance Amplifier (TIA) and the DAC, thus moving the signal into a narrow band where we can apply a second stage of gain (figure 4.20). This approach requires minimal additional components and avoids the use of a HPF stage to re-bias the signal, which would distort the low frequency components. It also allows for rapid adjustment of the DC offset to compensate for any baseline wander.

The range of possible output voltages from the TIA is $0.57V - 3.3V$. The DAC can output $0V - 3.3V$. Thus, a $3.3V$ signal from the TIA can be biased down to $\frac{3.3V+0V}{2} = 1.65V$, and a $0.57V$ signal can be biased up to $\frac{0.57V+3.3V}{2} = 1.93V$.

The addition of a capacitor at this averaging point allows us to implement the second LPF stage. The DAC is capable of sourcing or sinking up to $1mA$ of current. The use of a $10k\Omega$ summing resistor will limit the maximum current flow to $\frac{3.3V}{10k\Omega} = 330\mu A$, well under the $1mA$ maximum. As stated in the previous section, the desired time constant is $48.8\mu S$. The capacitor value is thus computed as $C = \frac{\tau}{(R \| R)} = \frac{48.8\mu S}{10k\Omega/2} = 9.76nF$.

We would also like to amplify AC signal with a gain of 50[4]. Given an ADC with an $ADC_{dynamic\ range}$of 3.3V, we can compute the $system_{dynamic\ range} = \frac{ADC_{dynamic\ range}}{G} = \frac{3.3V}{50} = 66mV$. As the minimum guaranteed DC voltage we can get by the use of the DAC is $1.65V$, we can configure an amplifier to work over the range of $1.65V$ to $1.65V + 0.066V = 1.72V$ (figure 4.21). The output of this signal is then fed into the ADC.

---

[4] The first versions implemented a gain of 30 based on other PPG implementations we examined, but we found the AC signal amplitude small and thus increased the gain to 50.

Metric	**Value**
Implementation	BJT-Based H-bridge with integrated current source
Current	$20mA$

(a) Current to light

Metric	**Value**
Implementation	PIN Photodiode with Transimpedance Amplifier
Gain	$30M\Omega$
Reverse Bias	$0.57V$
Dynamic Range	$0 - 90nA$
Bandwidth	$3.2kHz$ ($\tau = 48.8\mu S$)

(b) Light To Current

Metric	**Value**
Implementation	Averaging of signal with DAC output
Bandwidth	$3.2kHz$
Max DAC Current	$330\mu A$

(c) DC Bias Adjustment

Metric	**Value**
Implementation	Non-Inverting Amplifier
Resolution	$180pA$
Gain	50

(d) AC Amplification

Table 4.5: Summary of requirements for PPG implementation for the various stages.

Summary

A summary of the PPG implementation details is provided in table 4.5

4.2.4 Bioimpedance Spectrometer (Respiration & Edema)

Design Goals

During respiration, the geometry of the thorax changes which alters its impedance. Thus, by measuring the impedance of the chest, we can derive the respiration rate and tidal volume[101]. Additionally, an analysis of the impedances at different frequencies can determine the relative amount of fluid in the intra- vs. extra-cellular space (i.e. water compartmentalization, edema) .The design requirements include:

- Signal generation at 50kHz with a fixed current (for Respiration)
- Signal generation over a range of frequencies (for Edema)

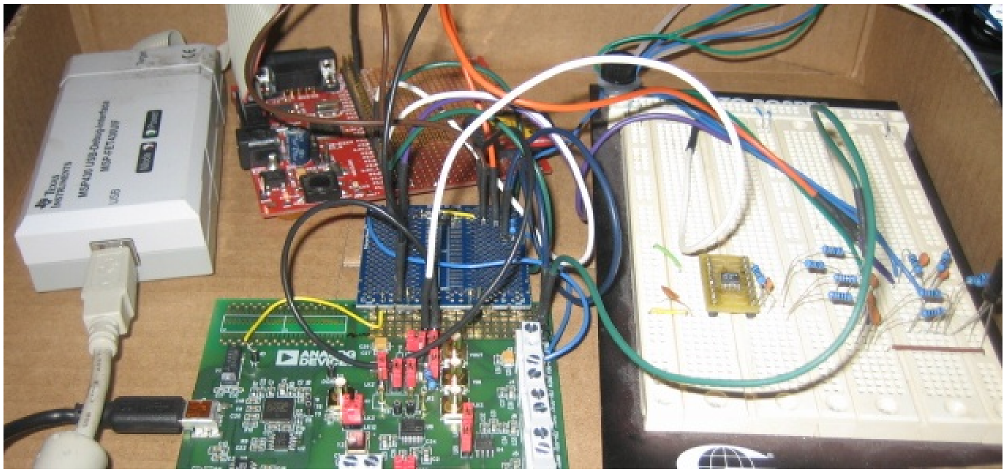

Figure 4.22: AD5933-Based BioZ implementation breadboard

- Support for a tetrapolar electrode configuration
- 0.01Ω resolution
- Complex impedance measurements (for Edema)

Background

The implementation of *The Berkeley Tricorder* has gone through several design iterations, each with different requirements. The various implementations will be briefly discussed followed by a discussion of the final circuit.

The initial implementation (see appendix, figure B.1) utilized a stable oscillator with quadrature output. The in-phase output was passed through a variant of the Holand current source to provide a fixed current independent of the tissue impedance. The output of the differential amplifier was fed to a demodulator along with the oscillator outputs which determined the in-phase (I) and out-of-phase, or quadrature (Q), components of the signal. This method provided not only the amplitude of the signal but the phase as well. This version was never built, due to the high component count and Printed Circuit Board (PCB) real-estate required.

A second method (see appendix, figure B.2) was explored that used a digital quadrature demodulation scheme. This method relied on a square wave of $100kHz$ being generated from the microcontroller, low pass filtered to make it sinusoidal, and fed into a simpler voltage to current converter. The output of the differential amplifier was then fed into Tayloe Detector circuit to demodulate the I/Q signals. The implementation of this circuit was significantly easier than the analog implementation, but this version was also never built.

The final implementation which was prototyped (figure 4.22) and built was based around the Analog Devices AD5933 Impedance Converter Integrated Circuit (IC). The AD5933 was chosen as it greatly simplified the implementation; it provides a programmable frequency generator ($1kHz - 100kHz$ with a resolution of $0.03Hz$), built-in I/Q demodulation, and a 16-bit complex output. The AD5933 samples the signal at 1MHz at 12-bits, performs a Fourier transform of the data, and computes the complex impedance for only the frequency of interest. This method is

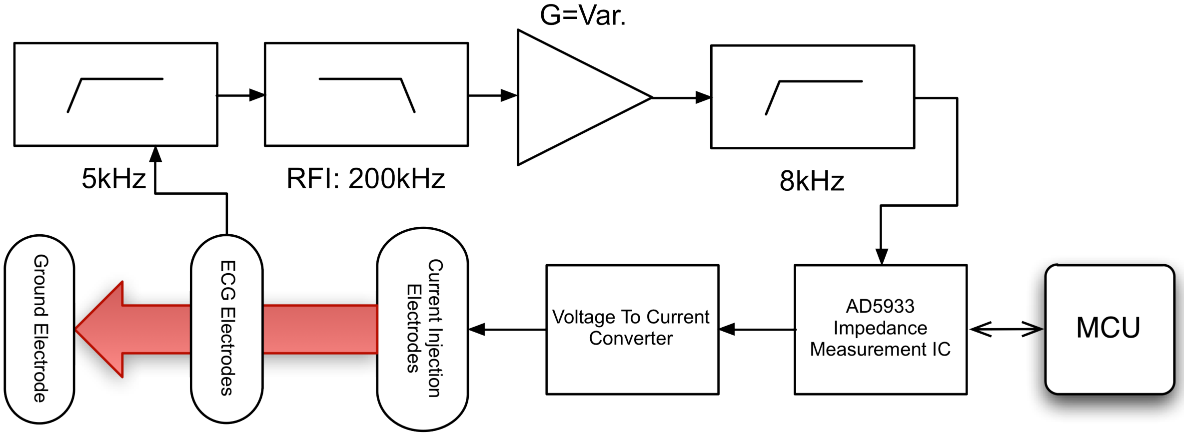

Figure 4.23: Bioimpedance front end block diagram. The red arrow represents the flow of current through the tissue.

highly immune to any noise outside the frequency being measured. The AD5933 is controlled over an Inter-Integrated Circuit (I^2C) bus by the MCU. There have been several groups that have used the AD5933 for biological applications[7, 9, 100], though none has published the front-end implementation details.

The basic function of the AD5933 is that it can generate a signal with a frequency from 1kHz-100kHz into a load of $1k\Omega - 10M\Omega$, and measure the output phase and amplitude. Unfortunately, the impedance of tissue is much lower than $1k\Omega$, so an AFE needs to be designed to accommodate the differences in impedances and to allow for a tetrapolar electrode configuration[100].

Analog Front End

The implementation requires conversion of a voltage from the AD5933 to a current which is fed through the tissue to a sink. Along the current path, two electrodes pick up a differential signal proportional to the tissue impedance between the two electrodes and the current passing between them. This signal needs to be further filtered and amplified before being fed back into the AD5933 for analysis.

Voltage to Current

The output voltage from the AD5933 needs to be converted to a proportional current with a maximum current consistent with the IEC6060-1 safety guidelines. A maximum value of $200\mu A$ peak was chosen to be well within the tolerances. The AD5933 is capable of generating a signal in one of four different voltages ranges. The maximum output is at $1.98V$ peak-to-peak at a $1.48V$ bias. This voltage was originally fed into a modified Holand circuit (figure 4.24) to generate the constant current[5].

---

[5] Up to version 7 of the hardware

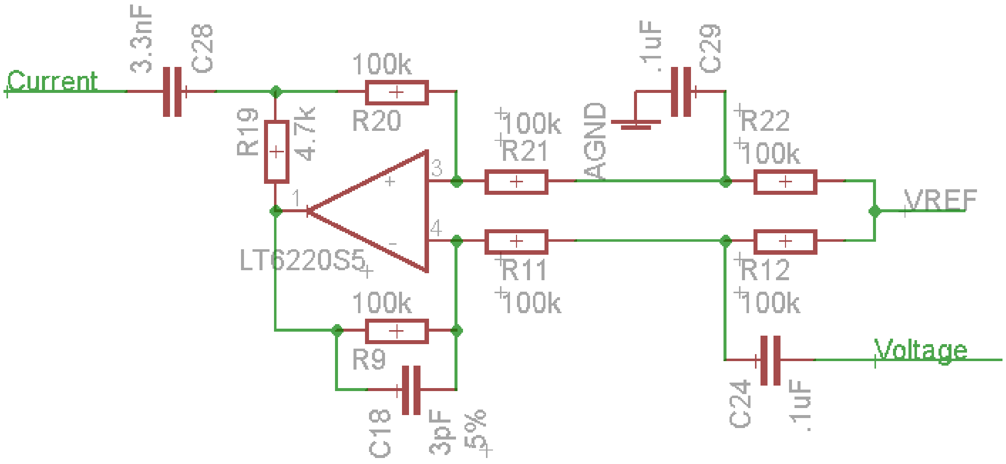

Figure 4.24: Modified Holand voltage to Current Circuit.

A later simplification of the circuit dropped the Holand circuit in favor of a simple resistor as a voltage to current converter. To set the current to $200\mu A$ from $1.98V$ peak-to-peak (or $1.98V/2 = 0.99V$ peak) requires a $0.99V/200\mu A = 4.95k\Omega$ resistor. Any additional impedance from the tissue would further reduce the current.

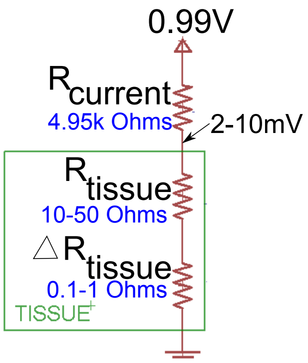

Figure 4.25: Simplified model of current path for bioimpedance measurement.

At 50kHz, the tissue impedance is quite low ($\sim 30\Omega$), and the variation due to respiration is even smaller (in the order of $0.1 - 1\Omega$[5]). The effect of the change in tissue impedance on the current becomes negligible compared to the $4.95k\Omega$ current setting resistor.. If we estimate R_{tissue}as 30Ω, we can compute the current being injected under static conditions as

$$\frac{V}{R_{resistor} + R_{tissue}} = I$$

$$\frac{0.99V}{4.95k\Omega + 30\Omega} = 198.8\mu A$$

And to model the influence of a change in the tissue resistance, ΔR_{tissue}, as a result of respiration, we can compute the change in current. Let us estimate ΔR_{tissue} as 1Ω

$$\left| \frac{V}{R_{resistor} + R_{tissue} + \Delta R_{tissue}} - I \right| = \Delta I$$

$$\left| \frac{0.99V}{4.95k\Omega + 30\Omega + 1\Omega} - 198.8\mu A \right| = 40nA$$

This variation represents a deviation of $40nA/198.8\mu A = 0.02\%$, which is sufficiently small that it can be ignored.

In addition to setting the current, the signal needs to be AC-coupled to the body. This prevents a direct galvanic connection between the electronics and the body in case of a fault in the circuitry. This also will bias the signal at the voltage of the sink. This is simply implemented by the addition of a series capacitor with a small impedance at the operating frequency of $50kHz$. A $1\mu F$ capacitor will add $\frac{1}{2\pi fc} = \frac{1}{2\pi 50kHz\, 1\mu F} = 3.1\Omega$ of resistance at 50kHz, which is negligible compared to the $4.9k\Omega$ gain setting resistor. The capacitor's impedance is frequency dependent, and for the bioimpedance spectroscopy application, it will alter the results and must be compensated for by calibrating the hardware.

Current to Voltage

The current passing through the tissue needs to be converted into a voltage suitable to be fed into the AD5933. As the current passes from the source, through the tissue, and into the sink - a distribution of voltages appear on the surface of the skin. Although this distribution is non-linear and analysis of the torso as an inhomogeneous anisotropic volume conductor is required, we can approximate the voltage will be highest at the source electrode, and decrease to zero at the sink. The differential voltage is picked up between the source and sink electrodes and fed into a differential amplifier with a target gain of 137 (derived in section 3.4.1). There are three places in the system where this can can be achieved. The differential amplifier can provide gain, the AD5933 implements a gain stage configured by an external resistor, and the AD5933 also implements a programmable 5x gain stage. The simple approach would be to set the stages accordingly to provide a total gain of 137.

The aforementioned approach is optimized for thoracic respiration. However, impedance measurements on other parts of the body might have significantly different impedance, and a fixed gain would optimize the system for one measurements site only. In order to enable a greater use of the hardware, a programmable gain differential amplifier (Analog Devices AD8557) was chosen to provide the a very large dynamic range.

The AD8557 programmable gain amplifier can be configured with a single I/O pin for a gain of between 28x-1,300x. The AD5933 is set to a gain of 2x via the external resistor, and the 5x gain stage is configurable in software. This results in a range of gains that extend from 48x to 13,000x. By working backwards, this enables us to work with maximum tissue impedances (R_{tissue}) in the range of $0.6\Omega - 171\Omega$.

Additionally, In order to fully utilize the AD5933 as a bioimpedance spectrometer, the bandwidth of the system was expanded to the range $500Hz - 200kHz$. This allows the hardware to to scan complex impedances across a range of frequencies. This was implemented with a $500Hz$ HPF followed by an Radio Frequency Interference (RFI) filter configured with a differential bandwidth of $200kHz$. The AD5933 is excellent at rejecting out of band frequencies and the RFI filter might have been unnecessary, but the the implementation of an RFI filter over an LPF required only one additional capacitor.

4.2.5 Accelerometer (Motion)

Most health monitors incorporate an Accelerometer. One can use it determine body orientation, activity levels, types of activity, and perform fall detection. Furthermore, it is very easy to implement – hence it's prevalence.

Our first implementation utilized a 3-Axis analog accelerometer that was connected to the MCU by means of three analog input lines. Although this approach worked well, it used too many ADC channels of the MCU.

We later switched to the LIS302DL manufactured by STmicroelectronics. The LIS302DL has an on-chip 8-bit ADC and provides the results digitally over an Serial Peripheral Interface (SPI) bus to the MCU, $\pm 2g/\pm 8g$ of dynamic range, and built-in hardware fall detection. This has been upgraded to the Bosch BMA150 accelerometer in the latest design. The BMA150 is similar to the LIS302DL, but it includes a 12-bit ADC, $\pm 2g/\pm 4g/\pm 8g$ of dynamic range, and has digitally configurable bandwidth filters ($15Hz - 1.5kHz$). It is only 3mm x 3mm in size and is lower in cost.

4.3 Other Components

4.3.1 Microprocessor

MCU is the core of an embedded device, and provides not only the ability to run the application, but integrates peripherals to interface with additional hardware. Our requirements for a MCU included:

- Low power consumption.
- Capability to interface with other integrated circuits through standard interfaces - Serial Peripheral Interface (SPI) and I^{2}C.
- ADC with at least 12-bits of resolution.
- DAC with at least 12-bits of resolution.
- Sufficient flash (program memory) and RAM for application to run.
- Capable of operating at 3.3 Volts .
- Hardware multiplier for filter implementations.

Although there are many microcontrollers that satisfy the above requirements, the The Texas Instrument's 16-bit MSP430 series of microcontrollers provided the best fit with its ultra-low power consumption, and easy to implement sleep states. Earlier versions of The Tricorder utilized the MSP430F169 (versions 1-2), followed by the MSP430F1611 (versions 3-6), and the MSP430F2618 (versions 7-9) (table 4.6).

4.3.1.1 Firmware

The firmware was written in C using the IAR Compiler[7]. The code has been segmented to run under different interrupt handlers, effectively creating multiple threads with different priorities. The main loop initializes the various peripherals, but otherwise sits idle waiting to write data to the SD card, and handles any incoming traffic from the Bluetooth interface. The main loop is

---

[6] Texas Instruments Peripheral Bus Interface Module

[7] `http://www.iar.com/en/Products/IAR-Embedded-Workbench/TI-MSP430/`

	MSP430F169	**MSP430F1611**	**MSP430F2618**
Frequency	8 MHz	8 MHz	16 MHz
Flash	60 Kbytes	48 Kbytes	116 Kbytes
RAM	2 Kbytes	10 Kbytes	8 Kbytes
General Purpose I/O	48	48	48
Timers	2	2	2
DAC Channels	2	2	2
DAC Resolution	12-bit	12-bit	12-bit
ADC Channels	8	8	8
ADC Resolution	12-bit	12-bit	12-bit
USART[6]	2	2	4

Table 4.6: MCU Feature Overview

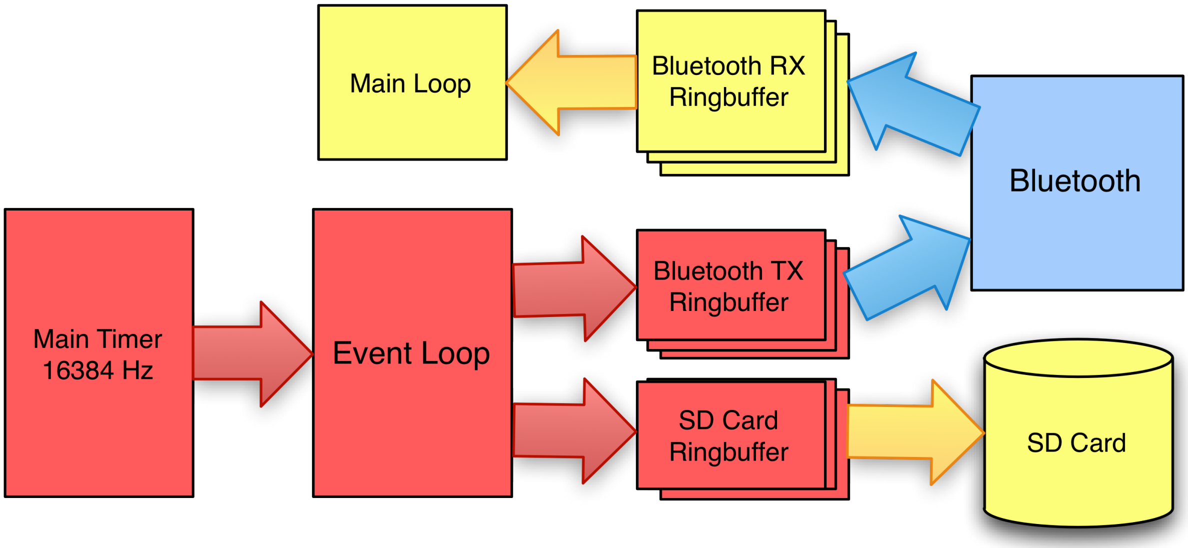

Figure 4.26: Firmware data flow. Yellow runs in the main() loop, red runs in the timer interrupt loop, and blue runs in the UART interrupt handler.

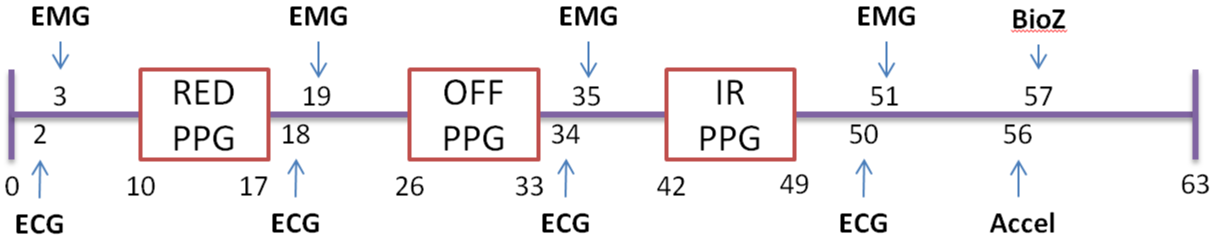

Figure 4.27: Major events occurring in the timer loop. The numbers correspond to the counter value which is incremented every $1/16384Hz = 60\mu S$. The pulse oximeter samples are taken 8 consecutive times per block.

considered the lowest priority thread, and only is active if nothing else is happening (figure 4.26, yellow).

One of the two timers in the MSP430 is clocked from an external clock crystal ($32.768kHz$), and calls the timer loop at a rate of $16.384kHz$. The timer loop performs two tasks: it increments a real time clock timer once every second to allow the *Tricorder* to keep track of time, and it performs various data acquisition and system control tasks at a regular intervals.

Each time the timer loop is called, it increments a counter from 0 to 63, then it starts over at 0. The entire loop takes $64/16384Hz = 3.9mS$, hence the periodic waveform of $3.9mS$ in figure 4.31. At various values of the counter, certain data acquisition tasks take place. The major events are outlined in figure 4.27. If a task shows up in the timing loop once, then the sampling rate is $16384Hz/64 = 256Hz$. To increase the sampling rate, additional entries can be made in the timer loop (such as for the ECG and EMG signals). The acquired data is then stored in two FIFO ringbuffers, one for data to be written to the SD card, and another to be transmitted via the Bluetooth interface (figure 4.26, red).

The main loop handles flushing the SD card buffer when at least 512 bytes are in the buffer, which is the block size for the SD card. If there is data present in the Bluetooth transmit buffer, and the hardware handshaking lines indicate that the Bluetooth IC is capable of receiving data, it is transmitted using the UART (asynchronous serial interface) interrupt handlers (figure 4.26, blue). Received data from the Bluetooth IC is also accepted by the UART interrupt handler and copied onto a received buffer for the main loop to handle.

4.3.1.2 Power Consumption

The MSP430 is one of the lowest power consuming MCUs in it's class. It's power consumption is a function of the supply voltage, the master clock speed, and the duty cycle of the processor. The MSPF430F2618 operating at 16Mhz at 3.3V uses a nominal 9.5mA of current (figure 4.28a). However, when the processor is idle, it can enter one of four different low power states to conserve energy (figure 4.28b). The power consumed will be the sum of the power at the various states.

4.3.1.3 Analog Digital Converter (ADC)

The analog digital converter on the MSP430 is implemented with an 8-channel analog multiplexer and a 12-bit successive approximation converter, and is used for the ECG, EMG, pulse oximeter,

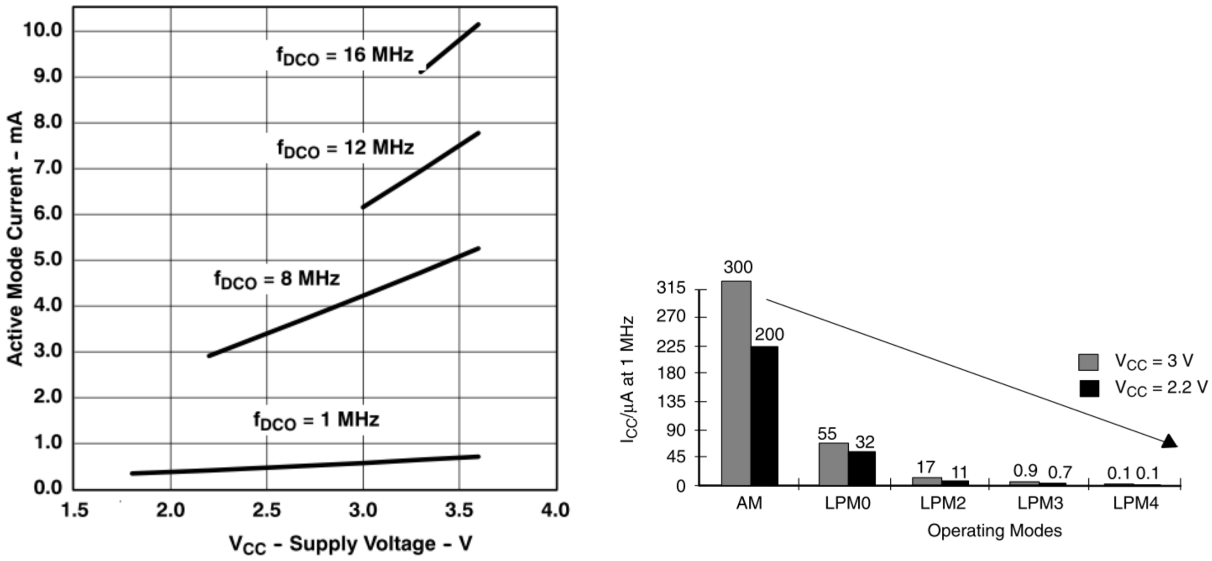

(a) Comparison at various voltages and clock speeds

(b) Comparison for active mode (AM) and the various low power modes (LPM) with a 1Mhz clock

Figure 4.28: Power consumption details for MSP430F2618

and to track the battery voltage. The converter can either the supply rails as voltage references, or an external reference. These represent the voltages that correspond to an ADC output of $2^{12} = 4096$ (max) and 0 (min). For most measurements, the supply rails were used, with both a $0.1\mu F$ and a $10\mu F$ bypass capacitor to minimize noise. This resulted in an ADC resolution of $3.3V/(2^{12})bits = 805\mu V/bit$. The external voltage reference was supplied with 1.2375V and 2.0625V, which yields a resolution of $(2.0625V - 1.2375V)/(2^{12})bits = 201\mu V/bit$. Thus, an by configuring the use of the external voltage references in software, the ADC can provide an additional gain of $805\mu V/201\mu V = 4$.

The external voltage references, as well as a mid-rail bias reference, were provided a resistive divider chain of 8 $1M\Omega$ resistors followed by unity gain amplifiers (AD8544). Additional filtering was provided before the amplifier ($\tau = 1.875\ S$) and after ($\tau = 100\ \mu S$).

Over the course of collecting data from over 100 subjects, the additional resolution of the ADC was never required, thus the external references were removed to reduce parts cost and reduce board space utilization. Instead, an AD8542 is used to generate a mid-rail reference voltage and it is also used in the PPG to provide a second stage gain.

4.3.1.4 Digital to Analog Converter

The digital to analog converter is implemented with a 12-bit R-ladder, and is used to perform offset subtraction for the pulse oximeter. It's pins are multiplexed with the 8 ADC pins, so if two channels of DAC are being used, then only 6 ADC inputs are available. It can source up to 1mA of current into a 100pF load, with a maximum slew rate of $2.7V/\mu S$ with a settling time of $1\mu S$. The DAC can use either the rail voltage or the external reference voltage, just as the ADC, in case higher resolution output is required.

Modality	Bytes/Sample	Sampling Rate	Bytes/Second
ECG	3	1024 Hz	3072
EMG	3	1024 Hz	3072
Acceleration	9	256 Hz	2304
SpO$_2$	9-18	256 Hz	2304-5608[8]
Bioimpedance	6	256 Hz	1536
Timestamp	6	1 Hz	6
Sync Block	3	1 Hz	3
		Total	**12297-15601 Bytes/Second**

Table 4.7: Bandwidth Requirements. Sync-Block only transmitted over Bluetooth.

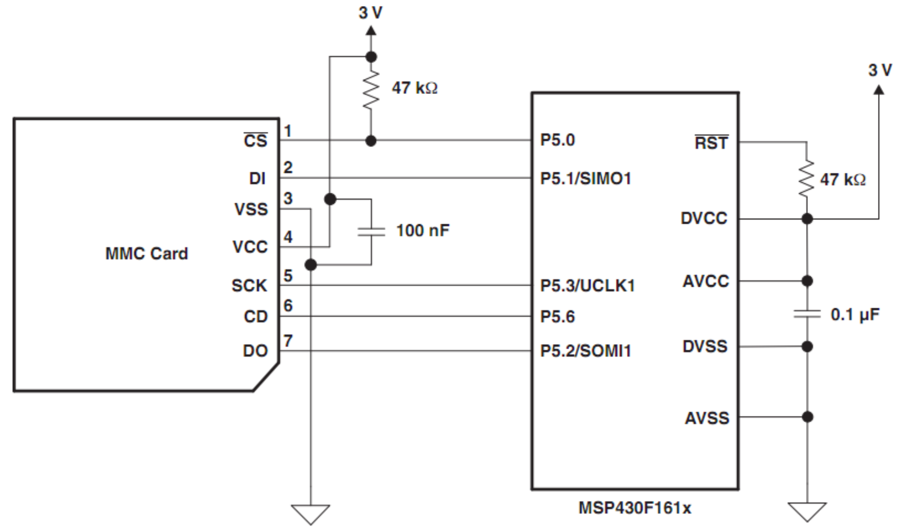

Figure 4.29: Interface between SD/MMC card and MSP430 MCU. From [112].

4.3.2 Data Storage

Our sensing modalities generate up to 15kbps of data (Table 4.7), or 1285 Megabytes of data in 24 hours. The availability of inexpensive microSD cards not only provide many gigabytes of data storage, but also allow for rapid data transfer to a personal computer by physically removing the card and connecting it to a USB reader. This process is facilitated by saving the data on a FAT filesystem, which has become the de-facto standard for removable media.

Interface

There are a number of ways to interface with the SD card, the simplest of which utilizes a 3-wire SPI bus and along with a 4th “chip select” line. An example interface is provided by texas instruments (figure 4.29), along with low level block access code [112]. The API for the code presents an initialization routine, and functions to read & write a 512-byte block from/to the SD card.

---

[8] DC offset subtraction value are only saved/transmitted when they change

Filesystem

In order to implement the FAT filesystem, the open-source DOSFS[9] library was used. It was chosen because it is designed to use minimal system resources and memory. However, the software does not appear to be maintained anymore, and several bugs were found in the code which required to be fixed (see A for patch). The library allows for the full set of typical operations such as file creation, appending to a file, reading from a file, and deleting a file.

Originally, the application created a data file if it didn't exist, and the file would be expanded as new data was written. This proved to be too inefficient as the filesystem code required multiple block reads and writes to allocate a new sector[10] , as well as multiple block reads and writes to update the directory structure with the new filesize. To circumvent this issue, a large file[11] full of the value 0x00 was pre-allocated on the filesystem by connecting the SD card to a computer via an SD/USB adapter and issuing the unix *dd* command.

```
#dd if=/dev/zero of=DATA bs=10M count=100
```

As this file was created on an empty SD card, the PC operating system would allocate the file as one large contiguous file. The dosfs code would be used to determine the location of the first segment, and hence block, of the DATA file. As data is acquired, it overwrites the empty data file by writing to sequential blocks, starting with the first block of the file. As long as the size of the data being written does not exceed the size of the file, the net effect is that the file fills with data and the overhead of the filesystem layer can be avoided.

A problem with this approach is that if the device is powered off and on, it would over-write data already in the DATA file. In order to avoid that problem, a value is written to the first 2 bytes of every 512-byte block written to the SD card. Thus, on startup, the fimware would look for the start of the file, then seek until it found the first block which had 0x0000 in the first 2 bytes (called the restart counter), and start writing at that block. The value written to the restart counter when the file is empty is 0x0001. On subsequent power cycles, it simply increments the value of the previous block (i.e. form 0x0001 to 0x0002) and all subsequent writes will written to using the value 0x0002. This strategy has the additional benefit of being able to denote the location in the data file where data acquisition began.

Data Format

As the low-level block interface writes in 512-byte blocks, the data was arranged such that the first two bytes of the 512-byte block represented a "restart counter", and the remaining 510 bytes were divided into 170 3-byte messages. The first byte of the message represented the type of data being stored, and the next two bytes contained a 16-bit payload, or the value of that type of data. For example, the sequence "0x01 0x1E 0x2C" represents a sample from the ECG of value 0x1E2C. A list of valid message types is in table 4.8.

4.3.3 Wireless Telemetry

Our requirements for the wireless telemetry include

---

[9] `http://www.larwe.com/zws/products/dosfs/index.html`

[10] The minimal unit by which data is addressed in a FAT filesystem.

[11] Typically a 1 Gigabyte file would be created which was sufficient for over 24 hours of recording

Type Code	**Description**
0	EMG
1	ECG
3	X-Acceleration
4	Y-Acceleration
5	Z-Acceleration
9	PulseOx Red AC
10	PulseOx Red DC Offset
11	PulseOx IR AC
12	PulseOx IR DC Offset
13	PulseOx Off AC
14	PulseOx Off DC Offset
19	BioZ Real
20	BioZ Imaginary
21	Battery Voltage
22	Timestamp (high 16 bytes)
23	Timestamp (low 16 bytes)

Table 4.8: Message Types

- Sufficient bandwidth to transmit all data in raw form (~ 1Mbit)
- Low power consumption
- Small form factor
- Ease of implementation
- Compatibility with target hardware (smartphones, laptops, etc).

Bluetooth was a natural choice given the requirements. The IEEE 802.15.4 based protocols (Zigbee, 6LoWPAN, etc) are limited to a theoretical maximum of 250kbit/s at the PHY, thus were too slow. IEEE 802.11 based protocols (i.e. WiFi) have high power requirements, and their implementations typically require a dedicated ARM-like processor to handle the baseband and the TCP stack which increase power consumption and complexity. Some of the key benefits of Bluetooth include

- High level of penetration in consumer devices such as cell phones and laptops.
- Standardized profiles (Serial, Audio, Object Transfer, Dial-Up Networking, etc) requiring no additional low-level protocol implementation/work.
- High-speed wireless (v1.2 Bluetooth is rated at 1Mbit/s).
- Lower power consumption per bit than competing devices. (BlueCore3 Bluetooth: 62.5nC/bit @ 720kbps; XBee ZigBee: 180nC/bit @ 250kbps; Telos Mote: 78nC/bit @ 250kbps[94])

(a) Panasonic PAN1321 Bluetooth module (b) CSR BlueCore 3 IC

Figure 4.30: Bluetooth Implementations

There are multiple ways to add Bluetooth to an embedded system. The simplest route involves the addition of a daughterboard that is populated with the required ICs, passives, RF filters, and optionally the antenna (figure 4.30a). These modules implement the firmware required[46] for a serial connection, and typically have passed FCC testing and include a license from the Bluetooth Special Interest Group, thus significantly simplifying requirements for Bluetooth implementation. As the firmware comes preloaded on the modules, implementing different Bluetooth profiles (such as OBEX file transfer) are not possible.

Another option is to add the Bluetooth ICs, passives, RF filters, and antenna manually. This option allows for the optimization of the PCB space utilized, and complete access to the firmware to implement custom applications. Cambridge Silicon Radio[12] manufactures a number of *plug'n'go* Bluetooth ICs which incorporate the baseband, firmware, and RF hardware in a single system on chip (SoC), which provide a compromise between a daughterboard module implementation and a low-level IC implementation.

Our original designs utilized the CSR BlueCore 3 IC (BC358239A; figure 4.30b) which provides audio input/output, a USB interface, 16 general-purpose I/O lines which can be used for I^2C or SPI communication, ADC, DAC and a serial interface. The firmware can be configured to provide many different profiles including Object Exchange (OBEX) to facilitate bulk data transfer, and more importantly, dial-up networking (DUN) to allow telemetry without the need for any custom phone software.

A serial connection running at 230400 baud with hardware flow control lines communicates with the MCU. The BlueCore3 IC runs firmware supplied by CSR to handle the Bluetooth Serial Port Profile (SPP) and is configured to accept all incoming connections with a default password of '1234'. Once a connection has been established, the BC3 IC signals the MCU to start transmitting data by setting it's Ready To Send (RTS) line low. An interrupt handler will recognize this high to low transition and enable the uart transmit interrupt on the MCU. The transmit uart interrupt handler will pull data from the bluetooth ringbuffer and transfer it to the BlueCore 3 IC (figure 4.26). The transmit interrupt takes a very short period of time to copy a byte of data from the ringbuffer to the tx buffer and thus runs continuously without detriment to the rest of the operation of the MCU firmware. When the ringbuffer is empty, or the RTS line goes high, the transmit

---

[12] `http://www.csr.com/`

interrupt is disabled until more data is available, or the RTS line goes low again.

The latest version of the Tricorder is deigned to work with the Panasonic PAN1321 module. This change was primarily mediated by the BC358239A IC being depreciated, and as a result, increasing in cost dramatically. The PAN1321 module is currently lower in cost as compared to the BC358239A IC[13] , not including the cost of the required passives, and the additional cost associated with assembly of a PCB with a Ball Grid Array (BGA) IC.

Wireless Streaming Protocol

In order to stream multiple biometric data sets, the various signals required serialization. The same 3-byte packet was used as detailed in the preceding data Format section. A data packet consists of 3 bytes; the first byte defines the type of data in the payload, and the next 2 bytes define a 16-bit payload. The payload types are summarized in table4.8.

One problem with streaming data in such a compact format is that if a byte is lost, then the receiver can misinterpret a payload byte as a type byte, and the type bytes can be used as part of the payload. In order to deal with this problem, a sync block is transmitted every second consisting of the following bytes: “0x55 0x55 0x55.” The receiver must watch the stream and ignore packets until it recognizes the block three “0x55 0x55 0x55” bytes. Once recognized, the subsequent byte is guaranteed to be a type byte.

In addition, if a type byte is received that is not valid (>23) then the application will assume that the stream is no long synchronized and it will wait for a sync block before continuing.

4.3.4 Power Supply

The Berkeley Tricorder is designed to operate of a Litihum-Polymer Ion (LiPo) battery. These batteries come in many different form factors, have very high energy density, minimal memory effect, and very low impedance. The nominal voltage on for a LiPo is 3.7V, with a maximum and minimum voltage of 4.2V and 3.0V. Operating the battery outside of these ranges can result in permanently damaging the battery, and a dedicated protection circuit is placed in series with the battery to prevent said damage. Battery recharge was originally performed by a dedicated charger IC (MAX1555) capable of charging at 100mA or 280mA from a mini-USB connection to a PC or dedicated charger. The latest version uses the MAX1811 with a max charge current of 500mA to reduce charge time.

A linear regulator (MAX8860, 300mA) is used to drop the battery voltage down to 3.3V, and supplies the digital portion of the circuit. An RC low pass filter ($\tau = 100\mu S$) provided filtration for the analog components and isolates the analog and digital supplies. The board has dedicated analog and digital ground planes, and shared supply planes, to help minimize noise.

The battery voltage is monitored by means of a voltage divider with the output being fed to an ADC input on the MCU.

Supply Noise

The supply noise was minimal when the SD card writes were disabled and the Bluetooth was turned off - 4mA analog & 14mA digital. The noise jumped to 8mA analog & 18mA digital when

---

[13] \$17.65 vs \$20.71 for single quantity as of December 2011

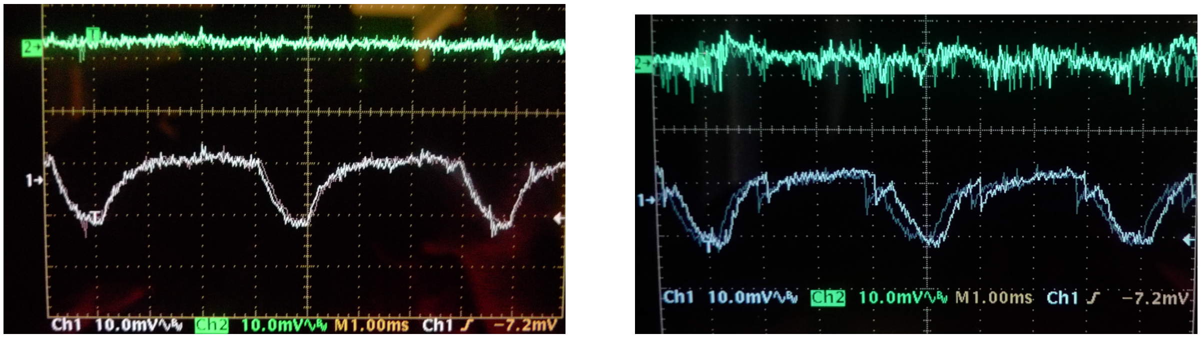

(a) Bluetooth & SD Card writes off

(b) Bluetooth & SD Card writes on

Figure 4.31: Supply noise. Channel 1 (bottom trace) is the digital supply, channel 2 (top trace) is the analog supply.

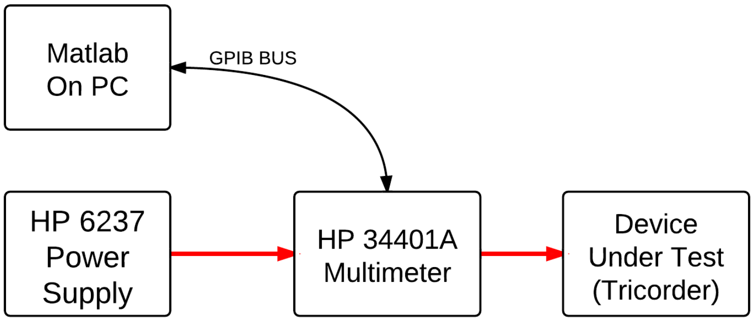

Figure 4.32: Power consumption test setup. Red arrows indicate flow of current.

the SD card writes were enabled and the Bluetooth was on and transmitting (figure 4.31). A large period component to the digital noise is present, and corresponds to the 3.9mS data acquisition loop in which LEDs are cycled on/off and other measurements take place.

Power Consumption

A good deal of effort was spent minimizing the current consumption of the device. The lower the power consumption, the longer the device can operate without a recharge. Most of components were chosen to optimize this parameter, however, several required components were unavailable in low power versions. Current measurements were made by connecting an HP 34401A multimeter in series between the power supply and *The Berkeley Tricorder* (figure 4.32). The multimeter was configured to measure current and the results were sent to a Matlab for analysis. The results are displayed in figure 4.33 and the various component consumption has been summarized in table 4.9.

Based on this data, we can anticipate an ambulatory implementation which stores data and has no telemetry to use 95mA of current, and one with telemetry and no storage to use 78mA of current. A 1000mAh battery will last 10.5 and 12.8 hours, respectively.

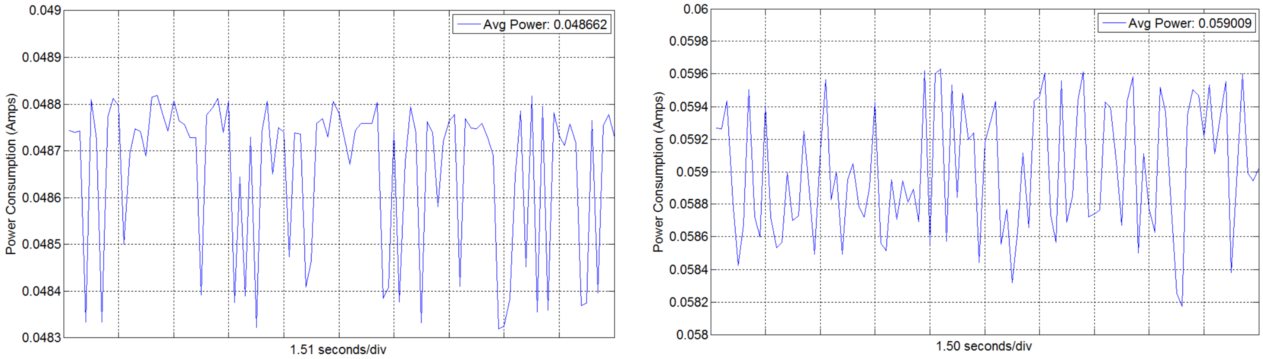

(a) Sampling everything except PPG

(b) Sampling everything

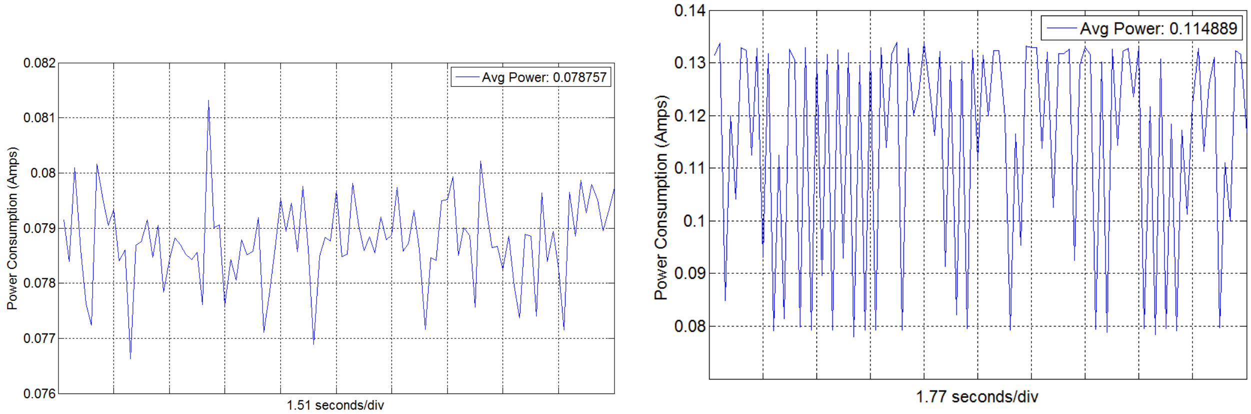

(c) Sampling everything & Bluetooth streaming

(d) Sampling everything, Bluetooth streaming & SD card writes

Figure 4.33: Power consumption under different modes of operation.

Component	Current (mA)
Base System (No PPG)	48
PPG	11
Bluetooth	19
SD Card Writes	36
Total	114

Table 4.9: Summary of power consumption for various components.

4.4 The Harness and Electrodes

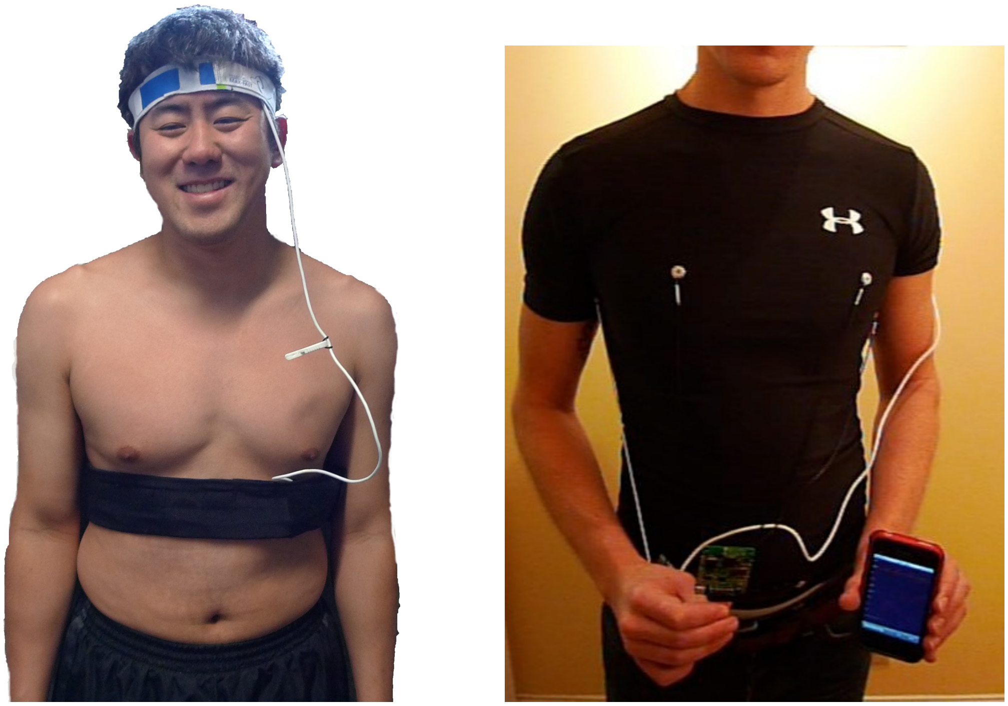

(a) Chest strap and reflective forehead PPG. (b) Compression shirt with conductive fabric.

Figure 4.34: Subjects wearing the monitor

The harness (Figure 4.34a) was initially prototyped in house and then replicated in a small, medium, and large sizes through a local manufacturing company. The harness is made of fabric that is designed to only stretch lengthwise. It has been sewn into a tube, and Velcro attached at either end allows the strap to be wrapped around the subject's torso and fastened.

The Berkeley Tricorder device, a Lithium-Polymer Ion battery, and a wiring harness were placed inside the strap through an opening that can be Velcroed shut. The electrode leads run through the inside of the strap, exit through button holes placed at regular intervals, and connect to the electrodes (Figure 4.35).

The electrodes are manufactured by Respironics (Model 16510-1, Murrysville, PA), and consist of conductive rubber, an affixed Velcro backing, and a slot for the electrode to attach. The electrodes have no adhesive or gel, and are held in place by the harness. The electrodes attach to small squares of Velcro on the inside of the harness.

In addition to the strap, an Armor All compression shirt had three 1"x.5" strips of conductive fabric affixed to the inside using iron-on tape. The locations corresponded to the typical ECG electrode placements (figure 4.34b). Electric contact was made to the conductive fabric by means of a metal button affixed to the shirt. No accommodations were made for the sensing hardware which was held by the subject for the duration of the data collection episode.

Finally, *The Berkeley Tricorder* was affixed to a subject using disposable Ag-AgCl electrodes (figure 4.36).

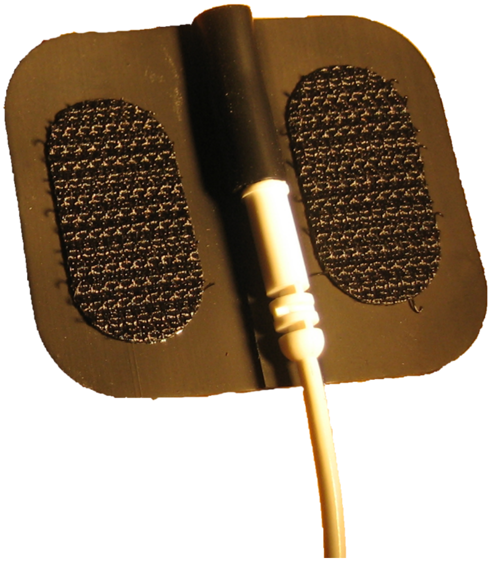

Figure 4.35: Non-Adhesive electrode with Velcro backing

4.5 The Applications

Numerous applications have been written to visual the data streaming over Bluetooth from *The Berkeley Tricorder*.

The fist application written was written in C# to connect to the device via Bluetooth and display real time data. Between 12297 and 15601 bytes/second (Table 4.7) are required to stream all the channels. The C# application has was subsequently ported to a pocketPC mobile phone (figure 4.37a).

A java application was subsequently written in the Processing[14] environment. This application ran on Windows, Macintosh, and Linux machines.

Additionally, an iOS application was written for the iPhone and iPad, as well as an Android application. In order to communicate with the iPhone/iPad over Bluetooth requires the use of a dedicated encryption chip and a proprietary stack from Apple. The use of an encryption scheme greatly reduces the maximum Bluetooth throughput below the required 12297 bytes/second minimum.

In order to stream data to the iPhone/iPad, the device was first jailbroken to allow for root access to the hardware. An open-source Bluetooth stack called btstack[15] was available with implementation of all layers up to the HCI layer. The author of btstack was collaborated with to finish development of the RFCOMM layer to enable serial streaming. In addition to the Bluetooth stack, custom graphing libraries were written to enable streaming of the biometric data (figure 4.37b).

---

[14] `http://processing.org/`

[15] `http://code.google.com/p/btstack/`

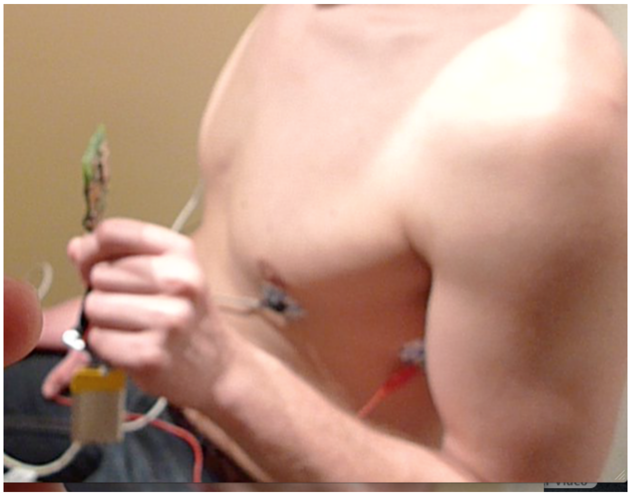

Figure 4.36: Disposable Ag-AgCl adhesive electrodes affixed to subject.

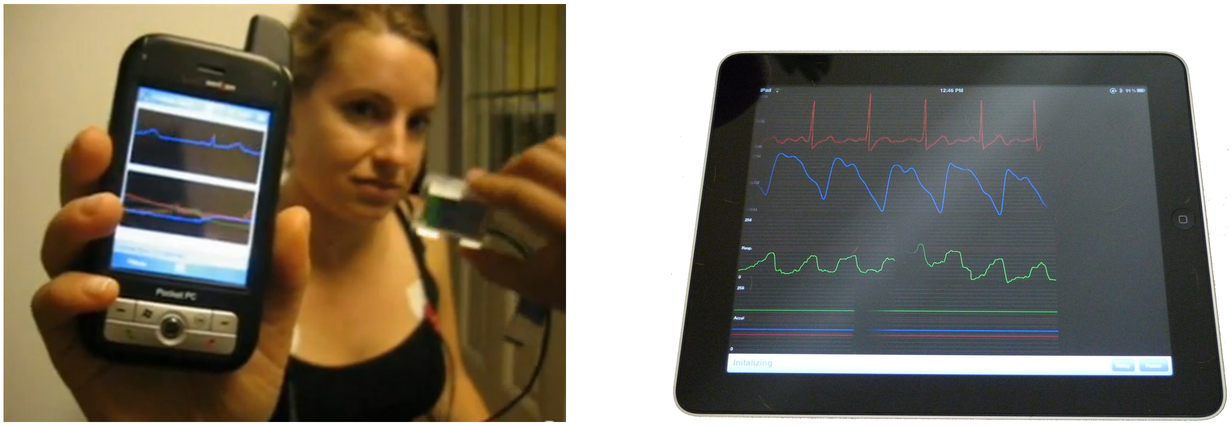

(a) PocketPC

(b) iPad (1st Generation)

Figure 4.37: Visualization applications for data from *The Berkeley Tricorder.*

4.6 Version History

The Berkeley Tricorder has undergone a number of versions in order to optimize the features, improve power consumption and reduce board space. A summary of the different major versions and the associated features is presented in figure 4.38.

The initial version used individual connectors per sensor which were found to be difficult to use, as was dropped by version four in favor of a unified connector for all the signals. Although the unified connector was designed with a friction locking mechanism, the cable was easily pulled out and required tape being applied to prevent it from pulling out during ambulatory use. Version 8 implemented a smaller connector with a stronger locking mechanism, but the connector required hand-soldering of all the signal cables in a tight space and was very difficult to use. Version 9 switched to a very robust molex connector with a strong locking mechanism. However, the signal density of this connector is very low and thus the miscellaneous I/O pins which were previously exposed were removed.

The processor has been upgraded several times as well. The MSP430F169 was used in the first 2 versions, followed by the MSP430F1611 in the next 4 versions, and the MSP430F2618 in the last 3 versions (table 4.6). The main advantage to the upgraded processors is the ability to operate at higher clock speeds as well as additional RAM.

The Bluetooth module initially used in the first 2 versions was from the BlueCore2 family by CSR. The following 6 versions utilized the BlueCore3 module, and the latest version moved away from a Bluetooth IC to an module. Besides cost considerations, the module is certified by the Bluetooth SIG and the FCC, thus removing the need for FCC testing and Bluetooth certification, both very costly.

Version 8 was designed to explore the ability to stream biometric signals over a cellular modem and included an EES3 module from Cinterion. The data was sent over a TCP socket to a client written in Perl, and subsequently put into a database. The limited and unreliable bandwidth necessitated the development of on-board feature extraction routines and only the extracted features, such as heart rate, were transmitted.

The first four versions incorporated an audio amplifier with the goal of analyzing breathing sounds. A vacuum mold of a stethoscope was made and an soft silicone copy of the stethoscope was made. An electret microphone was placed inside the silicone stethoscope resulting in excellent audio reproduction quality. However, this feature was removed in subsequent versions as privacy concerns with recorded audio arose.

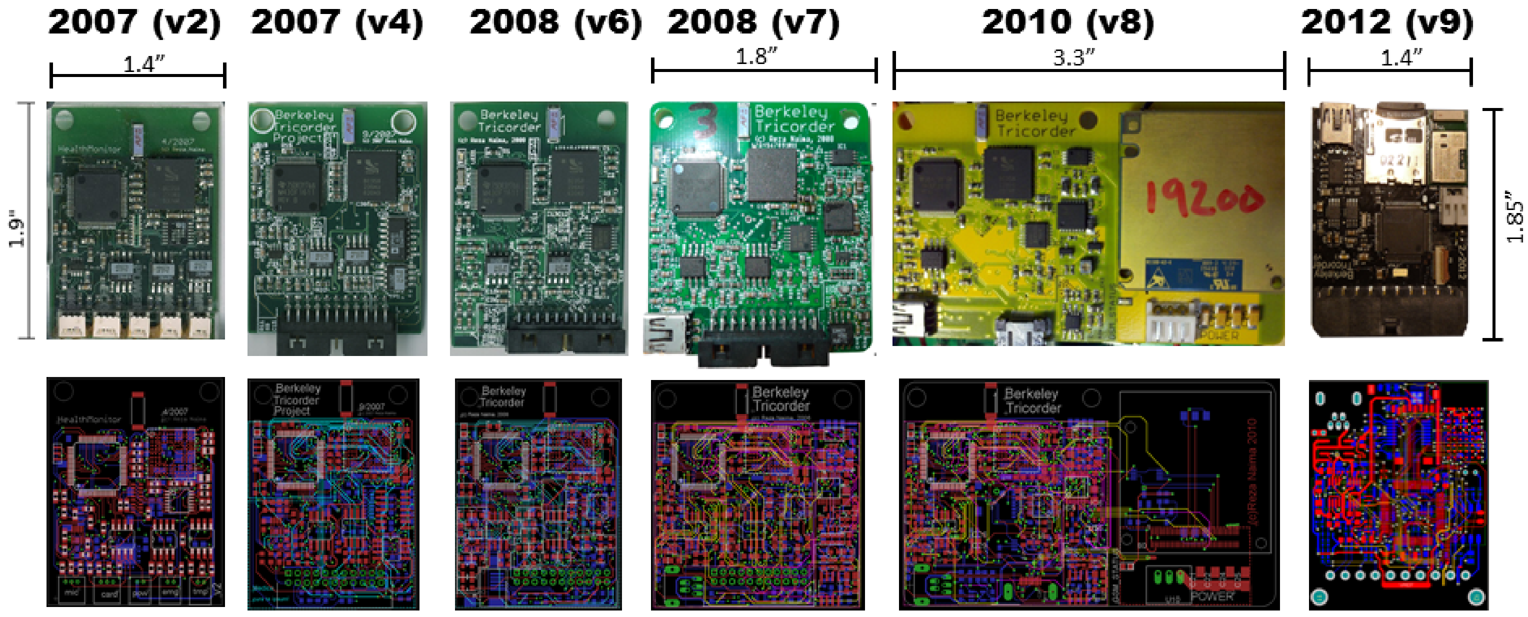

Audio Recording	Audio Recording				
EMG	EMG	EMG	EMG		**High Speed EMG**
ECG	ECG	ECG	ECG	ECG	ECG
Misc Amplified Input	Misc Amplified Input	**Misc Inputs/Outputs**	Misc Inputs/Outputs	Misc Inputs/Outputs	
Analog Accelerometer	Analog Accelerometer	**Digital Accelerometer**	Digital Accelerometer	Digital Accelerometer	**12-bit Digital Accelerometer**
SD Card	SD Card	SD Card	SD Card	SD Card	SD Card
BlueCore2 BT	BlueCore3 BT	BlueCore3 BT	BlueCore3 BT	BlueCore3 BT	**PAN 1321 BT Module**
	Batt Charger	Batt Charger	Batt Charger	Batt Charger	**High Current Batt Charger**
	USB Interface	USB Interface	USB Interface	USB Interface	**USB Recharge Only**
	PulseOx V1	**PulseOx V2**	**PulseOx V3**	**PulseOx V4**	**PulseOx V4**
			BioImpedance Spectrometer v1	**BioImpedance Spectrometer v2**	**BioImpedance Spectrometer v2**
				GSM Cell Data Module	

Figure 4.38: Revisions of the Tricorder and major features.

Chapter 5

Device Validation

5.1 Analysis

The various features and signals from *The Berkeley Tricorder* have been been evaluated and compared to the theoretically expected results, as per the design. Additionally, a commercial Electrocardiogram (ECG) and Photoplethysmograph (PPG) were purchased and signals from the commercial systems were compared to those from *The Berkeley Tricorder*.

5.1.1 Electrocardiogram (ECG)

Front-End Gain

A Wavetek 228 function generator was set to output 1mV and connected to a 1:100 voltage divider to generate a $10\mu V$ signal. The $10\mu V$ signal was then sent to the input of the ECG circuit as well as to the a Tektronix TDS784D oscilloscope. The output of the ECG amplifier was also sent to the oscilloscope. Both the function generator and oscilloscope were controlled over a IEE-488 General Purpose Interface Bus (GPIB) parallel bus by an application written in Matlab. The application sweeps through a range of frequencies, and compute the gain as the ratio of the signal from the test circuit to that from the voltage divider (figure 5.1).

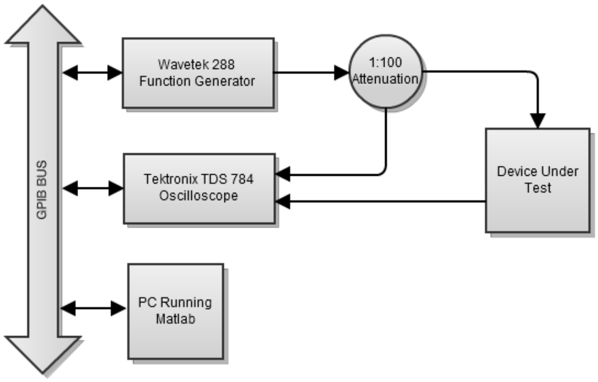

Figure 5.1: Test setup for measuring gain.

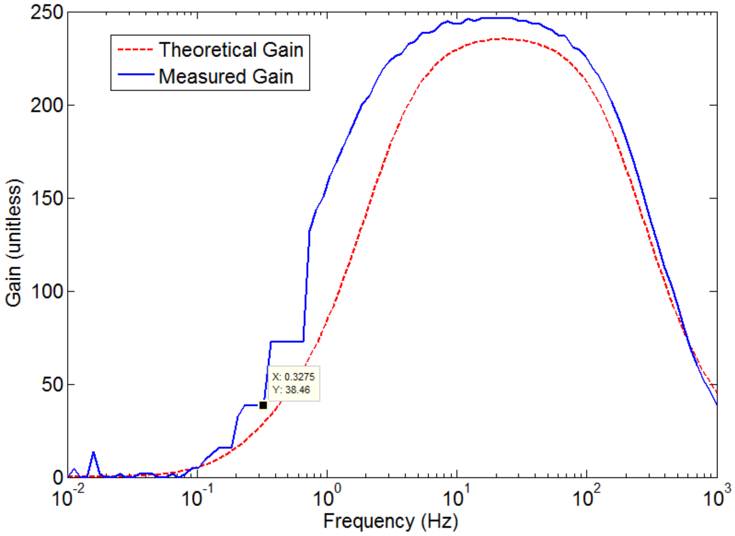

Figure 5.2: ECG gain comparing expected and actual values.

The gain of the filter and amplifier were measured and compared to values generated from a spice simulation of the circuit (figure 5.2) and demonstrated good agreement. The measured bandwidth is $0.6Hz - 200Hz$ which is very close to our target of $0.5Hz - 150Hz$. The deviation from the expected results are most likely due to errors in the passive component values, including the gain setting resistor.

Motion Artifacts

The ECG implementation was evaluated in a number of studies and trials. The initial trial was a subjective evaluation of the ability of the hardware to operate under ambulatory conditions. The plot in figure 5.3 is from a test subject in the first set of human trials; the data plotted is from the accelerometer and the ECG. The ECG provided clean R-wave peaks, even under heavy motion.

Comparison With FDA Approved ECG

ECG data was collected simultaneously using the same set of electrodes by *The Berkeley Tricorder* and a commercial FDA-approved ECG (MD100A12 from Beijing Choice Electronic Tech. Co.). The output of the FDA approved device was saved to a PC and the file format was reverse engineered in order to extract the ECG waveform.

A sample of the ECG recording from both devices is plotted in figure 5.4. The plots on the left are from placing the electrodes close to each other on the same arm. Thus, all the noise is picked up but none of the signal from the heart. The plots on the right are generated by putting the electrodes on either side of the heart, and consist of both the noise and signal components. The Power Spectral Density (PSD) of the ECG signals are plotted in figure 5.5. The plots from *The Berkeley Tricorder* were filtered for 60Hz line noise using a 10^{th} order Butterworth stopband filter.

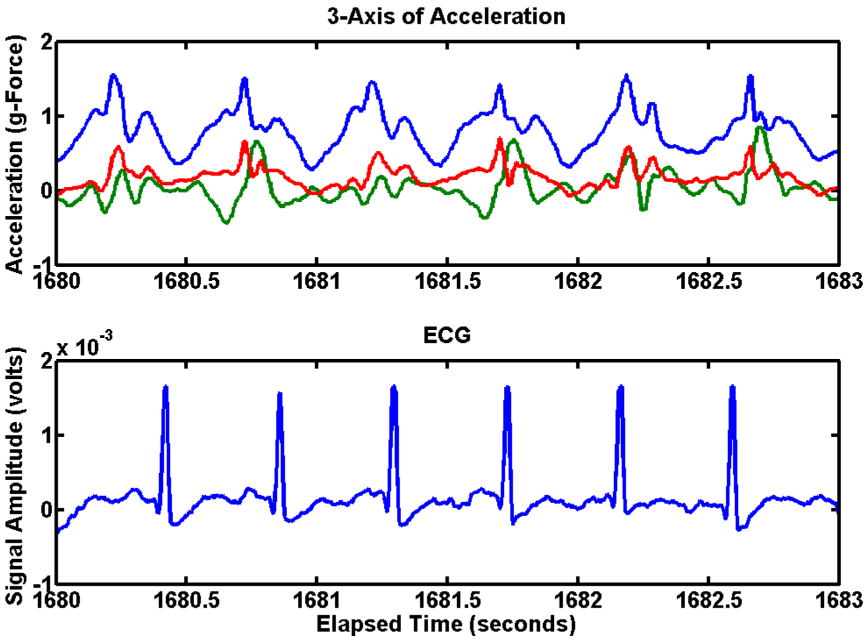

Figure 5.3: ECG signal (lower plot) captured while subject in motion (upper plot)

The red portion of the plot is the PSD of the noise component, and the blue portion of the plot is the PSD of the ECG signal plus the background noise. The power of the signal can be calculated by subtracting the area of the red plot from the blue plot.

$$Area_{signal=}Area_{signal+noise} - Area_{noise} = Area_{blue} - Area_{red} \tag{5.1}$$

The ratio of the signal to noise defines the Signal to Noise Ratio (SNR).

$$SNR = \frac{Area_{signal}}{Area_{noise}} = \frac{Area_{blue} - Area_{red}}{Area_{red}} \tag{5.2}$$

The SNR is calculated as 28.2 and 86 from *The Berkeley Tricorder* and the commercial device, respectively. Both signals were also filtered with a 2^{nd}order Butterworth Low-Pass Filter (LPF) with a corner frequency of 40Hz. This changed the SNRs to 67.1 and 71.2, respectively.

The device is stated to sample the data at 250Hz, however, the accuracy of the devices internal clock is unknown as compared to *The Berkeley Tricorder*[1]. Through trial-and-error, it was determined that the data was sampled at $248.01Hz$. The data from the commercial device was resampled, scaled, and shifted to be overlaid on the data from *The Berkeley Tricorder* (figure 5.6).

5.1.2 Electromyogram (EMG)

Front-End Gain

A different test setup was used to quantify the gain/bandwidth of the ECG system to incorporate the effects of digitization on the signal. A Wavetek 228 function generator was set to output $6mV$ peak to peak and connected *The Berkeley Tricorder's* Electromyogram (EMG) input. The signal

---

[1] *The Berkeley Tricorder* uses a $32768Hz \pm 20ppm$ oscillator for sample acquisition.

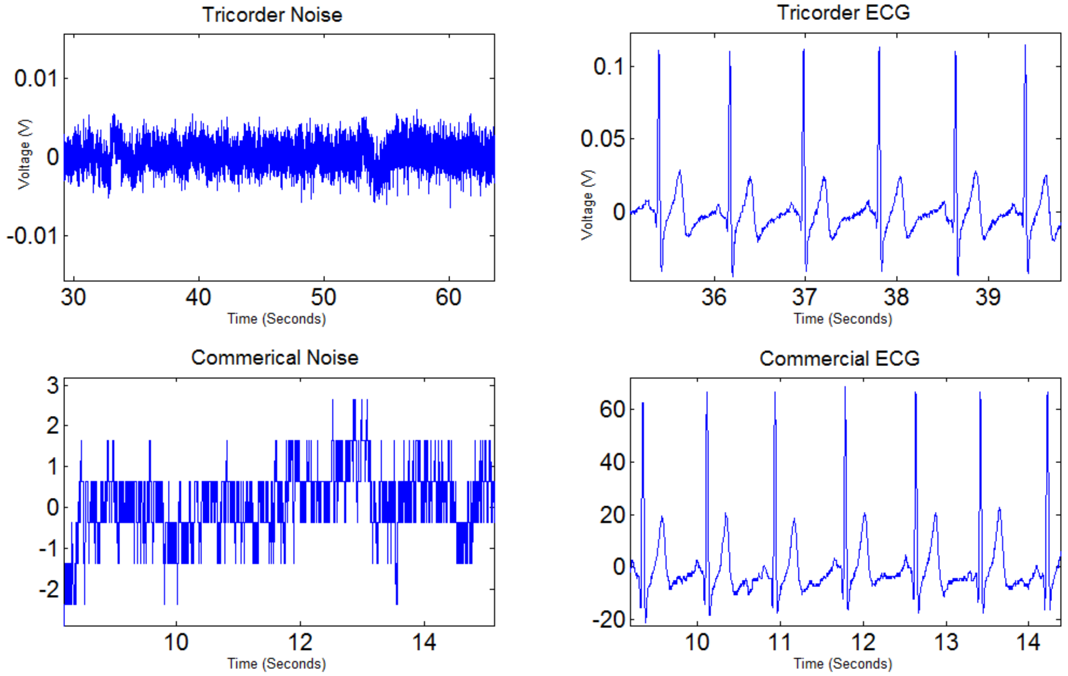

Figure 5.4: Sample ECG signal and noise signal from Tricorder and commercial ECG. Noise is generated by putting both electrodes on same arm. 60Hz notch filter applied to the signal from the Tricorder.

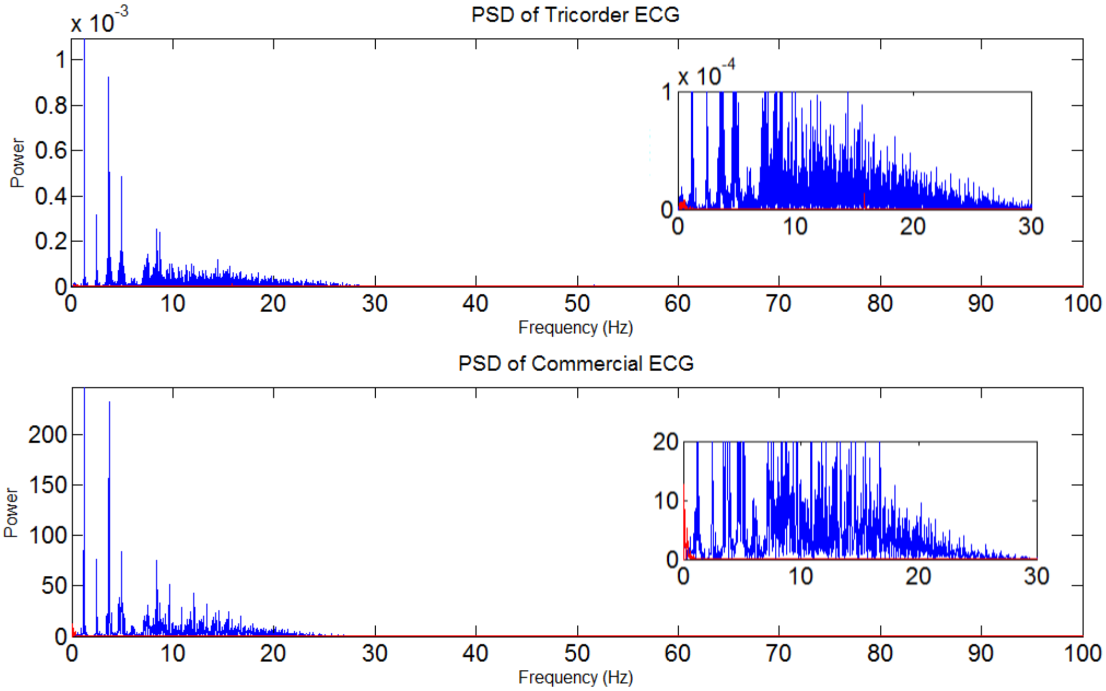

Figure 5.5: ECG power spectrum of the Tricorder and a commercial ECG. The inset represents is a close up of the same data. A 60Hz notch filtered was applied to the signal from the Tricorder.

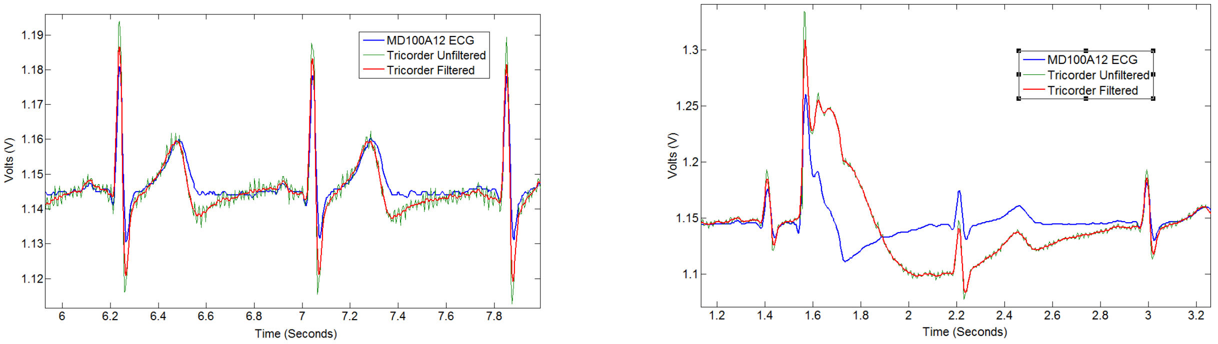

(a) Normal ECG Rhythm

(b) ECG signal with intentional artifact introduction

Figure 5.6: ECG output from *The Berkeley Tricorder* compared to commercial ECG

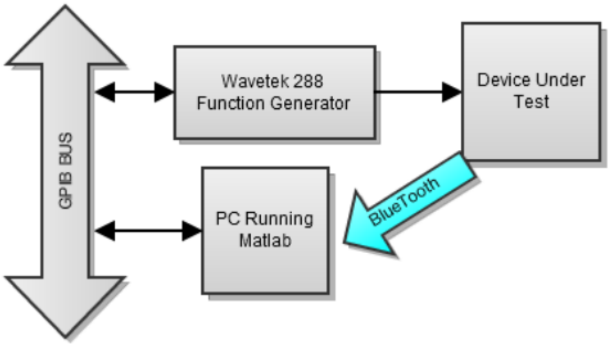

Figure 5.7: Test setup for measuring gain.

passed through the Analog Front End (AFE) and to the Analog to Digital Converter (ADC) of the Microcontroller (MCU). The results were sampled at $1024Hz$ and sent over Bluetooth back to the Personal Computer (PC) for analysis. A Matlab script was used to adjust the frequency generated by the function generator, and the amplitude of the signal was measured from the wireless signal (figure 5.7).

The gain of the filter and amplifier were measured and compared to theoretical values (figure 5.8) and demonstrated good agreement. There appears to be a shift of the High-Pass Filter (HPF) corner frequency down a few Hz, and is most likely a result of inexact passive component values.

Sample Data

The EMG circuit was connected to two electrodes spaced 20mm apart on the left quadriceps. Multiple contractions were recorded, a 60 Hz notch filter[2] was applied, and the raw data and power spectrum were plotted (figure 5.9). A three second segment of no contraction and a three second with muscle contraction were isolated and the PSD derived from both. The SNR was computed as 25.37 using the same method as used to compute the ECG SNR using equation 5.4. The PSD during a period of no contraction was used to estimate the noise, and the PSD during a period of contraction was used to estimate a combination of signal and noise.

---

[2] A 10^{th} order Butterworth stopband filter between 59Hz and 61Hz.

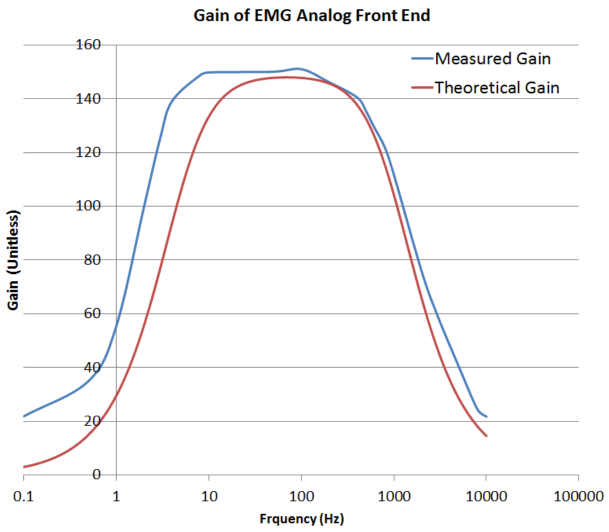

Figure 5.8: EMG gain comparing expected and actual values.

5.1.3 Pulse Oximeter (Photoplethysmograph (PPG))

A transmissive finger clip sensor was connected to *The Berkeley Tricorder* and PPG samples were acquired over Bluetooth. A sample of the data is plotted in figure 5.10, showing a very clean signal with no filtering applied.

A commercial FDA-approved pulse oximeter (CMS60C by Contec Medical Systems Co., LTD) was purchased and used in conjunction with *The Berkeley Tricorder* to acquire the PPG from two adjacent fingers simultaneously. The commercial devices can stream live data to a PC application, but does not allow for the stream to be saved. A port sniffer was used to intercept the serial data and the protocol was reverse engineered. By comparing the duration between peaks from the signal from the devices, it was determined that the commercial device uses a sampling rate of $60Hz$. A Perl script was used to reconstruct the raw waveforms from the serial data.

A power spectrum from the signals captured from *The Berkeley Tricorder* and the commercial pulse oximeter were plotted (figure 5.11). A comparison of the power spectrums reveals a strong peak corresponding to the heart rate along with multiple harmonics from both devices. The amplitude of the 3^{rd} harmonic onward is much lower for the commercial device as compared to that of *The Berkeley Tricorder* which indicates a more aggressive LPF was used. Additionally, by looking at the amplitude of the PSD between the initial harmonics, it is apparent that there is more noise in the signal from the commercial device than from *The Berkeley Tricorder.*

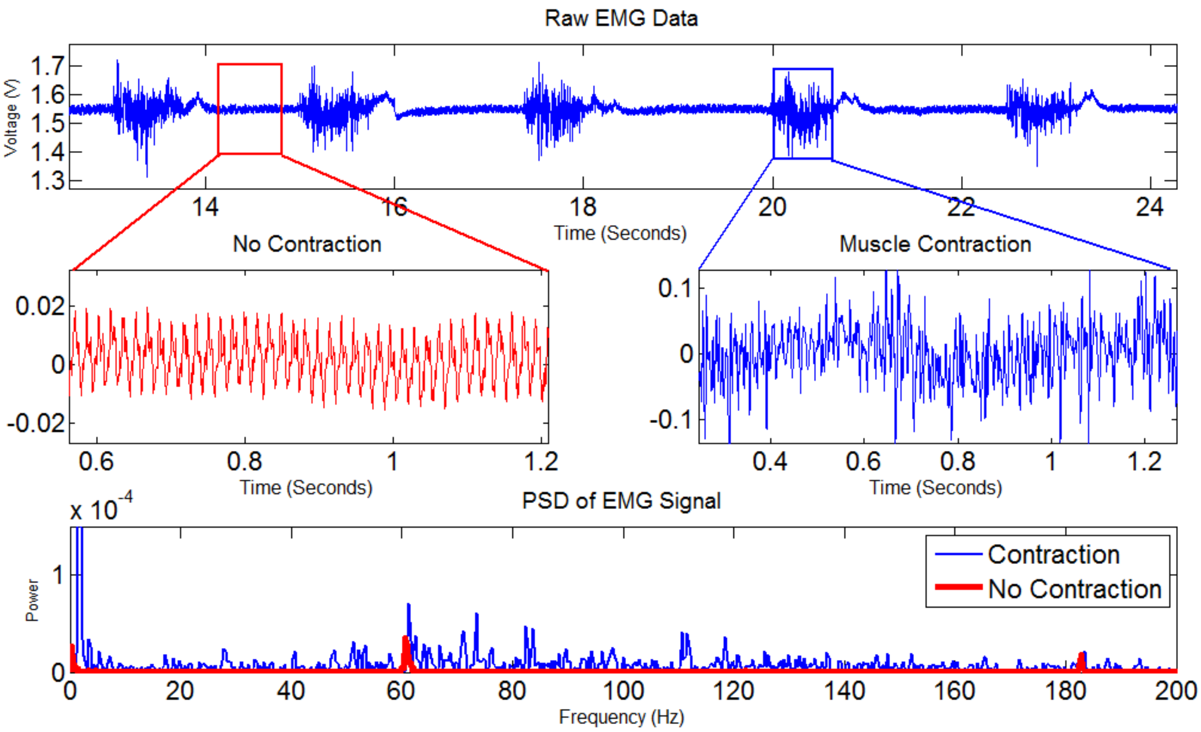

Figure 5.9: Example of EMG signal from quadriceps. Data was filtered with 60Hz notch filter.

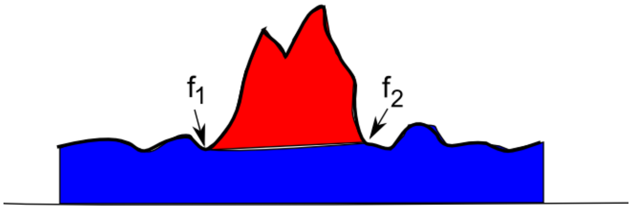

Figure 5.12: Fictitious data plotted. The area used to compute SNR is in red, the area in blue is considered noise.

The PPG is a periodic signal which contains a strong pulse component above the noise floor in the PSD. Additionally, multiple harmonics of the pulse can be found at regular intervals in the PSD (figure 5.11). The SNR of this signal is computed as the ratio of the the area of the signal above the noise floor to the area of the noise floor.

For example, in figure 5.12, the area in red represents a single harmonic of the signal and the area in blue represents the noise. For each harmonic peak, the signal area, $Area_{signal,peak}$, is calculated as

$$Area_{signal,peak} = \sum_{N=f_1}^{f_2} psd(N) - \frac{(psd(f_1) + psd(f_2))}{2} n \tag{5.3}$$

And the sum of all $Area_{signal,peak}$ is equal to the power of the signal.

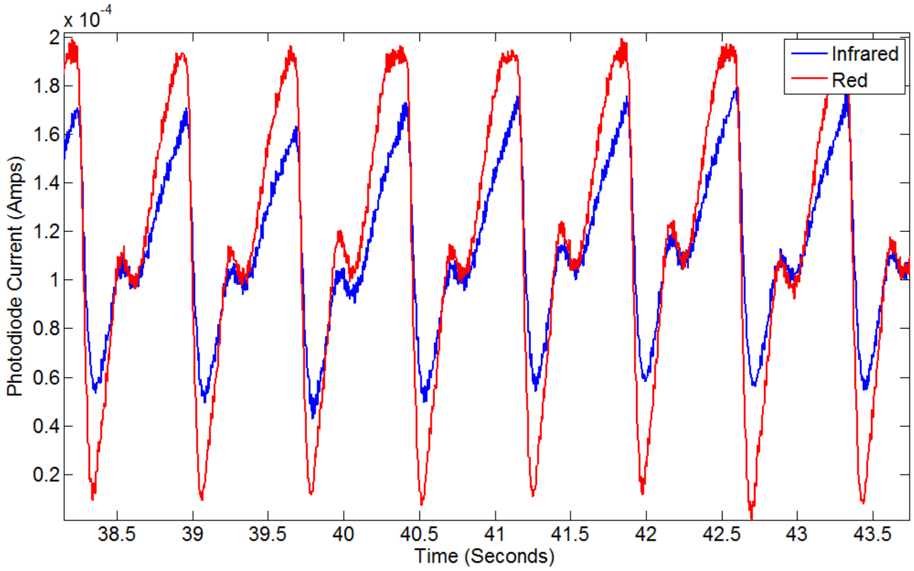

Figure 5.10: Sample data from PPG.

$$Power_{signal} = \sum Area_{signal,peak}$$

The power of the noise is then equal to all the area of the plot minus the area of the plot corresponding to the signal.

$$Power_{noise} = Area_{all} - \sum Area_{signal,peak}$$

The SNR of then calculated as

$$SNR = \frac{Power_{signal}}{Power_{noise}} = \frac{\sum Area_{signal,peak}}{Area_{all} - \sum Area_{signal,peak}} \tag{5.4}$$

The SNR of the red and infrared signals from *The Berkeley Tricorder* were computed as 9.79 and 3.78, respectively. The application of a 4^{th}order Butterworth LPF with a corner frequency of $4Hz$ resulted an increase in the SNR to 15.6 and 4.27, respectively. The commercial device was computed as having an SNR of 2.56 unfiltered and 2.54 filtered. From the figures, it is apparent that the bulk of the noise is low frequency. Modifying the filter to act as a bandpass filter between 1Hz and 4Hz increased the red and infrared SNR to 21.4 and 18, respectively. The SNR of the commercial device also increased to 7.77.

5.1.4 Respiration (Bioimpedance (BioZ))

Resistance Measurement

The AD5933 impedance spectrometer Integrated Circuit (IC) greatly simplifies the implementation of the BioZ. A test circuit consisting of two 50Ω resistors with a trimming potentiometer in series (figure 5.13b) was configured to mimic interaction with tissue (figure 3.17). The test circuit was connected to an HP 34401A 6-digit multimeter as well as the BioZ connection on *The Berkeley*

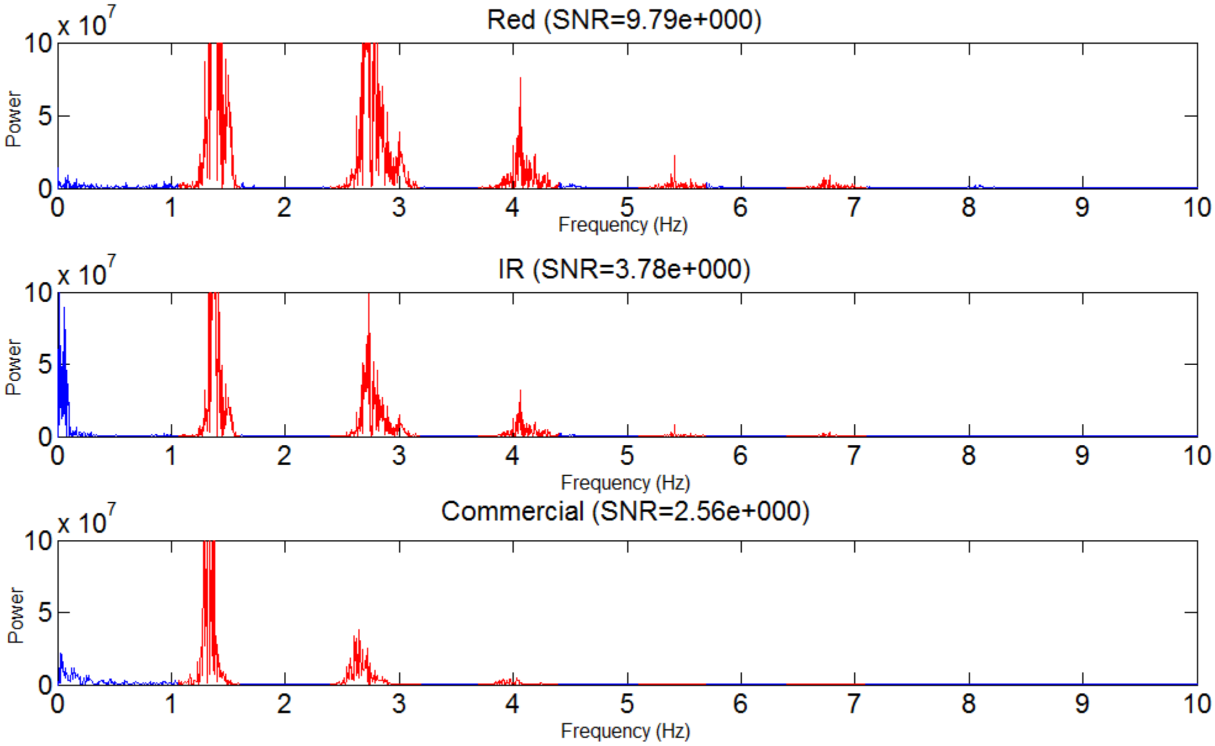

Figure 5.11: Sample power spectrum from Tricorder and commercial pulse oximeter. Top two plots are from the Tricorder, bottom plot from CMS60C. The red represents the signal and harmonics used to compute SNR, blue is noise.

Tricorder. Data was logged via Bluetooth from the Tricorder, and via GPIB from the multimeter to matlab. The trimmer potentiometer was adjusted with a screwdriver and turned clockwise and counterclockwise three times to generate a change in resistance. The output of the AD5933 is an unscaled number which was subsequently scaled to match the data (figure 5.14a).

The stepwise change in resistance is a function of the mechanical action of the potentiometer. The signal contains 0.068Ω of RMS noise, predominantly in the high frequency range. However, the application of an Gaussian FIR filter with a mean of 0, a standard deviation of 2 smaples, and width of 8 samples reduced noise down to 0.0064Ω RMS while still being very responsive to changes in the impedance of the system (figure 5.14b).

Comparison of results with spirometer

A peak flow meter (Microlife PF 100) was purchased to compare expired air flow to respiration data collected from *The Berkeley Tricorder.* The peak flow meter only records the maximum air flow velocity, not the air flow profile. It works by measuring the rotational velocity of a small propeller that is in the device using an optical encoder. The encoder's output is further filtered and rectified through a Bipolar Junction Transistor (BJT). The signal from the BJT was sampled using a USB-based logic analyzer (Logic by Saleae) and exported into a text file which was then imported into Matlab for further analysis.

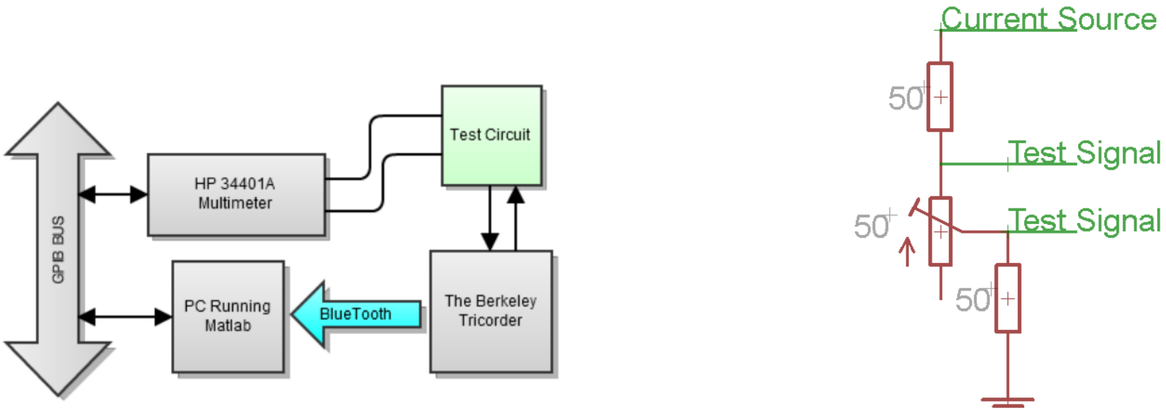

(a) The test circuit is connected to the BioZ interface on *The Berkeley Tricorder* as well as to a multimeter. The multimeter and *Tricorder* both log their data to a PC.

(b) Test Circuit consisting of two resistors and a triming potentiometer.

Figure 5.13: BioZ test setup

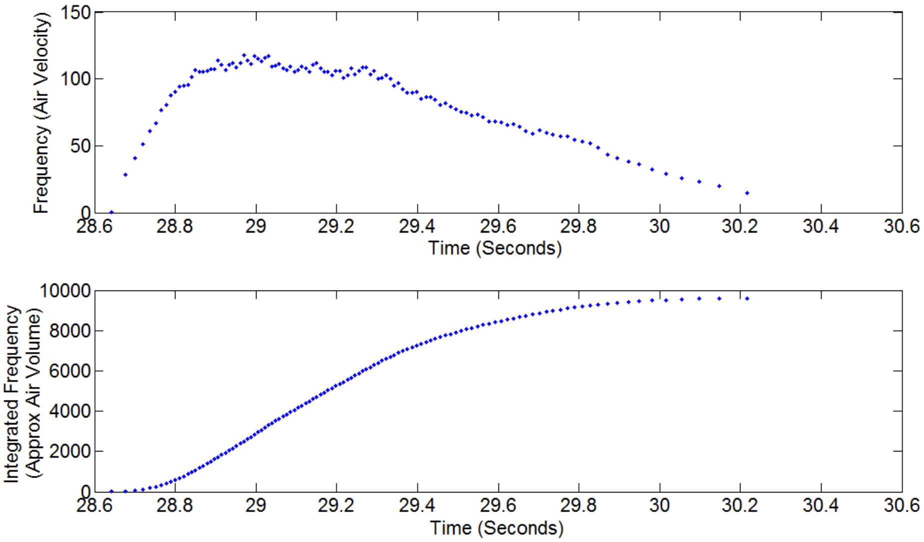

Figure 5.15: Air flow velocity and volume from modified peak flow meter.

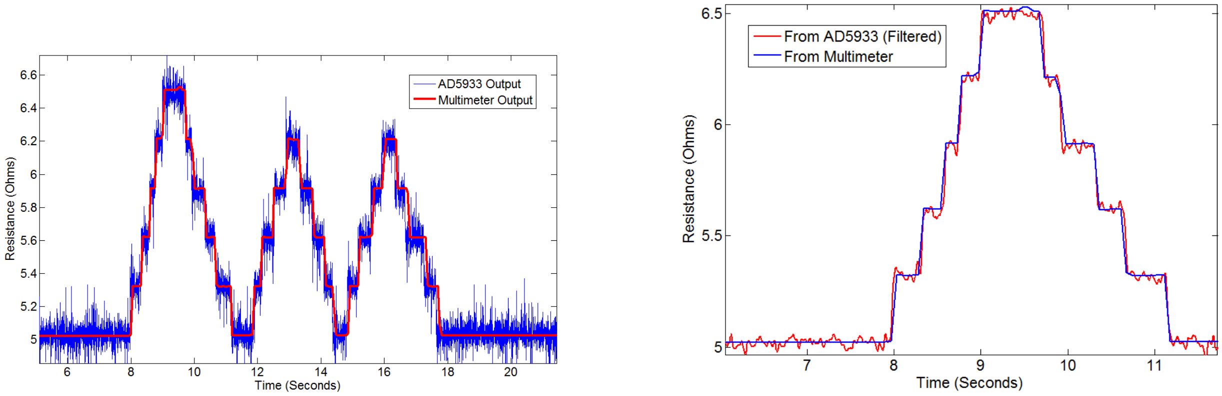

(a) Resistance change and output from AD5933.

(b) Gaussian filter applied to the output of figure 5.14a.

Figure 5.14: Raw and filtered output of the AD5933.

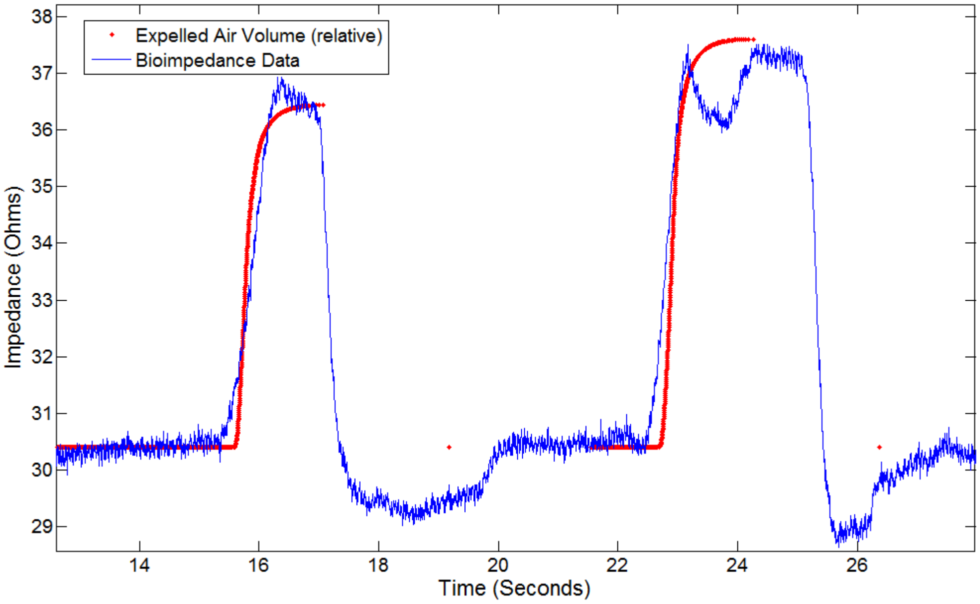

Figure 5.16: Expiration volume from peak flow meter (red) and change in thoracic impedance.

The duration between pulses from the optical encoder are inversely proportional to air flow velocity. A Matlab script was used to generate the air flow velocity, and integrated to generate the air volume expired (figure 5.15). Data was simultaneously collected from the the BioZ sensor in *The Berkeley Tricorder* and overlaid with data from the commercial device (figure 5.16). Perfect agreement between the signals is not expected as there is no linear relationship between deformation of the chest and air flow, however, there is a good deal over similarity between the signals.

Paced Respiration

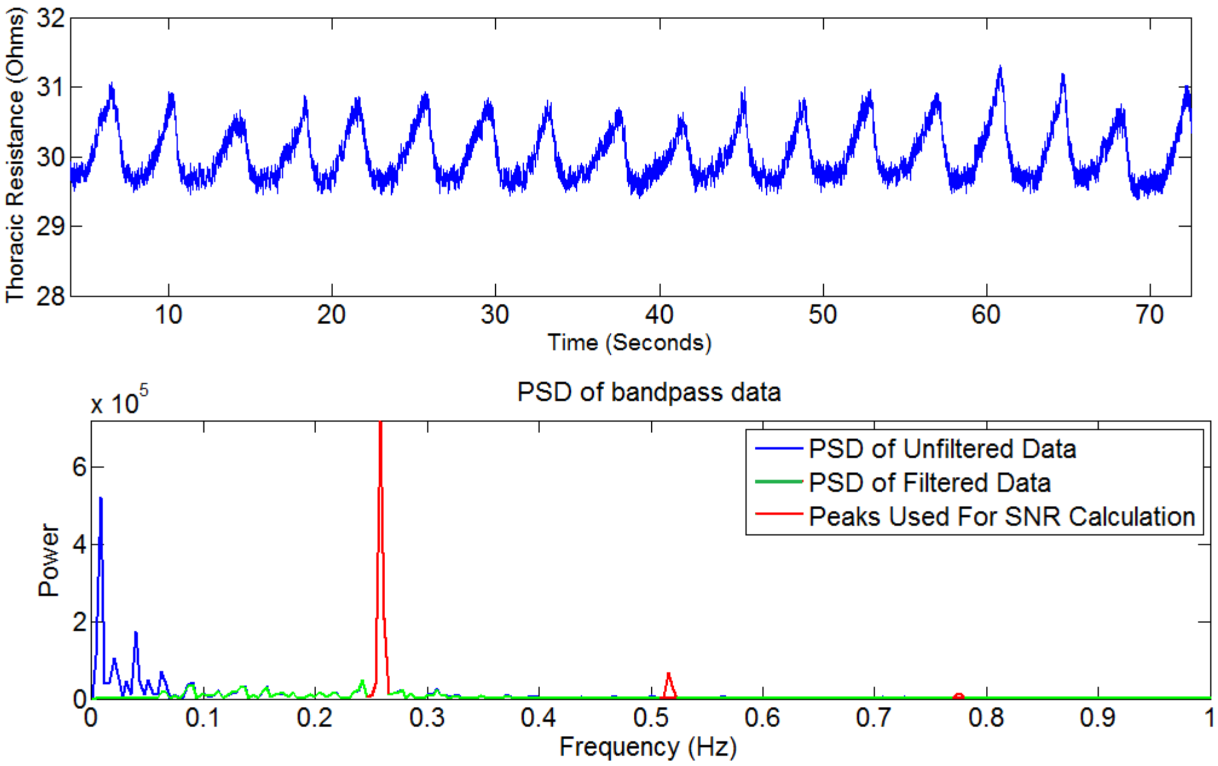

Figure 5.17: Sample BioZ respiration data and PSD.

In order to estimate the SNR of the BioZ respiration signal, a metronome set to 31 beats per minute was used to pace normal breathing. Inhalation would occur on the first tick, exhalation on the second, and so on. The raw data is plotted in the top of figure 5.17, and PSD of the signal is present in the lower plot. The blue plot is the PSD of the raw signal, the green plot is a result of the application of a 2^{nd} order Butterworth bandpass filter with corner frequencies of $0.066Hz$ and $0.4Hz$.

The SNR was calculated using the same technique as for the PPG signal (section 5.1.3, equation 5.4). The peaks in red were used for the SNR calculation. The SNR of the raw and filtered signals are 0.43 and 1.1, respectively. The noise of the unfiltered signal is 0.0809Ω RMS, and is computed from a short segment of signal where there was no change in the mean impedance.

5.1.5 Accelerometer

The accelerometer implementation involves a single IC which outputs the acceleration data in a digital format. The output of the accelerometer is expected to conform to the specification in its datasheet.

5.1.6 Summary

A summary of the computed SNR values is found in table 5.1.

	Unfiltered	Filtered
ECG	$28.8^{\dagger}$	$86^{\dagger}$
Commercial ECG	67.1	71.2
EMG	$25.37^{\dagger}$	
PPG Red	9.79	$15.6/21.4^{\triangledown}$
PPG Infrared	3.78	$4.27/18^{\triangledown}$
Commercial PPG	2.56	$2.54/7.77^{\triangledown}$
Respiration (BioZ)	0.43	1.1

Table 5.1: Summary of SNR values, expressed as a ratio, not in dB. (†)60Hz notch filter applied. (▽)LPF/Bandpass Filter applied.

5.2 Human Trials

A number of human trials were performed to both examine the performance of *The Berkeley Tricorder* in the context of long term ambulatory use. Additionally, the hardware has been used in a number of studies to acquire ambulatory physiologic data to explore topics ranging from activities of daily living to stress induction.

5.2.1 Usability Studies (1 & 2)

Two sets of human trials have been performed with a total of 24 participants ranging from 18 to 62 years of age. The subjects were fitted with the device, and asked to wear the strap for 24 hours while keeping a log of their daily activity. Fitting involved determining the ideal electrode placements along the strap and routing wires from the device to the electrodes. After the subject was fitted, a PC application was used to connect to the device via Bluetooth to validate that all the signals were being recorded. The firmware was programmed to shut down the Bluetooth connection 30 minutes after being powered on.

Our initial goal was to place a reflective sensor on the chest along with the other electrodes. Unfortunately, we found dermal vascular perfusion on the chest to be insufficient for SpO_2 measurement. As a result, we used a reflective forehead sensor (Figure 4.34a) which provided an excellent SNR and is minimally influenced by motion artifacts.

The Bluetooth telemetry worked well under most cases, however, the device was placed under the left arm which caused significant signal degradation while the arm was covering the device. In subsequent trials the device was mounted either in the center of the chest or on the arm to avoid the problem. We can achieve telemetry distances of up to 10m with a clear line of sight. In addition, the Bluetooth implementation worked quite well in automatically reestablishing broken connections.

In the version of *The Berkeley Tricorder* used in these trials, the PPG circuit suffered from noise from the digital supply being coupled onto the LED (see section 4.2.3 for further details). This problem was solved in the next version of the hardware by use of a better voltage reference to drive the Light-Emitting Diode (LED) constant current circuit. We also had problems with the signal saturating the transimpedance amplifier which was solved by reducing the first stage gain and increasing the second stage gain.

The memory card was ejected prematurely from the first subject so an enclosure was built to keep the memory card secure before being placed in the strap. The reported comfort of the system varied greatly based on the individual. Most people stated that the device was comfortable, except the electronics package bothered them while they were sleeping. The strap, although made of elastic material, was still a bit too restrictive for some subjects. The worst complaint received was from an overweight subject who resorted to putting additional bits of cloth under the strap for added comfort.

Some subjects exercised at the gym, and reported that their sweat made the electrodes, especially the forehead sensor, somewhat irritating. The forehead sensor has two plastic bulges where the LEDs and photodiode are encapsulated. Most subjects reported mild topical irritations after wearing the headband overnight, with an underweight subject reporting pain.

The device performed very well under most conditions, allowing for rich parameter extraction such as heart rate, respiration rate, respiration tidal volume, and pulse transit time.

5.2.2 Activities of Daily Living Study

A study was performed with version 7 of *The Berkeley Tricorder* by another lab member involving analyzing activities of daily living. Two accelerometers were required for this study, mounted in different locations. In order to accommodate the requirements, a Bluetooth enabled accelerometer was purchased (WiTilt from Sparkfun) and mounted on a different location on the body. The firmware in the CSR Bluetooth stack was modified to connect to the WiTilt module, and the *The Berkeley Tricorder's* firmware was modified to to collect data from the remote accelerometer. The remote data was stored alongside the locally acquired data on the the Secure Digital (SD) card for offline processing.

The ability to also incorporate data from 3^{rd} party sensors allows a simple method of expanding the ability of the *The Berkeley Tricorder* platform.

5.2.3 Trier Stress Study

A large study was undertaken to induce stress in a population of students using the Trier Social Stress Test (TSST). This study is further detailed in chapter 6.

Chapter 6

Ambulatory Stress Monitoring

6.1 Introduction

Evolutionarily, it is believed that stress played a role in survival by increasing arousal and through activation of the fight-or-flight response in the presence of danger[23]. However, in the context of contemporary society, chronic stress plays a negative role. Chronic stress has been associated with with a wide range of physiological diseases such as cardiovascular disease, cancer, diabetes, infection diseases and immune system dysregulation[22, 30, 31]. Additionally, there is strong evidence linking stress with a range of mental diseases such as depression, anxiety, and schizophrenia [33].

Although most everyone can relate to and intrinsically understand the notion of stress, the scientific community has been unable to provide a single definition or an agreed upon methodology of quantification stress. It has been stated that there are as many definitions of stress as there are stress researchers[108].

The wide range of definitions for stress and hence the inability to quantify stress make it difficult to study stress and the relationship between stress and disease. To date, the most common tools researchers utilize in stress research are subjective questionnaires, scales, and inventories which try to gauge levels of anxiety, depression, short term stressors, major life events, social interactions, etc. However, the sheer number and diversity of these "questionnaires" make it difficult to compare results between studies and risk measuring the "wrong kind of stress."

Another tool utilized by researchers are stress hormones such as cortisol which have been shown to vary in relationship to stress and can be measured in both blood and saliva [20]. However, there is generally a lag time of 10 minutes between the onset of stress and elevations in cortisol levels[62], and the samples need to be sent to a lab for analysis. Additionally, levels of natural cortisol secretion vary throughout the day with peak levels in the morning, and must be accounted for. This makes it difficult to use cortisol for long term ambulatory studies.

The ability to use a non-invasive non-subjective measure of stress would be of great value value in helping in better understanding the relationship between stress and disease as well and unifying research in the field. We aim to explore the relationship between stress and quantifiable physiological measures which relate to the autonomic nervous system, a key mediator of stress.

6.2 Background & The Autonomic Nervous System

Numerous researchers have explored the autonomic nervous system as a key mediator of stress, and there is substantial evidence to support this [95, 117]. The Autonomic Nervous System (ANS) has two branches, the Sympathetic Nervous System (SNS) and the Parasympathetic Nervous System (PNS) which originate in the central nervous system and innervate many of the body's organs. The SNS is responsible for the fight or flight response which prepares the body for action by increasing it's metabolic capacity, dilating the pupils, etc. The PNS is responsible for digestion and the body's "restorative activities". Stress has been shown to increase SNS activity and decrease PNS activity.

These systems often, though not always, affect organs in opposing ways. Activation of the SNS will increase heart rate, whereas activation of the PNS will decrease heart rate. Their actions are coordinated in that an increase in SNS activity is often accompanied by a decrease in PNS activity - and vise versa - through there are exceptions such as sexual arousal where activity increases in both systems.

In the context of disease, the ANS is also an interesting target to explore. Many of the diseases associated with stress can be influenced by the ANS. For example, stress is believed to play an important role in Crohn's disease[22]. Crohn's disease is an autoimmune disease of the Gastro-Intestinal (GI) tract in which aggressive inflammatory responses results in stricture or fissure formation in the GI tract. A powerful mediator of inflammation is Tumor Necrosis Factor Alpha (TNS-α). The release of TNS-α is regulated through the cholinergic anti-inflammatory pathway, which is mediated by the PNS[115, 118]. Though not yet established as a causative link, what is known is that stress decreases PNS activity, that decreased PNS activity increases production of TNS-α, and that TNS-α is an important mediator of inflammation in the GI system.

The link between the ANS and numerous other diseases also exist. Elevated SNS activity can result in hypertension[99], the aforementioned inflammatory response has been linked to plaque formation in atherosclerosis[64], and decreased PNS activity can even accelerated aging[67].

Additionally, many de-stressing activities that people perform also act upon the ANS. Yoga has been shown to increase PNS activity[59], as well as listening to relaxing music[55].

Based on this evidence, in the context of disease, being able to measure the level of PNS and SNS activity in a continuous ambulatory fashion would be greatly aid in stress research, understanding the relationship between stress and disease, as well as exploring methodologies to mitigate stress through feedback.

6.2.1 Measuring Autonomic Nervous System Activity

The gold standard for measuring ANS activity is through pharmacological blockade studies. Administration of a β-blocker such as propranolol will block epinephrine receptors, the neurotransmitter associated with the SNS. As SNS activity increases heart rate, blocking this branch of the ANS will cause a decrease in the heart rate. Next, administration of atropine will block acetylcholine receptors, the neurotransmitter associated with the PNS which likewise causes an increase in heart rate by blocking the effects of the PNS. The change in heart rate associated with with the administration of atropine after propranolol is proportional to the level of PNS activity (figure 6.1). However, this is a very invasive technique and not suitable to ambulatory monitoring.

An alternative method to measure ANS activity is by measuring Heart Rate Variablity (HRV)[111], a non-invasive technique that has been shown to have a high degree of correlation with results form

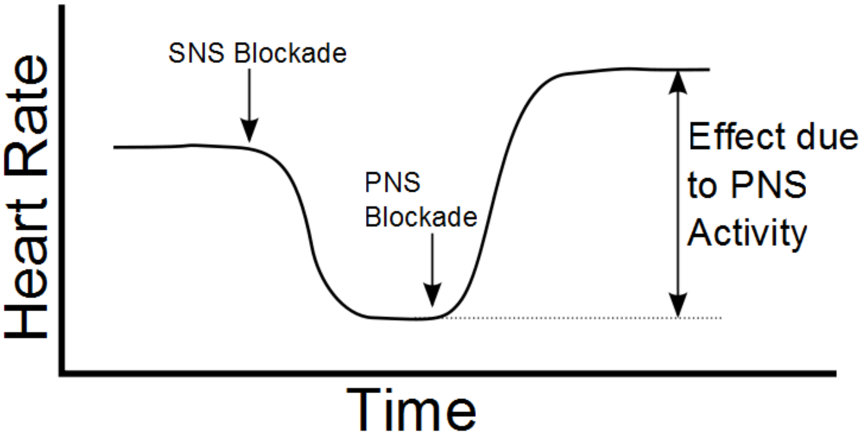

Figure 6.1: Pharmacological blockade study to determine level of PNS activity

Metric	How Measured	SNS	PNS
Heart Rate	ECG	+	-
Peripheral Sweat Gland Activity	Skin Conductance	+	0
Respiration Rate	BioImpedance	+	-
Blood Pressure	Pulse Transit Time	+	-
Vascular Tone	Photoplethysmograph	+	-
Muscle Tone	Electromyogram	+	-

Table 6.1: Physiological Metrics Affected By The Autonomic Nervous System

pharmacological blockade studies[50]. This technique relies a feedback loop between the respiratory system and the heart which is mediated by the PNS. The effects of this feedback system can be measured which is proportional to the level of PNS activity.

During inhalation, heart rate increases, and during exhalation, the heart rate decreases - an effect known as Respiratory sinus arrhythmia (RSA). By measuring instantaneous heart rate per beat, and analyzing the amount of energy in the range 0.15Hz-0.4Hz (corresponding to the RSA), one can can determine the level of of PNS activity. This method is most accurate under paced breathing.

6.2.2 Additional Measures of ANS Activity

Beyond heart rate variability analysis, there are a number of other physiological parameters that are influenced by the ANS that we can measure in order to improve our estimate of PNS/SNS activity. Some of these parameters are summarized in table 6.1.

6.3 Methods

The basis of the study is to induce stress in a number of individuals while they are wearing The Berkeley Tricorder. Physiologic metrics will be measured continuously and stored on the device throughout the duration of the study. Along with the physiologic measurements, salivary cortisol, a stress hormone, will be sampled and used as a ground truth along with a subjective evaluation from the subjects. The goal of the study is to determine which physiologic metrics yield the best quantitative estimate of stress.

6.3.1 Stress Induction Protocol

We conducted a stress inducing study based on Trier Social Stress Test (TSST) [62]. The TSST allows experimenters to induce stress under laboratory conditions. TSST has been successfully replicated in many research studies.

TSST is unique because it involves social stress, including scenarios of social evaluation stress and the anticipation stress before that. It is arguably more representative of the stress that people experience in day to day activity. The participants were asked to prepare for an interview with hiring managers for their "dream job". The task came unexpected, so anticipating stress was raised.

A main component of the TSST is that the subjects are placed in front of a panel of "hiring managers" that will not provide any emotional feedback. This lack of feedback is a strong exacerbation factor to further increment stress levels. The panel was composed of two very intimidating actors who were hired to play the part of the managers. The actors were dressed in formal suites to induce an aura of seriousness and authenticity to the study, and they were instructed to provide zero facial, verbal or body language feedback. The actors were both female and male, in order to balance any gender bias.

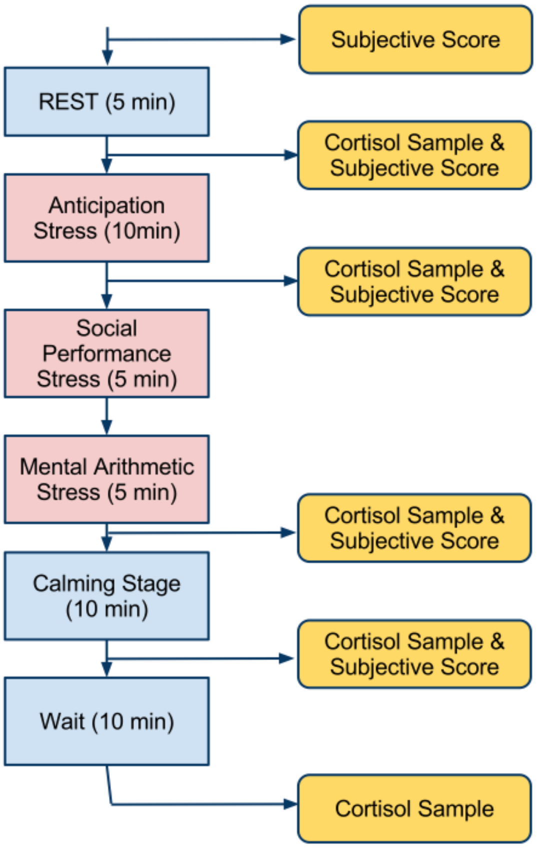

Figure 6.2: Overview of Study Protocol

As it can be seen in figure 6.2, the overall flow of the study is composed of 6 stages. The stages in blue are calming, and the stages in red are stress inducing. After arriving, the subject were fitted with the physiologic monitor and asked what their perceived subjective stress levels were, on a scale from 1-10. The nature of the study was not made apparent to the subjects until the conclusion of the study. The following details the six stages of the study. Between each stage, the subjects were asked to rate their perceived stress and a salivary cortisol sample was taken, with the exception of the of the period after the 3rd stage. The 3rd and 4th stages occurred back-to-back in front of the panel of hiring managers, and it was not possible to interact with the subjects.

1. The subjects were asked to close their eyes and try to relax for 5 minutes. This allows for a baseline "relaxed" measurement.

Modality	Sampling Rate	Bandwidth	Resolution
Electrocardiogram (ECG)	1024Hz	0.8Hz - 200Hz	12 bits
Electromyogram (EMG)	1024Hz	8Hz - 200Hz	12 bits
Bioimpedance (BioZ)	256 hz	1kHz - 100kHz	16 bits complex
Photoplethysmograph (PPG)	256Hz	DC - 3.4kHz	15 bits
Accelerometer	256Hz	DC - 200Hz	8 bits/axis
Skin Conductance	256Hz	DC - 16Hz	12 bits

Table 6.2: Tricorder Device Summary

2. The subjects were taken to the room of hiring managers and presented with their task. They were told that they were applying to get their dream job, and that they had 10 minutes to prepare a speach as to why they should be hired. They were then led back into a waiting room to prepare. This segment of the study is meant to induce anticipation stress.

3. After 10 minutes of preparation, the subjects were taken back to the room with the hiring managers and were given 5 minutes to give their speech. This phase is meant to induce social anxiety stress.

4. After they delivered their speech, they were presented with a mathematical problem. They were asked to subtract 13 from 2087, and to keep subtracting 13 from the resulting number. If they made a mistake, they were asked to start over again. Mental arithmetic is a common way to induce stress[108].

5. At the end of the stress induction phase, the nature of the study was explained to the subjects, and they were provided a period of 10 minutes to rest.

6. An additional 10 minutes of waiting ensued before the final cortisol sample to account for the lag in time before changes in salivary cortisol levels.

In addition to asking the subjects what their perceived stress levels were, they were presented with two questionnaires which are used in assessing stress. They included the Positive Affect and Negative Affect (PANA) questionnaire [119] and the State Trait Anxiety Inventory (STAI) [58]. The study protocol was approved by the University of California at Berkeley Institutional Review Board and the subjects were undergraduate students from UC Berkeley.

6.3.2 Wireless Physiological Monitor

The Berkeley Tricorder was used to collect ambulatory physiologic data throughout the study. The device was optimized to reflect the required parameters for this study, and is summarized in Table 6.2. Additionally, a daughter-board utilizing variable gain amplifier design was used for electrodermal conductivity measurements to allow for the wide dynamic range required for the measurements.

The monitor was affixed to the upper arm of the non-dominant hand in a pouch with Velcro. Commercial Ag-AgCl fingertip electrodermal conductivity electrodes (MLT117F ADInstruments) along with conductive paste (MLA1095 ADInstruments) were used for the skin conductance measurement and placed on the middle and ring finger of the non-dominant hand. A fingertip pulse

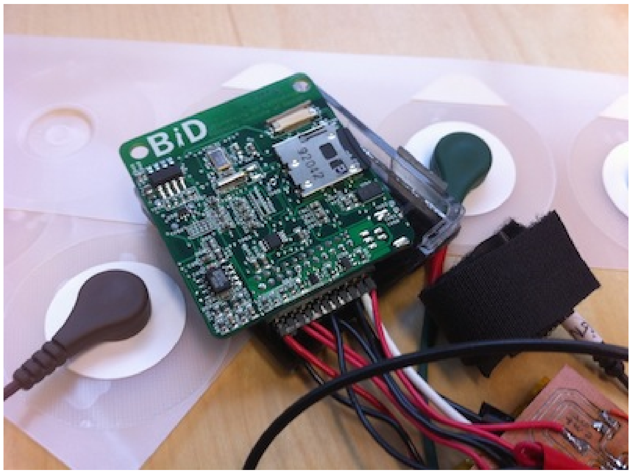

Figure 6.3: Wireless monitor with sensors

oximeter sensor (Nellcor DS-100) was placed on the index finger of the non-dominat hand. Standard Ag-AgCl pre-gelled electrodes were used for the ECG, EMG and BioZ measurements. A pair of EMG electrodes were placed on the trapezius muscle of the non-dominant hand. Tension in the trapezius muscle have been correlated with stress[73]. The BioZ respiration measurement was performed using a tetrapolar electrode configuration with two current electrodes and two pickup electrodes. A $350\mu A$ peak to peak ($175\mu A$ peak) current source electrode and a ground electrode were placed on either side of the torso, and a pair of differential pickup electrodes were placed centered on the front of the torso. The differential pickup electrodes were also used as inputs to the ECG amplifier. All leads were routed to the pouch containing the monitor.

After affixing the device to the subject, a laptop was used to connect to the monitor over Bluetooth to view real-time biometrics and to validate all the signals were being acquired correctly. Raw data was simultaneously recorded on the microSD card on a FAT16 formatted filesystem on the unit. The current time was transmitted from the laptop to *The Berkeley Tricorder* in order to configure a real time clock running on the hardware. This timestamp was also recorded in the data-stream so the periods of physiologic activity recorded could be correlated with the different stages of the TSST.

6.3.3 Feature Extraction

The physiologic data was recorded in a raw format. Features, such as heart rate from raw ECG voltages, were extracted in matlab for analysis.

Heart Rate

A lightweight peak and slope extraction technique inspired by the Canny edge detection algorithm[24] was developed and utilized for a number of vital signs. First, a 16-point power spectrum of the normal distribution was convolved forwards and backwards with the raw ECG waveform in order to smooth it. It was determined that the downward slope between the R-peak and S-trough was a dominant feature and provided a robust method for localizing the QRS-complex in the ECG waveform. The derivative of the waveform was determined by subtracting subsequent points from each other; the local minimum of the derivative provides a fiduciary marker of the QRS-complex.

The local minimums were found by examining in the lower 10th percentile of values in the 2-second moving window. For a point to be considered a local minimum, it required the point that proceeded it and the point that followed it to both be of a higher value that the point itself.

The time between these points were used as a measure of the time between heart beats (RR time), and the inverse of this is the heart rate.

The algorithm then computed a running average of heart rate, and rejected any points which would cause 50% increase in the instantaneous heart rate. This method proved to be very fast and accurate at detecting QRS-complexes.

Heart Rate Variability

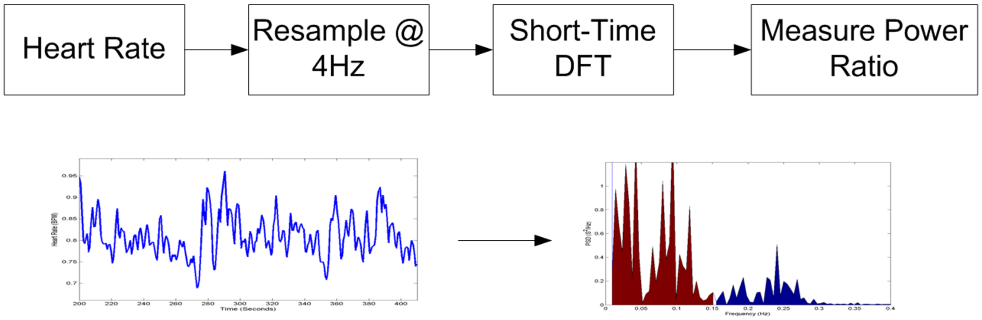

Figure 6.4: Steps involved in computing HRV. Resampled heart rate in the left plot. Power spectrum on a 210 second window on the right. The ratio of power in the blue section to that in the red section is proportional to the level of PNS/SNS activity.

Heart rate variability was analyzed through non-parametric frequency analysis utilizing a set of matlab scripts[1] developed by Danny Kaplan and Phil Staffin (Macalester College, St. Paul, MN). The process involves the following steps (figure 6.4).

1. Take RR time series data from section 6.3.3 and resample to derive an evenly spaced heart rate at 4Hz.

2. Find outlier points and perform a spline fit over the HR data to remove noise. Ideally, the ECG data is examined manually to detect missing or miss-marked peaks.

3. Perform a short-time Fourier transform of a 210 second window with a 205 second overlap and compute the power spectrum between 0.003Hz-0.15Hz (low-frequency) and 0.15Hz-0.4Hz (high-frequency). The ratio of high-frequency to low-frequency represents the ratio of PNS to SNS activity.

The higher the HRV metric, the more PNS activity is present.

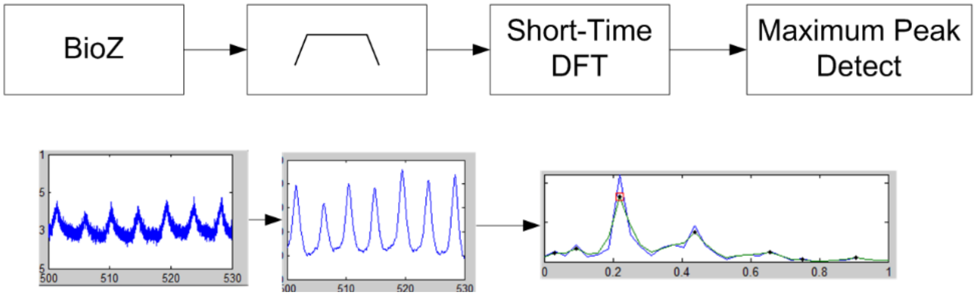

Figure 6.5: Steps involved in computing respiration rate. The first plot is the raw BioZ data, second plot is the filtered BioZ data, and the third plot is a short-time FFT with the dominant peak identified.

Respiration Rate

The technique developed at the Virginia Commonwealth University[8] was adapted to extract the respiration rate from the Bioimpedance (BioZ) signal. The BioZ signal was filtered by a 2^{nd} order butterworth filter from 0.066Hz-.4Hz, and a short-time FFT was performed with a window of 30 seconds with a 5 second overlap. The frequency of the dominant peak was determined to be the respiration rate at that time (figure 6.5).

Pulse Transit Time

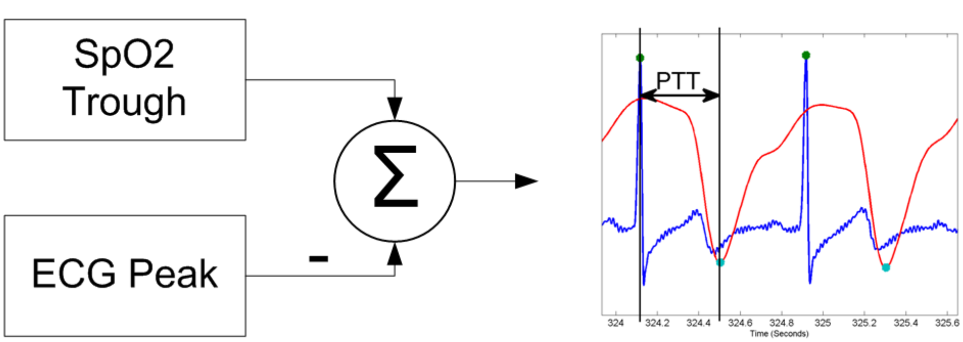

Figure 6.6: Steps involved in computing the pulse transit time. The ECG peaks and the PPG troughs are detected and the time difference between them is the PTT.

Pulse Transit Time (PTT) has been shown to correlate with relative changes in blood pressure and is the measure of the blood pulse wave velocity. A pulse wave will propagate through an elastic tube at a rate that is proportional to the inverse of the compliance of the tube. As blood pressure increases, the vessel walls become less compliant and the pulse wave travels faster. For this measure, we first bandpass filtered the signal using a 6th order butterworth filter from 0.5Hz-5hz. We then used the same technique as described in section 6.3.3 except we find the minimum of the pulse oximeter waveform (minimum measured light) rather than the minimum slope of the signal. We expected that these points would occur at the same frequency as the heart rate and

---

[1] http://www.macalester.edu/~kaplan/hrv/doc/

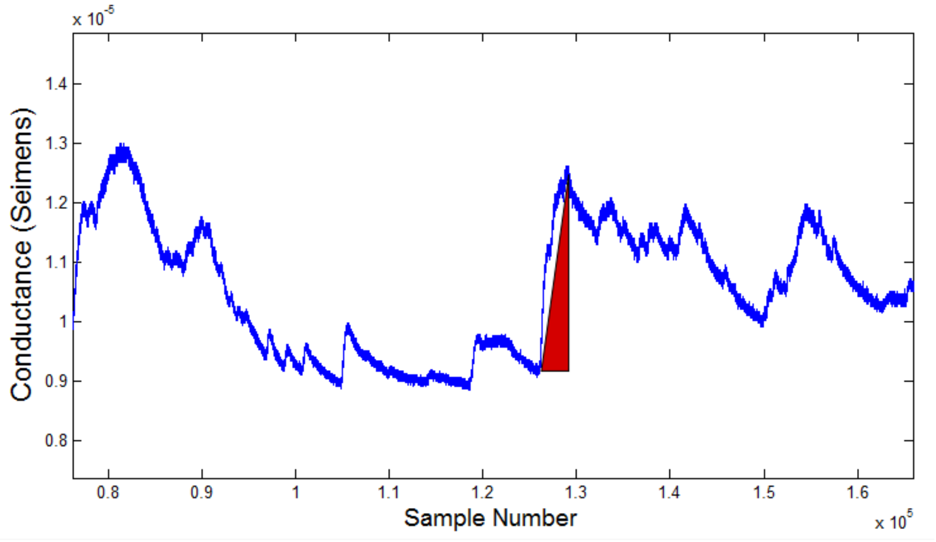

Figure 6.7: Sample electrodermal conductivity signal. Triangle represented computed EDC value for that peak.

disregarded any points that are outliers. We then computed the time difference between the the RS point measured in section 6.3.3 and the minimum value of the pulse oximeter signal (figure 6.6). The duration between the peak of the R-wave and the RS point was found to be fixed and did not affect the PTT measurement.

Electromyogram

The EMG signal was filtered with a 4th order butterworth filter between 5Hz-500Hz and the standard deviation of the signal over a moving 1 second window was computed. Additionally, the maximum peak to peak values over the same window were computed.

Vascular Tone

This metric was identified after examining the data and noting large variations in the amplitude of the PPG signal collected at various stages of the study. The greater the amount of blood flowing through the fingers, the larger the amplitude of the PPG signal. The relative vascular tone was computed using the same technique as for the EMG signal.

Electrodermal Conductivity

The Electrodermal Conductivity (EDC) increases as sweat is secreted by sweat glands, and decreases as the fluids evaporate or are reabsorbed. The same peak detection method as described in section 6.3.3 was used to find a trough followed by a peak. The size of the peak was determined by the area of the triangle as depicted in figure 6.7. As EDC is a slow signal, the sum of all such triangles over a window of 60 seconds were used to represent the level of EDC activity over that period.

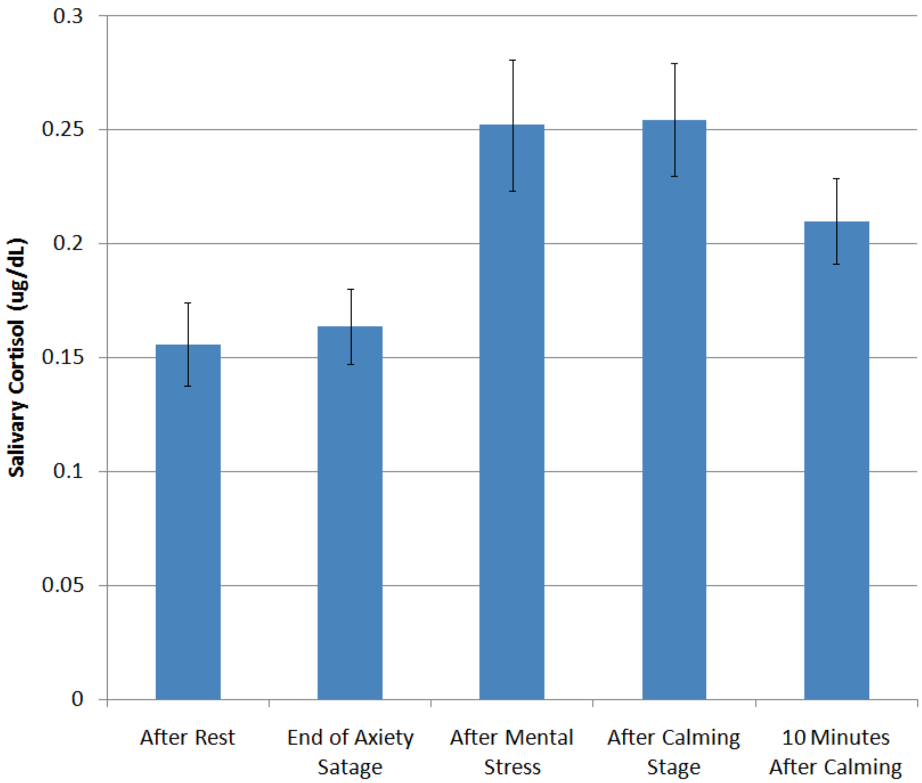

Figure 6.8: Change in cortisol levels at various stages in the study. Average and SEM values shown (n=44).

6.3.4 Cortisol Measurements

Cortisol is a stress hormone produced by the adrenal gland through the Hypothalamic pituitary adrenal axis, and has been demonstrated to increase as a result of stress. Each subject had 4 salivary cortisol readings performed at key points in the study and one additional reading 10 minutes after the end of the study due to the approximate 10 minute lag in the response of cortisol to stress[62] (figure 6.2). The study was performed in the afternoon (between 13:00-18:00) to minimize the effect of natural changes in cortisol levels through the duration of the study due to circadian rhythm where the maximal changes occur in the morning. The samples were collected by use of a Salivette (Sarstedt AG & Co.) and frozen during the duration of the study. Analysis was performed by the salimetrics salivary cortisol assay at the University of California, San Francisco.

6.4 Analysis & Results

The cortisol and subjective stress scores are first analyzed to determine the efficacy of the TSST in inducing stress. The physiologic data is then examined to determine which measurements best correlate with the induced stress.

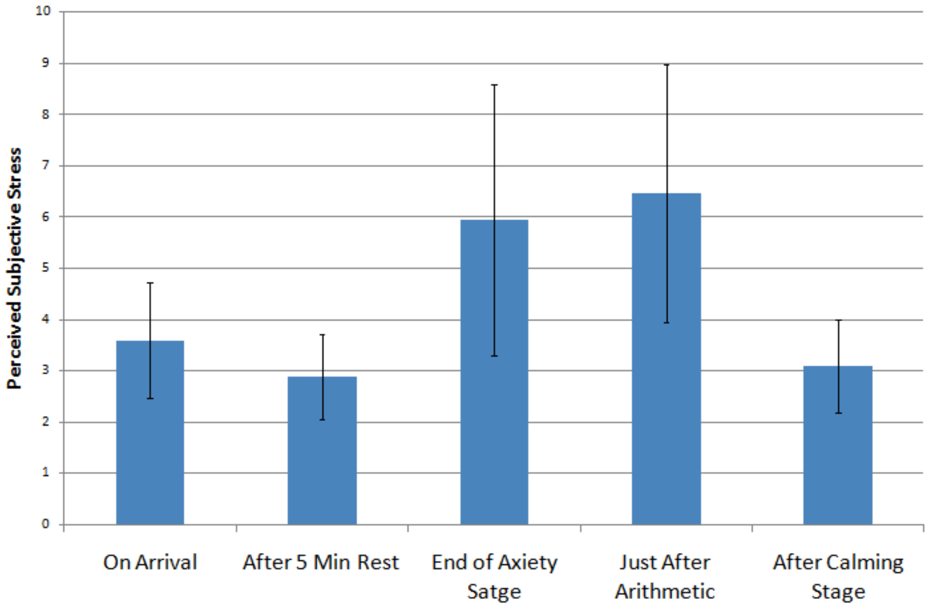

Figure 6.9: Average perceived subjective stress score with SEM. 1-10 scale; 10 highest stress.

6.4.1 Cortisol

Initial cortisol levels at the beginning of the study for each subject were compared with the hour the study began, and no significant differences were determined (ANOVA p=0.360). Mean and the Standard Error of the Mean (SEM) across subjects are plotted in figure 6.8. Note that we expect cortisol levels to lag stress by 10 minutes, so the measurement for “10 Minutes After Calming” represents the stress state “After Calming State”, and the measurement “After Calming State” represents the stress state “After Mental Stress,” et cetera. Taking the cortisol lag time into account, salivary cortisol levels were found to have been elevated after after the anxiety stress and presentation phases of the study, and decreased after the calming stage, indicating a physiological stress response. The differences in cortisol levels in figure were found to be statistically significant (ANOVA p<.001).

6.4.2 Subjective Perceived Stress

Subjective scores (1-10; 10 being the highest) were collected at times indicated in figure 6.2 (figure 6.9). A nonparametric rank-based analysis was performed which showed a significant difference between the levels of perceived stress (Friedman statistic, χ^2 = 85, p<0.001, n=30). As expected, the perceived stress increased as a result of the stressing stages and decreased after the calming stage.

6.4.3 Physiological Data

A sample of the collected physiologic data is presented in figure 6.10. The different phases of the study are marked. Heart rate is plotted as a frequency, PTT is plotted as number of seconds and is expected to decrease with increased blood pressure, HRV is plotted as the ratio of PNS/SNS and is

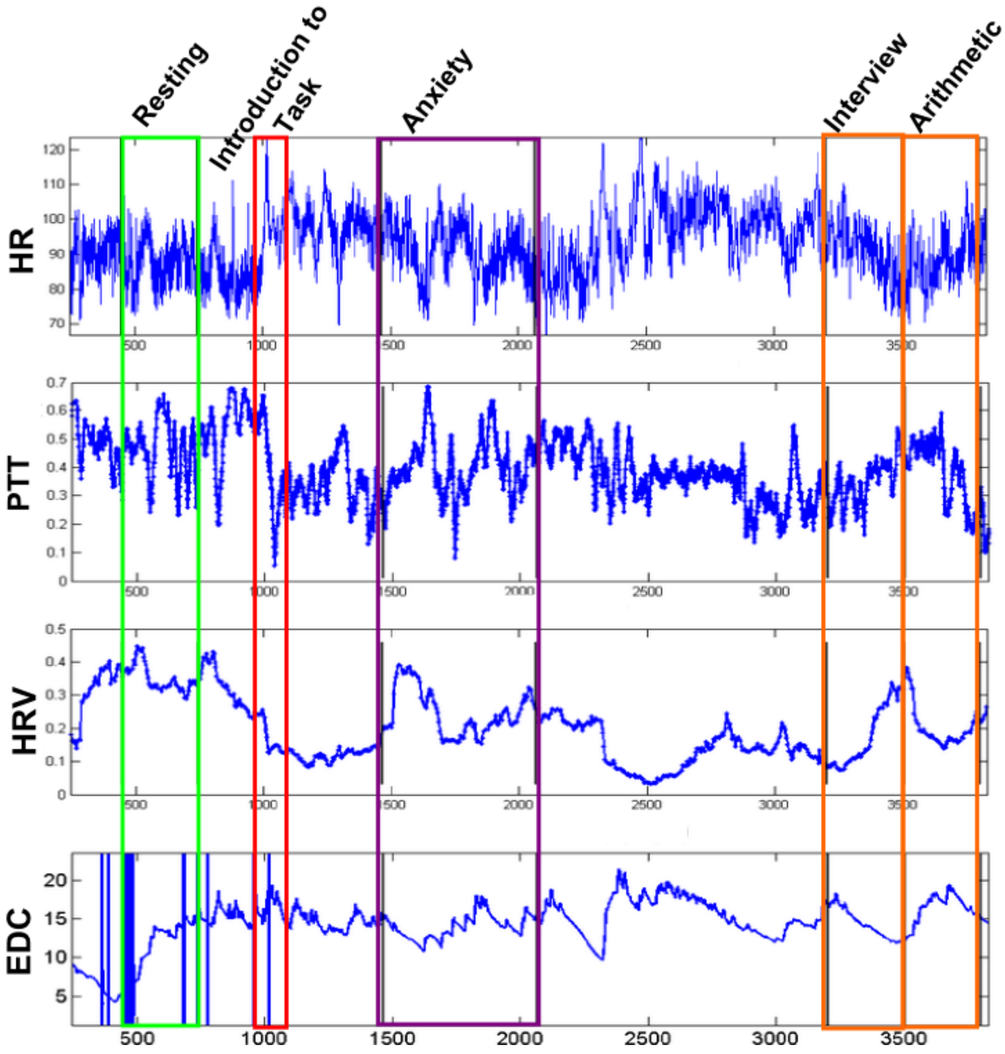

Figure 6.10: Sample data collected through the study from one subject.

expected to decrease with stress, and EDC is plotted as $\mu Siemens$ and is expected to increase with stress.

Note that the point where the subjects were introduced to the panel of hiring managers (red square), they exhibited a dramatic changes in the physiologic parameters, all indicating a stressful experience.

Principle Components

A principle components analysis was performed to explore the significance of the various variables in predicting stress.

Data computed from section 6.3.3 was resampled at 1Hz. The average value for the various metrics over the resting state, the anxiety state, the interview, and the mental arithmetic portion of the study were computed. The leading and trailing 60 seconds of data in these windows was not used due to inadequate resolution in the the timestamps associated with these states. Subjects that

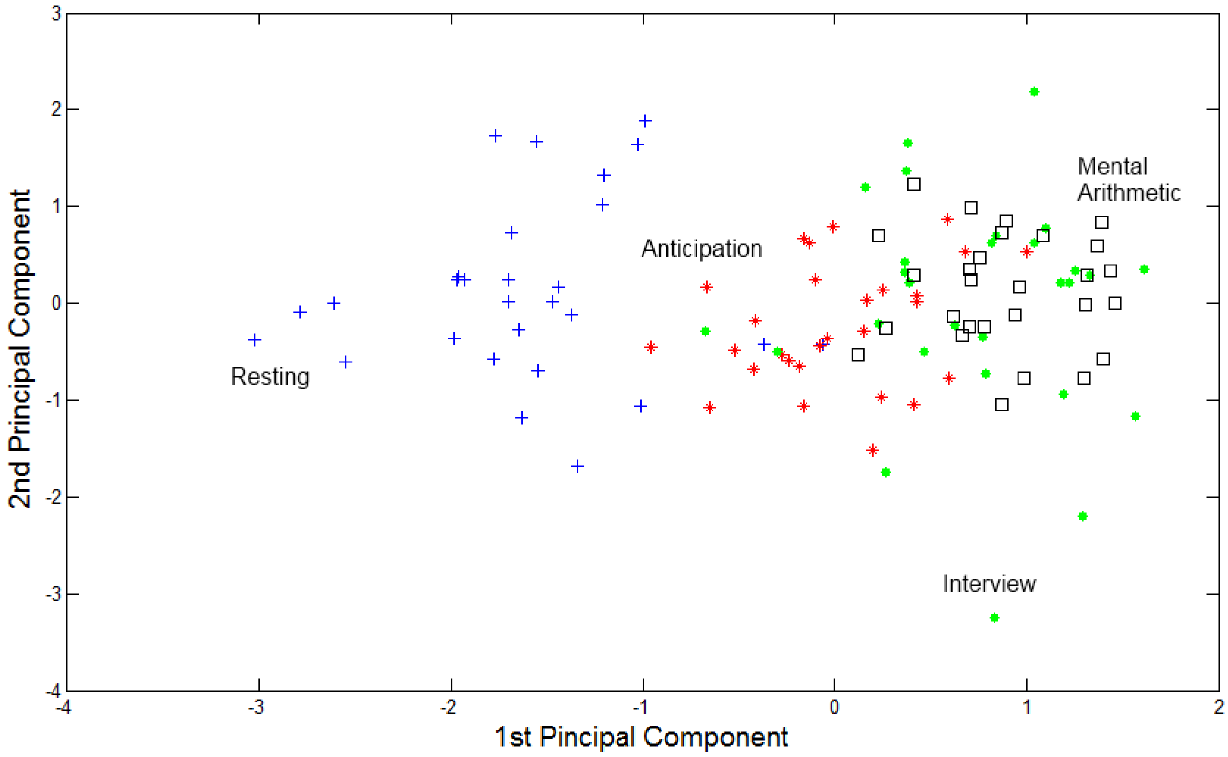

Figure 6.11: Principal component analysis from extracted features.

had missing timestamps in their records were excluded from the analysis.

The method used to extract respiration data was not found sufficiently robust, and was excluded from the analysis. The EMG signal suffered from excessive external interference[2] and was also excluded from the analysis.

The values were normalized by subtracting the mean and and dividing by the standard deviation for each signal across the duration of the study per subject. The Principal component analysis was performed on the resulting normalized values for each of the four states and plotted in figure 6.11. The 1st principal component is capable of segregating the data collected from the resting stage from the data collected from the other stress inducing stages. To a lesser degree, it is capable of segregating the data from the anticipation stage from the stages in front of the hiring managers. It is not possible to discriminate between the mental arithmetic stage and the interview stage.

Metric	**Coefficient**
HR	0.51
HRV	-0.31
PTT	-0.1
Vascular Tone	0.57
EDC	0.43

Table 6.3: Coefficients of the first principal component of figure 6.11.

The coefficients associated with the 1st principle component are summarized in table 6.3. As expected, increasing SNS activity increases HR, decreases HRV, decreases PTT, increases vascular tone, and increases EDC all are signs of increasing stress. The coefficients demonstrate this

---

[2] Possibly from the florescent lighting

relationship.

Linear Regression

A simple linear regression model was constructed in order to see if changes in physiologic parameters could be used to predict changes in the subjective perceived stress score. As before, the various metrics (HR, HRV, PTT, etc.) were computed and averaged for each metric over the various phases in the study (resting, anxiety, interview/arithmetic)[3]. The phases are give indexes 0 through 2, respectively. We then assign the average value for the heart rate of subject i during period j to the variable $\overline{HR}_{ij}$. The average values for heart rate variability are likewise assigned to the variables $\overline{HRV}_{ij}$, and so on.

As individuals all have different baseline values for the various physiologic parameters, the initial resting value was subtracted from the anxiety, interview, and arithmetic phases. For example,

$$\overline{HR'}_{i1} = \overline{HR}_{i1} - \overline{HR}_{i0}$$

$$\overline{HR'}_{i2} = \overline{HR}_{i2} - \overline{HR}_{i0}$$

And so on. The linear model we are solving takes the form of

$$Y = X\beta + \epsilon$$

Where X includes all the averages for all the metrics, subjects, and periods. X is defined as

$$X = \begin{bmatrix} 1 & \overline{HR'}_{11} & \overline{HRV'}_{11} & \overline{PTT'}_{11} & \overline{VasularTone'}_{11} & \overline{EDC'}_{11} \\ 1 & \overline{HR'}_{12} & \overline{HRV'}_{12} & \overline{PTT'}_{12} & \vdots & \vdots \\ 1 & \overline{HR'}_{21} & \overline{HRV'}_{21} & \overline{PTT'}_{21} & \vdots & \vdots \\ 1 & \overline{HR'}_{22} & \overline{HRV'}_{22} & \overline{PTT'}_{22} & \vdots & \vdots \\ \vdots & \vdots & \vdots & \vdots & \vdots & \vdots \\ 1 & \overline{HR'}_{N2} & \overline{HRV'}_{N2} & \overline{PTT'}_{N2} & \overline{VasularTone'}_{N2} & \overline{EDC'}_{N3} \end{bmatrix}$$

Likewise, we let the subjective perceived stress score for subject i during period j be equal to $\overline{S}_{ij}$. We are only interested in the change in stress from the baseline, so the resting subjective score is subtracted from the subjective scores from the other phases.

$$\overline{S'}_{i1} = \overline{S}_{i1} - \overline{S}_{i0}$$

$$\overline{S'}_{i2} = \overline{S}_{i2} - \overline{S}_{i0}$$

Thus Y is defined as

---

[3] No subjective score was taken taken after the interview phase, so data from the interview and arithmetic stages are averaged.

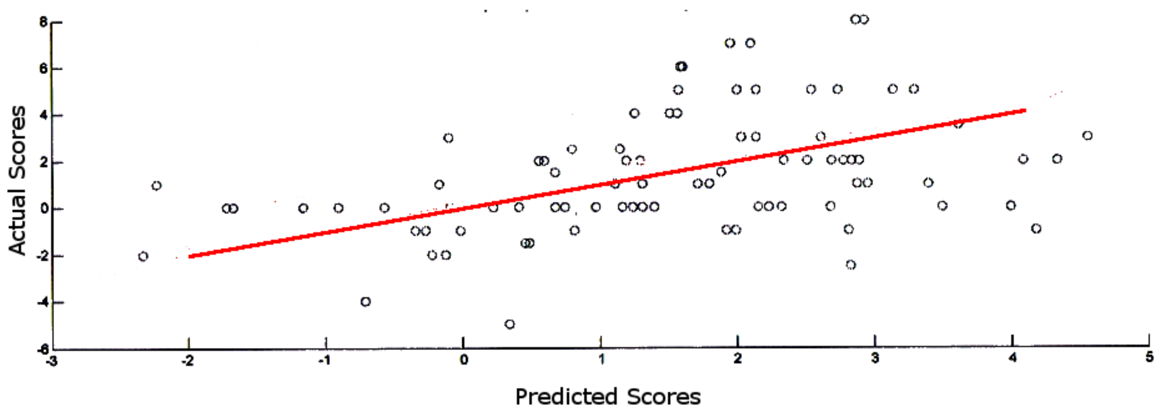

Figure 6.12: Predicted vs. actual perceived stress scores for all subjects. Correlation=0.404.

$$Y = \begin{bmatrix} \overline{S'}_{11} \\ \overline{S'}_{12} \\ \overline{S'}_{21} \\ \overline{S'}_{22} \\ \vdots \\ \overline{S'}_{N2} \end{bmatrix}$$

We can then solve for the matrix β with a goal of minimizing the residuals, ϵ.

The matrix β can then be used to try to predict a subjective score given a set of physiologic data. The data from a subject was withheld, and the matrix β was trained using data from all other subjects. It was then used to compute the subjective stress score for the withheld subject. This was repeated for all subjects, and the results were plotted in figure 6.12. The correlation of the predicted vs. actual perceived stress was 0.404.

6.5 Discussion

We explored the relationship between physiology and stress in the context of the autonomic nervous system. Our aim was to find a set of non-invasive physiological measures that can be used in an ambulatory setting, and that are capable of providing a reliable measure of stress by means of the autonomic nervous system. The trier social stress test was chosen as it better represented real-world stress, and it did so in an ambulatory fashion requiring subjects to walk from room to room, to sit, stand, and to interact naturally. We also collected salivary cortisol, subjective perceived stress scores, audio recordings of speech as well as a number of questionnaires. Both the salivary cortisol and the subjective stress scores indicate that the study did induce stress. The questionnaires and audio recordings will be used for a different research project.

Additionally, the ambulatory nature of the study introduced motion artifacts which made feature extraction difficult for some of the signals. This was most pronounced with the PPG, which is known to be highly susceptible to motion artifacts, and corrupted portions of the pulse transit time feature. As the interview and mental arithmetic stages of the study required speech, the respiratory BioZ signal was not sufficiently robust to provide a respiration rate during speech. There are different techniques[101] beyond the frequency analysis which may provide a better measure of respiration with noisy signals. We also did not find much value in the EMG signal from the trapezius and suspect it as not being useful in the ambulatory situations with motion. As motion data was recorded from the accelerometer, it is worth considering using it as an indicator of confidence for the signals that are susceptible to motion artifacts and incorporating it into the analysis.

There is clustering of the physiological metrics in the principal component analysis (figure 6.11) with the resting state appearing on the left and the stress states appearing on the right. The first principal component was dominated by a combination of heart rate and heart rate variability metrics, and accounted for 41% of the variance in the data. This is not surprising as both heart rate and heart rate variability are highly influenced by the ANS, which we believe is the dominant mediator of stress. Both the resting and the anticipation states occurred under identical physical circumstances - with the subject left alone sitting in a room - yet there is a clear distinction between the two cases in the principal component analysis. Both the interview and mental arithmetic occurred under the same physical circumstance as well - with the subject standing in front of the panel. The distinction between the resting and interview/mental arithmetic stages is less clear as the subject was standing versus sitting which can also influence heart rate and heart rate variability.

Additionally, we explored the possibility of using a linear system to describe how the change in one's physiology maps to changes in perceived stress. This was a gross simplification of the complexities of the relationship between physiology and mental state, however we were able to derive correlation of 0.404 which exceeded our expectations.

Chapter 7

Future/Ongoing Work

A number of derivative projects have been implemented which implement a subsection of the functionality of *The Berkeley Tricorder*.

7.1 Ear PulseOx Sensor

A small (1.5" x .5") Bluetooth-enabled ear worn PPG (figure 7.1) has been developed for continuous blood oxygenation and heart rate monitoring for a number of applications including monitoring for hypoxemia and continuous stress levels. The sensor includes 4 bright RGB Light-Emitting Diodes (LEDs) for displaying the status of the individual.

7.2 Edema Monitor for Congestive Heart Failure

A dedicated Bluetooth-enabled Bioimpedance (BioZ) spectrometer (figure 7.2) has been developed in conjunction with an Android tablet (figure 7.3) to assess edema in patients with Congestive Heart Failure (CHF).

CHF patients are required to monitor their fluid levels. This is currently performed by daily weight measurements and noting sudden increases in weight as a result of increased water retention. Once water retention is detected, drugs can be used to return the fluid levels to normal. However, compliance with this task is sufficiently low that a large number of patients require hospitalization.

A study is currently underway at the congestive heart failure department at John Muir Hospital in Walnut Creek, CA to assess the sensitivity in using bioimpedance spectrometry to detect variations in peripheral edema for suffers of CHF.

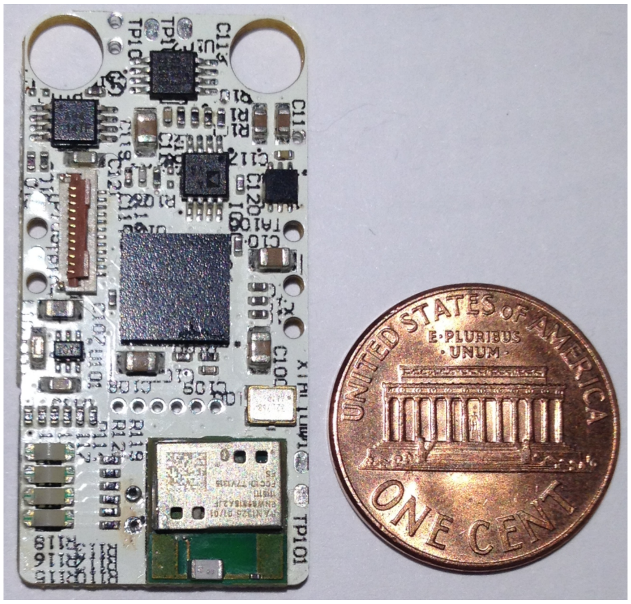

Figure 7.1: Ear-worn PPG

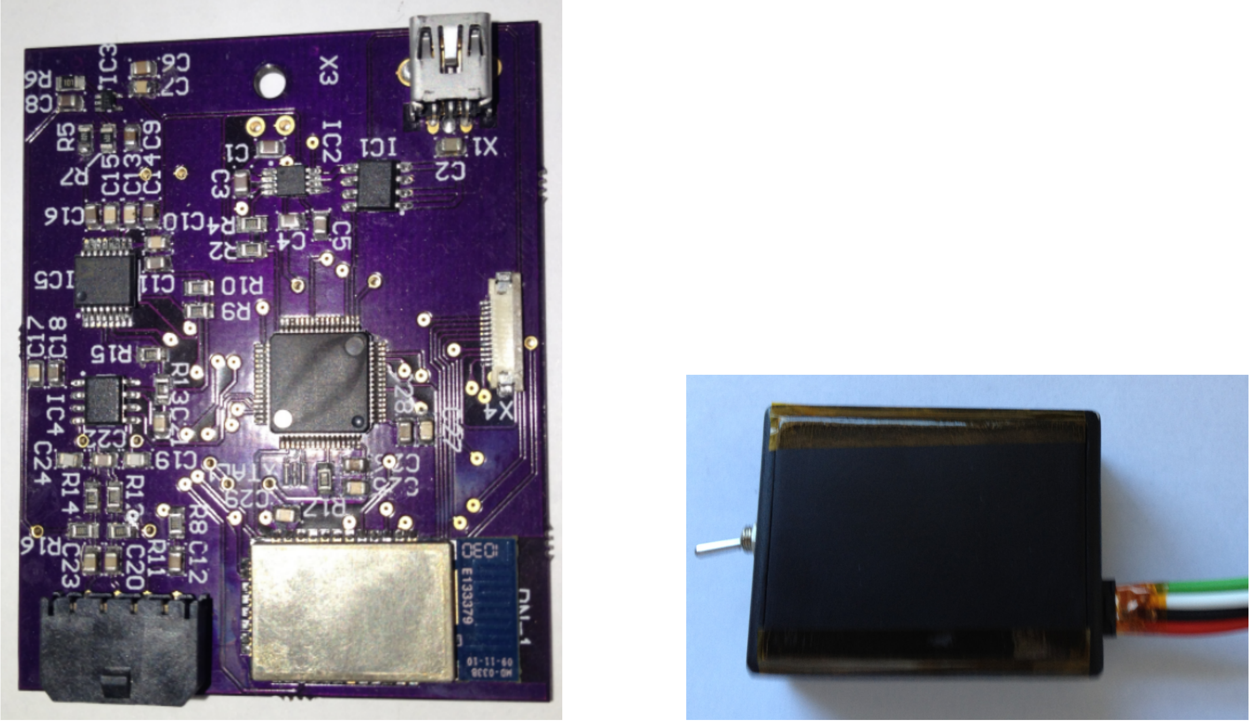

(a) PCB

(b) Device in enclosure

Figure 7.2: Bioimpedance Spectrometer for Edema Monitoring

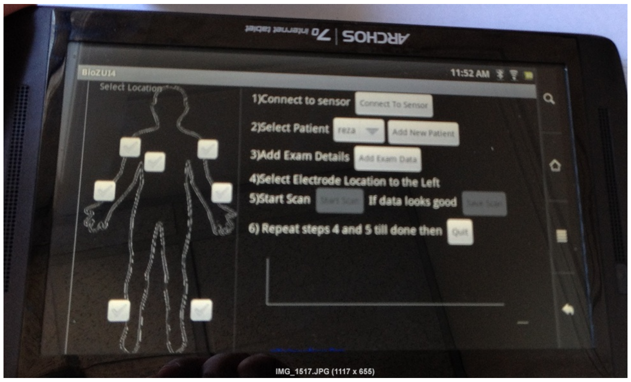

1)Connect to sensor

2)Select Patient

3)Add Exam Details

4)Select Electrode Location to the Left

5)Start Scan If data looks good

6) Repeat steps 4 and 5 till done then

Figure 7.3: Android tablet acting as bioimpedance spectrometer user interface and data aquisition system.

Bibliography

[1] Wiley Encyclopedia of Biomedical Engineering. John Wiley & Sons, INC.

[2] Extracting breathing rate information from a wearable reflectance pulse oximeter sensor. pages 1–4, Jun 2009.

[3] J Ahlgren. Kinesiology of the mandible an emg study. *Acta Odontologica*, 25(6):593–612, 1967.

[4] Metin Akay. *Wiley Encyclopedia of Biomedical Engineering, 6-Volume Set*. Wiley-Interscience, April 2006. ISBN 9780471249672. URL `http://books.google.com/books?id=uS6fSQAACAAJ`.

[5] RD Allison, EL Holmes, and J Nyboer. Volumetric dynamics of respiration as measured by electrical impedance plethysmography. *Journal of Applied Physiology*, 19(1):166–173, 1964. URL `http://jap.physiology.org/content/19/1/166.short`.

[6] M Altmann and U Pliquett. Prediction of intramuscular fat by impedance spectroscopy. *Meat Science*, 2006. URL `http://linkinghub.elsevier.com/retrieve/pii/S0309174005003542`.

[7] P Annus, A Kuusik, R Land, O Martens, and A Ronk. A digital multichannel bioimpedance analyser: Signal processing task and its solution. *Instrumentation and Measurement Technology Conference*, Jan 2006. URL `http://ieeexplore.ieee.org/xpls/abs_all.jsp?arnumber=4124574`.

[8] S Ansari, K Najarian, and K Ward. Extraction of Respiratory Rate from Impedance Signal Measured on Arm: A Portable Respiratory Rate Measurement Device. ... *and Biomedicine*, 2009. URL `http://ieeexplore.ieee.org/xpls/abs_all.jsp?arnumber=5341815`.

[9] S M Ardeshna, M Flanagan, Y L Ng, and K Gulabivala. An ex vivo investigation of the relationship between apical root impedance and canal anatomy. *International Endodontic Journal*, 44(6):525–533, February 2011. doi: 10.1111/j.1365-2591.2011.01857.x. URL `http://doi.wiley.com/10.1111/j.1365-2591.2011.01857.x`.

[10] John Ardizzoni. The Incredible Versatile Op Amp in Medical Applications. *Analog Devices Inc, Technical Article MS-1946*, pages 1–3, October 2010. URL `http://www.analog.com/static/imported-files/tech_articles/MS-1946.pdf`.

[11] Fabio Bagalà, Clemens Becker, Angelo Cappello, Lorenzo Chiari, Kamiar Aminian, Jeffrey M Hausdorff, Wiebren Zijlstra, and Jochen Klenk. Evaluation of Accelerometer-Based Fall Detection Algorithms on Real-World Falls. *PLoS ONE*, 7(5):e37062, May 2012. doi: 10.1371/journal.pone.0037062.t002. URL `http://dx.plos.org/10.1371/journal.pone.0037062.t002`.

[12] SJ Barker and KK Tremper. Pulse oximetry: applications and limitations. *International anesthesiology clinics*, 1987. URL `http://ukpmc.ac.uk/abstract/MED/3323062`.

[13] A Barreto, J Zhai, and M Adjouadi. Non-intrusive physiological monitoring for automated stress detection in human-computer interaction. *Human–Computer Interaction*, pages 29–38, 2007.

[14] J Basmajian and C De Luca. Muscles alive. In *PROCEEDINGS OF THE ...*, 1985. URL `http://rheumatology.oxfordjournals.org/cgi/issue_pdf/backmatter_pdf/7/4.pdf`.

[15] L Beckmann, D van Riesen, and S Leonhardt. Optimal electrode placement and frequency range selection for the detection of lung water using Bioimpedance Spectroscopy. *Engineering in Medicine and Biology Society, 2007. EMBS 2007. 29th Annual International Conference of the IEEE*, pages 2685–2688, 2007. URL `http://ieeexplore.ieee.org/xpls/abs_all.jsp?arnumber=4352882`.

[16] AK Bourke, JV O'Brien, and GM Lyons. Evaluation of a threshold-based tri-axial accelerometer fall detection algorithm. *Gait and Posture*, 26(2):194–199, 2007.

[17] DM Buchner and EH Wagner. Preventing frail health. - Abstract - UK PubMed Central. *Clinics in geriatric medicine*, 1992. URL `http://ukpmc.ac.uk/abstract/MED/1576567`.

[18] A Sonia Buist, Mary Ann McBurnie, William M Vollmer, Suzanne Gillespie, Peter Burney, David M Mannino, Ana MB Menezes, Sean D Sullivan, Todd A Lee, Kevin B Weiss, Robert L Jensen, Guy B Marks, Amund Gulsvik, and Ewa Nizankowska-Mogilnicka. International variation in the prevalence of COPD (The BOLD Study): a population-based prevalence study. *The Lancet*, 370(9589):741–750, September 2007. doi: 10.1016/S0140-6736(07)61377-4. URL `http://www.thelancet.com/journals/lancet/article/PIIS0140-6736(07)61377-4/fulltext`.

[19] HC Burger and JB Van Milaan. Heart-vector and leads. *British heart journal*, 10(4):229, 1948.

[20] HM Burke, MC Davis, and C Otte. ScienceDirect - Psychoneuroendocrinology : Depression and cortisol responses to psychological stress: A meta-analysis. *Psychoneuroendocrinology*, 2005. URL `http://linkinghub.elsevier.com/retrieve/pii/S0306453005000831`.

[21] MJ Burke and MV Whelan. Photoplethysmography: Selecting optoelectronic components. *Medical and Biological Engineering and Computing*, 24(6):647–650, 1986. URL `http://www.springerlink.com/index/01165028Q200136H.pdf`.

[22] Rafael J A C aacute mara, Roger Ziegler, Stefan Begr eacute, Alain M Schoepfer, and Roland von K auml nel. The Role of Psychological Stress in Inflammatory Bowel Disease: Quality Assessment of Methods of 18 Prospective Studies and Suggestions for Future Research. *Digestion*, 80(2):129–139, 2009. doi: 10.1159/000226087. URL `http://www.karger.com/doi/10.1159/000226087`.

[23] Walter Bradford Cannon. Bodily changes in pain, hunger, fear and rage. NEW YORK AND LONDON D. APPLETOX AND COMPANY, 1927. URL `http://books.google.com/books?id=Nw4LAAAAYAAJ`.

[24] John Canny. A Computational Approach to Edge Detection. *IEEE TRANSACTIONS ON PATTERN ANALYSIS AND MACHINE INTELLIGENCE*, 8:679–698, November 1986. URL `http://ieeexplore.ieee.org/stamp/stamp.jsp?tp=&arnumber=4767851`.

[25] P Castiglioni, L Piccini, M Di Rienzo, FDG Centro di Bioingegneria, FD Gnocchi, and I Milan. Interpolation technique for extracting features from ECG signals sampled at low sampling rates. *COMPUTERS IN CARDIOLOGY*, pages 481–484, 2003.

[26] AYK Chan. Biomedical Device Technology: Principles And Design , 2008. URL `http://books.google.com/books?hl=en&lr=&id=al9LufqNF4UC&oi=fnd&pg=PR1&dq=biomedical+device+technology+principles+and+design&ots=7ud1_vUv0t&sig=yqxKZYzPeKpOfgsBuP1NaQubF98`.

[27] Y Chen. IEEE Xplore - Abstract Page. *Communications*, 2002. URL `http://ieeexplore.ieee.org/xpls/abs_all.jsp?arnumber=996891`.

[28] Jongyoon Choi, Beena Ahmed, and Ricardo Gutierrez-Osuna. Ambulatory Stress Monitoring with Minimally-Invasive Wearable Sensors. *Department of Computer Science and Engineering, Texas A&M University, Technical Report*, pages 1–8, November 2010.

[29] Ivaylo I Christov and Todor V Stovanov. Steep slope method for real time QRS detection. *Electrotechnics & Electronics E+ E*, 2001. URL `http://www.clbme.bas.bg/pwp/todor_stoyanov/qrs%20detect%20ee.htm`.

[30] S Cohen. Stress and infectious disease in humans. *Psychological Bulletin*, 109(1):5–24, 1991. URL `http://psycnet.apa.org/journals/bul/109/1/5/`.

[31] S Cohen, D Janicki-Deverts, and G Miller. Psychological stress and disease. *Jama*, 2007. URL `http://jama.ama-assn.org/cgi/content/full/298/14/1685`.

[32] KS Cole and RH Cole. Dispersion and absorption in dielectrics I. Alternating current characteristics. *The Journal of Chemical Physics*, 9:341, 1941.

[33] C Corcoran, E Walker, R Huot, V Mittal, K Tessner, L Kestler, and D Malaspina. The stress cascade and schizophrenia: etiology and onset. *Schizophrenia Bulletin*, 29(4):671, 2003.

[34] B H Cornishi, B J Thomast, and L C WARD. Improved prediction of extracellular and total body water using impedance loci generated by multiple frequency bioelectrical impedance analysis. *Phys. Med. Biol.*, (38):337–346, January 1993.

[35] G Cotter, Y Moshkovitz, E Kaluski, and A Cohen. Accurate, noninvasive continuous monitoring of cardiac output by whole-body electrical bioimpedance*. *Chest*, Jan 2004. URL `http://www.chestjournal.org/cgi/content/abstract/125/4/1431`.

[36] G Cotter, Y Moshkovitz, E Kaluski, A Cohen, and H Miller. Accurate, noninvasive continuous monitoring of cardiac output by whole-body electrical bioimpedance. *Chest*, 2004. URL `http://www.ncbi.nlm.nih.gov/pubmed/15078756`.

[37] S E Crouter. A novel method for using accelerometer data to predict energy expenditure. *Journal of Applied Physiology*, 100(4):1324–1331, December 2005. doi: 10.1152/japplphysiol.00818.2005. URL `http://jap.physiology.org/cgi/doi/10.1152/japplphysiol.00818.2005`.

[38] Alvaro A Cruz and World Health Organization. Global surveillance, prevention and control of chronic respiratory diseases, 2007. ISBN 9789241563468. URL `http://books.google.com/books?hl=en&lr=&id=gdj5iU5FrXEC&oi=fnd&pg=PR5&dq=global+surveillance+prevention+and+control+of+chronic+respiratory+dieseases&ots=EtX-6FD8lD&sig=D8aKFVY7hN-uGGmIF93YTVNC0vU`.

[39] CA DeVito, DA Lambert, and RW Sattin. Fall injuries among the elderly. Community-based surveillance. . *Journal of the ...*, 1988. URL `http://ukpmc.ac.uk/abstract/MED/3171040`.

[40] Paul Duffty and M. Heather Bryan. Home Apnea Monitoring in 'Near-Miss' Sudden Infant Death Syndrome (SIDS) and in Siblings of SIDS Victims. 1982.

[41] C Earthman, D Traughber, J Dobratz, and W Howell. Bioimpedance spectroscopy for clinical assessment of fluid distribution and body cell mass. *Nutrition in Clinical Practice*, 22 (4):389, 2007.

[42] D Freimark, M Arad, and R Sokolover. ... content in CHF patients under intravenous diuretics treatment using bio-impedance .... *Physiological ...*, 2007. URL `http://www.cardio-inspect.com/diuretics_PM.pdf`.

[43] L Geddes, M Voelz, and C Babbs. Pulse transit time as an indicator of arterial blood pressure. *Psychophysiology*, Jan 2007. URL `http://www3.interscience.wiley.com/journal/119574157/abstract`.

[44] B Gerdle, S Karlsson, S Day, and M Djupsjöbacka. Acquisition, processing and analysis of the surface electromyogram. *Modern techniques in neuroscience*, pages 705–755, 1999.

[45] E Goldberger. A simple, indifferent, electrocardiographic electrode of zero potential and a technique of obtaining augmented, unipolar, extremity leads. *American Heart Journal*, 23 (4):483–492, 1942.

[46] Dean A Gratton. *Bluetooth profiles*. the definitive guide. Prentice Hall PTR, 2003. ISBN 9780130092212. URL `http://books.google.com/books?id=08eByqhzJ3wC&printsec=frontcover&dq=bluetooth+profiles&ie=ISO-8859-1&cd=1&source=gbs_api`.

[47] S Grimnes. Bioimpedance and bioelectricity basics - Sverre Grimnes, Ørjan Grøttem Martinsen - Google Books, 2008. URL `http://books.google.com/books?hl=en&lr=&id=v3EuUjoqwkkC&oi=fnd&pg=PP2&dq=bioimpedance+and+bioelectricity+basics&ots=OWNeV2vr-j&sig=rT0gLt-M26T1y5hMNZ8KIsrTX9c`.

[48] S Grimnes and ØG Martinsen. *Bioimpedance*. 2006.

[49] B Grundlehner, L Brown, J Penders, and B Gyselinckx. The Design and Analysis of a Real-Time, Continuous Arousal Monitor. *Wearable and Implantable Body Sensor Networks, 2009. BSN 2009. Sixth International Workshop on*, pages 156–161, 2009.

[50] J Hayano, Y Sakakibara, A Yamada, M Yamada, S Mukai, T Fujinami, K Yokoyama, Y Watanabe, and K Takata. Accuracy of assessment of cardiac vagal tone by heart rate variability in normal subjects. *The American journal of cardiology*, 67(2):199–204, 1991.

[51] STEVEN B HEYMSFIELD, DYMPNA GALLAGHER, JILL GRAMMES, CHRISTOPHER NUlqEZ, ZIMAN WANG, and ANGELO PIETROBELLI. Upper Extremity Skeletal Muscle Mass: Potential of Measurement with Single Frequency Bioimpedance Analysis. pages 1–2, February 2003.

[52] DM Hiestand, P Britz, and M Goldman. Prevalence of Symptoms and Risk of Sleep Apnea in the US Population*. *Chest*, 2006. URL `http://chestjournal.chestpubs.org/content/130/3/780.short`.

[53] Philip C D Hobbs. *Building Electro-Optical Systems*. Making It All Work. Wiley, September 2011. ISBN 9781118211090. URL `http://books.google.com/books?id=jV8PaQ_C_NoC&printsec=frontcover&dq=building+electro+optical+systems&ie=ISO-8859-1&cd=1&source=gbs_api`.

[54] SA Hosseini and MA Khalilzadeh. Emotional stress recognition system using EEG and psychophysiological signals: Using new labelling process of EEG signals in emotional stress state. *Biomedical Engineering and Computer Science (ICBECS), 2010 International Conference on*, pages 1–6, 2010.

[55] M Iwanaga and M. Tsukamoto. effects of excitative and sedative music on subjective and physiological relaxation. *Perceptual and motor skills*, 85(1):287–296, 1997. URL `http://www.ncbi.nlm.nih.gov/pubmed/9293589`.

[56] D.W. Jones and J.E. Hall. The National High Blood Pressure Education Program. *Hypertension*, 39(5):941–942, 2002. doi: 10.1161/01.HYP.0000018303.61360.28. URL `http://hyper.ahajournals.org/content/39/5/941.short`.

[57] M Kangas, A Konttila, P Lindgren, and I Winblad. Comparison of low-complexity fall detection algorithms for body attached accelerometers. *Gait and Posture*, 2008. URL `http://www.sciencedirect.com/science/article/pii/S096663620800026X`.

[58] Philip C Kendall and et al. The State-Trait Anxiety Inventory: A systematic evaluation. *Journal of Consulting and Clinical Psychology*, 44(3):406–412, 1976. doi: 10.1037/0022-006X.44.3.406. URL `http://content.apa.org/journals/ccp/44/3/406`.

[59] K Khattab, AA Khattab, and J Ortak. Iyengar yoga increases cardiac parasympathetic nervous modulation among healthy yoga practitioners. *Evidence Based ...*, 2007. URL `http://downloads.hindawi.com/journals/ecam/2007/801340.pdf`.

[60] K Kim and S Bang. Emotion recognition system using short-term monitoring of physiological signals. *Medical and biological engineering and ...*, 2004. URL `http://www.springerlink.com/index/RX11XP247627930L.pdf`.

[61] AC King and WJ Rejeski. Physical activity interventions targeting older adults. *American Journal of ...*, 2004. URL `http://archive.itee.uq.edu.au/~viller/projects/physicalActivity/KingAmerJnPrevMed.pdf`.

[62] C Kirschbaum, KM Pirke, and DH Hellhammer. The 'Trier Social Stress Test'—a tool for investigating psychobiological stress responses in a laboratory setting. *Neuropsychobiology*, 28(1-2):76–81, 1993.

[63] C Kitchin, L Counts, and M Gerstenhaber. Reducing RFI Rectification Errors in In-Amp Circuits. *Analog Devices Inc, Application Note (AN-671)*.

[64] WJ Kop. The Role of Immune System Parameters in the Relationship Between Depression and Coronary Artery Disease. *Psychosomatic Medicine*, 2005. URL `http://www.psychosomaticmedicine.org/content/67/Supplement_1/S37.short`.

[65] M Kraemer, C Rode, and V Wizemann. Detection limit of methods to assess fluid status changes in dialysis patients. *Kidney International*, 2006. URL `http://www.nature.com/ki/journal/v69/n9/abs/5000286a.html`.

[66] P. Kucera, Z. Goldenberg, and E. Kurca. Sympathetic skin response: review of the method and its clinical use. *BRATISLAVSKE LEKARSKE LISTY.*, 105(3):108–116, 2004. URL `http://www.bratislmedj.sk/2004/10503-05.pdf`.

[67] P Lee. Conditions of aging as manifestations of sympathetic bias unmasked by loss of parasympathetic function. *Medical Hypotheses*, 62(6):868–870, June 2004. doi: 10.1016/j.mehy.2003.11.024. URL `http://linkinghub.elsevier.com/retrieve/pii/S0306987704000052`.

[68] P Levy, J L Pepin, C Deschaux-Blanc, B Paramelle, and C Brambilla. Accuracy of Oximetry for Detection of Respiratory Disturbances in Sleep Apnea Syndrome. *Chest*, 109(2):395–399, February 1996. doi: 10.1378/chest.109.2.395. URL `http://www.chestjournal.org/cgi/doi/10.1378/chest.109.2.395`.

[69] W Liao, W Zhang, Z Zhu, and Q Ji. A Real-Time Human Stress Monitoring System Using Dynamic Bayesian Network. *Proceedings of the 2005 IEEE Computer Society Conference on Computer Vision and Pattern Recognition (CVPR'05)*, 2005.

[70] Konrad Lorincz and Matt Welsh. *Lecture Notes in Computer Science*, volume 3479 of *DavidHutchisonTakeoKanadeJosefKittlerJon M.KleinbergFriedemannMatternJohn C.MitchellMoniNaorOscarNierstraszC.Pandu RanganBernhardSteffenMadhuSudan-DemetriTerzopoulosDoughTygarMoshe Y.VardiGerhardWeikumLecture Notes in*

Computer Science0302-97431611-3349. Springer Berlin Heidelberg, Berlin, Heidelberg, 2005. ISBN 978-3-540-25896-4. doi: 10.1007/11426646{_}7. URL `http://www.springerlink.com/index/10.1007/11426646_7`.

[71] R Lumbroso, N Naas, and LK Beitel. Novel bioimpedance sensor for glucose recognition. ..., page 819, 2007. URL `http://ieeexplore.ieee.org/xpls/abs_all.jsp?arnumber=4294409`.

[72] U Lundberg, R Kadefors, B Melin, G Palmerud, P Hassmen, M Engström, and I Elfsberg Dohns. Psychophysiological stress and emg activity of the trapezius muscle. *International Journal of behavioral medicine*, 1(4):354–370, 1994.

[73] U Lundberg, R Kadefors, B Melin, G Palmerud, P Hassmen, M Engström, and I Elfsberg Dohns. Psychophysiological stress and EMG activity of the trapezius muscle. *International Journal of behavioral medicine*, 1(4):354–370, 1994.

[74] Suhuai Luo and Qinginao Hu. IEEE International Workshop on Biomedical Circuits and Systems, 2004. In *IEEE International Workshop on Biomedical Circuits and Systems, 2004.*, pages 25–28. IEEE, 2004. ISBN 0-7803-8665-5. doi: 10.1109/BIOCAS.2004.1454088. URL `http://ieeexplore.ieee.org/lpdocs/epic03/wrapper.htm?arnumber=1454088`.

[75] K Ma, JCT Khoo, and TIH Brown. Development of an ambulatory multi-parameter monitoring system for physiological stress related parameters. *Bioinformatics and Biomedical Technology (ICBBT), 2010 International Conference on*, pages 324–328, 2010.

[76] J Malmivuo, R Plonsey, and J Cameron. Bioelectromagnetism: principles and applications of bioelectric and biomagnetic fields. *Informa Pharma Science*, Jan 1995. URL `http://www.informapharmascience.com/doi/abs/10.3109/03091909609009004`.

[77] Robert G Maunder and Susan Levenstein. The role of stress in the development and clinical course of inflammatory bowel disease: epidemiological evidence. *Current molecular medicine*, 8:247–252, 2008. URL `http://www.ingentaconnect.com/content/ben/cmm/2008/00000008/00000004/art00002`.

[78] U Maurer, A Smailagic, D Siewiorek, and M Deisher. Activity recognition and monitoring using multiple sensors on different body positions. *Proceedings of the International Workshop on Wearable and Implantable Body Sensor Networks (BSN'06)*, 2006. URL `http://www.ece.cmu.edu/~bfrench/ewatch_files/papers/ewatch%20papers/01612909.pdf`.

[79] J Mawdsley and D Rampton. The role of psychological stress in inflammatory bowel disease. *Neuroimmunomodulation*, 2007. URL `http://content.karger.com/produktedb/produkte.asp?typ=fulltext&file=000104861`.

[80] R Merletti. Standards for reporting emg data. *J Electromyogr Kinesiol*, 9(1):3–4, 1999.

[81] JE Mietus, CK Peng, Ivanov, P.C., and AL Goldberger. Detection of obstructive sleep apnea from cardiac interbeat interval time series. *Computers in Cardiology 2000*, pages 753–756, 2000. URL `http://ieeexplore.ieee.org/xpls/abs_all.jsp?arnumber=898634`.

[82] MART MIN, TOOMAS PARVE, and ANDRES KINK. Thoracic Bioimpedance as a Basis for Pacing Controla. *Annals of the New York Academy of Sciences*, 873(1 ELECTRICAL BI):155–166, April 1999. doi: 10.1111/j.1749-6632.1999.tb09463.x. URL `http://doi.wiley.com/10.1111/j.1749-6632.1999.tb09463.x`.

[83] David F Moffett, Stacia B Moffett, and Charles L Schauf. *Human physiology*. foundations & frontiers. William C Brown Pub, February 1993. URL `http://books.google.com/books?id=RbpqAAAAMAAJ`.

[84] John T B Moyle. *Pulse oximetry*. BMJ Books, August 2002. ISBN 9780727917409. URL `http://books.google.com/books?id=FWVaHAAACAAJ&dq=intitle:Pulse+Oximetry+inauthor:moyle&hl=&cd=1&source=gbs_api`.

[85] VS Murthy, S. Ramamoorthy, N. Srinivasan, S. Rajagopal, and M.M. Rao. Analysis of photoplethysmographic signals of cardiovascular patients. *Engineering in Medicine and Biology Society, 2001. Proceedings of the 23rd Annual International Conference of the IEEE*, 3:2204–2207 vol. 3, 2001. URL `http://ieeexplore.ieee.org/xpls/abs_all.jsp?arnumber=1017209`.

[86] M NH and A Coster. Classification of basic daily movements using a triaxial accelerometer. *Medical and Biological Engineering and Computing*, 42:679–687, 2004. URL `http://d.wanfangdata.com.cn/NSTLQK_NSTL_QK8268033.aspx`.

[87] Robert B Northrop. *Noninvasive instrumentation and measurement in medical diagnosis*. CRC, 2002. ISBN 9780849309618. URL `http://scholar.google.com/scholar?q=related:X8Jb28eMDB4J:scholar.google.com/&hl=en&num=30&as_sdt=0,5`.

[88] N Noury. 2nd Annual International IEEE-EMBS Special Topic Conference on Microtechnologies in Medicine and Biology. Proceedings (Cat. No.02EX578). In *2nd Annual International IEEE-EMBS Special Topic Conference on Microtechnologies in Medicine and Biology. Proceedings*, pages 314–317. IEEE, 2002. ISBN 0-7803-7480-0. doi: 10.1109/MMB.2002.1002337. URL `http://ieeexplore.ieee.org/lpdocs/epic03/wrapper.htm?arnumber=1002337`.

[89] M Oehler, V Ling, K Melhorn, and M Schilling. A multichannel portable ecg system with capacitive sensors. *Physiological Measurement*, 29:783–793, 2008.

[90] Arne Öhman, Francisco Esteves, Anders Flykt, and Joaquim J F Soares. *Progress in Electrodermal Research*. Springer US, Boston, MA, 1993. ISBN 978-0-306-44536-1. doi: 10.1007/978-1-4615-2864-7{_}10. URL `http://www.springerlink.com/index/10.1007/978-1-4615-2864-7_10`.

[91] Ashok Vikhe Patil, K V Somasundaram, and R C Goyal. Current health scenario in rural India. *Australian Journal of Rural Health*, 10(2):129–135, April 2002. doi: 10.1046/

j.1440-1584.2002.00458.x. URL `http://doi.wiley.com/10.1046/j.1440-1584.2002.00458.x`.

[92] R Picard and C Du. Monitoring stress and heart health with a phone and wearable computer. *Motorola Offspring Journal*, 2002. URL `http://www.media.mit.edu/affect/pdfs/02.picard-du.pdf`.

[93] R Plonsey. Bioelectromagnetism: principles and applications of bioelectric and biomagnetic fields. Oxford University Press, USA, 1995. ISBN 9780195058239. URL `http://www.informapharmascience.com/doi/abs/10.3109/03091909609009004`.

[94] J Polastre, R Szewczyk, and D Culler. Telos: enabling ultra-low power wireless research. *Proceedings of the 4th international symposium on …*, Jan 2005. URL `http://portal.acm.org/citation.cfm?id=1147685.1147744`.

[95] S Porges. Cardiac vagal tone: A physiological index of stress. *Neuroscience & Biobehavioral Reviews*, 19(2):225–233, 1995. URL `http://linkinghub.elsevier.com/retrieve/pii/014976349400066A`.

[96] TL Rusch, R Sankar, and JE Scharf. Signal processing methods for pulse oximetry. *Computers in biology and medicine*, 26(2):143–159, 1996.

[97] K. Sato, WH Kang, K. Saga, and KT Sato. Biology of sweat glands and their disorders. I. Normal sweat gland function+. *Journal of the American Academy of Dermatology*, 20 (4):537–563, 1989. URL `http://www.sciencedirect.com/science/article/pii/S0190962289700633`.

[98] J Scharf, S Athan, and D Cain. Pulse oximetry through spectral analysis. *Biomedical Engineering Conference*, Jan 1993. URL `http://ieeexplore.ieee.org/xpls/abs_all.jsp?arnumber=247418`.

[99] E B Schroeder. Hypertension, Blood Pressure, and Heart Rate Variability: The Atherosclerosis Risk in Communities (ARIC) Study. *Hypertension*, 42(6):1106–1111, November 2003. doi: 10.1161/01.HYP.0000100444.71069.73. URL `http://hyper.ahajournals.org/cgi/doi/10.1161/01.HYP.0000100444.71069.73`.

[100] F Seoane, J Ferreira, and J Sanchéz. An analog front-end enables electrical impedance spectroscopy system on-chip for biomedical applications. *Physiological Measurement*, 2008. URL `http://iopscience.iop.org/0967-3334/29/6/S23/pdf/0967-3334_29_6_S23.pdf`.

[101] VP Seppä, J Väisänen, P Kauppinen, J Malmivuo, and J Hyttinen. Measuring respirational parameters with a wearable bioimpedance device. *13th International Conference on Electrical Bioimpedance and the 8th Conference on Electrical Impedance Tomography*, pages 663–666, 2007.

[102] VP Seppä, O Lahtinen, J Väisänen, and J Hyttinen. Assessment of breathing parameters during running with a wearable bioimpedance device. *Proceedings of the 4th European Congress for Medical and Biomedical Engineering*, 2008.

[103] M Shamir and C Weissman. Plethysmographic waveform variation as an indicator to hypovolemia. *Anesthesia & Analgesia*, Jan 2003. URL `http://www.anesthesia-analgesia.org/content/97/2/602.2.full`.

[104] Z Shinar, A Baharav, and S Akselrod. Obstructive sleep apnea detection based on electrocardiogram analysis. *Computers in Cardiology 2000*, pages 757–760, 2000. doi: 10.1109/CIC.2000.898635. URL `http://ieeexplore.ieee.org/xpls/abs_all.jsp?arnumber=898635`.

[105] M Shochat, G Charach, S Meyler, and S Meisel. Prediction of cardiogenic pulmonary edema onset by monitoring right lung .... *Intensive Care Medicine*, 2006. URL `http://www.springerlink.com/index/30HL852212M3N510.pdf`.

[106] Baha M. Sibai. Diagnosis and Management of Gestational Hypertension and Preeclampsia. *Obstetrics & Gynecology*, 102(1):181, July 2003. URL `http://journals.lww.com/greenjournal/Fulltext/2003/07000/Diagnosis_and_Management_of_Gestational.33.aspx`.

[107] R Sokolovsky, S Zlochiver, and S Abboud. Stroke volume estimation in heart failure patients using bioimpedance. *Physiological Measurement*, 2008. URL `http://www.iop.org/EJ/abstract/0967-3334/29/6/S12`.

[108] Mark A Staal. Stress, Cognition, and Human Performance: A Literature Review and Conceptual Framework. *NASA Technical Memorandum*, (NASA/TM—2004–212824):1–177, 2004.

[109] R Sung, P Lau, C Yu, and P Lam. Measurement of body fat using leg to leg bioimpedance. *Archives of Disease in Childhood*, 2001. URL `http://www.fetalneonatal.com/content/85/3/263.full`.

[110] R Sung, P Lau, C Yu, P Lam, and E Nelson. Measurement of body fat using leg to leg bioimpedance. *Archives of Disease in Childhood*, Jan 2001. URL `http://adc.bmj.com/cgi/content/abstract/85/3/263`.

[111] J Sztajzel. Heart rate variability: a noninvasive electrocardiographic method to measure the autonomic nervous system. *Swiss medical weekly*, 2004. URL `http://courses.ttu.edu/jrobert/Weblist%20HRV%20articles/Heart%20Rate%20Variability-%20a%20noninvasive%20electrocardiographic%20method%20to%20measure%20the%20autonomic%20nervous%20system.pdf`.

[112] Texas Instruments, Incorporated [SLAA281,B]. Interfacing the MSP430 With MMC/SD Flash Memory Cards (Rev. B). *Texas Instruments Application Report*, pages 1–5, January 2011. URL `http://www.ti.com/lit/an/slaa281b/slaa281b.pdf`.

[113] Andreas Tobola and Christian Douniama. Evaluation of alternative derivation areas for plethysmography and pulse oximetry. *Proceedings, SENSATION 2nd International Conference, Monitoring Sleep and Sleepiness with New Sensors within Medical and Industrial Applications*, pages 1–2, Jun 2007.

[114] Andreas Tobola and Christian Douniama. Evaluation Of Alternative Derivation Areas For Plethysmography And Pulse Oximetry. *Proceedings, SENSATION 2nd International Conference, Monitoring Sleep and Sleepiness with New Sensors within Medical and Industrial Applications*, pages 1–2, June 2007.

[115] KJ Tracey. The inflammatory reflex. *Nature*, 420(6917):853–859, 2002.

[116] J van Bemmel, M Musen, and J Helder. Handbook of medical informatics. *lavoisier.fr*, Jan 1997. URL `http://www.lavoisier.fr/notice/gbEGORA22NXOFKA2.html`.

[117] Tanja G. M. Vrijkotte, Lorenz J. P. van Doornen, and Eco J. C. de Geus. Effects of Work Stress on Ambulatory Blood Pressure, Heart Rate, and Heart Rate Variability. *Hypertension*, 35(4):880, April 2000. URL `http://hyper.ahajournals.org/cgi/content/full/35/4/880`.

[118] H WANG, M Yu, M Ochani, CA Amella, M Tanovic, S Susarla, JH Li, H WANG, H Yang, and L Ulloa. Nicotinic acetylcholine receptor alpha-7 subunit is an essential regulator of inflammation. *Nature*, 421(6921):384–388, 2002.

[119] David Watson, Lee A Clark, and Auke Tellegen. Development and validation of brief measures of positive and negative affect: The PANAS scales. *Journal of Personality and Social Psychology*, 54(6):1063–1070, 1988. doi: 10.1037/0022-3514.54.6.1063. URL `http://doi.apa.org/getdoi.cfm?doi=10.1037/0022-3514.54.6.1063`.

[120] J Webster. Medical instrumentation: application and design , 2009. URL `http://scholar.google.com/scholar?q=related:NuLi-vZkrbAJ:scholar.google.com/&hl=en&num=30&as_sdt=0,5`.

[121] R WEBSTER. Medical instrumentation sm 3e. *lavoisier.fr*, 1997. URL `http://www.lavoisier.fr/notice/frLWO6A2LARRWLKO.html`.

[122] S Wendelken, S McGrath, M Akay, and G Blike. Using a forehead reflectance pulse oximeter to detect changes in sympathetic tone. *Engineering in Medicine and Biology Society*, Jan 2004. URL `http://ieeexplore.ieee.org/xpls/abs_all.jsp?arnumber=1403158`.

[123] T M A Wilkinson. Early Therapy Improves Outcomes of Exacerbations of Chronic Obstructive Pulmonary Disease. *American Journal of Respiratory and Critical Care Medicine*, 169(12):1298–1303, April 2004. doi: 10.1164/rccm.200310-1443OC. URL `http://ajrccm.atsjournals.org/cgi/doi/10.1164/rccm.200310-1443OC`.

[124] F Wilson, A Macleod, and P Barker. The potential variations produced by the heart beat at the apices of einthoven's triangle. *American Heart Journal*, Jan 1931. URL `http://linkinghub.elsevier.com/retrieve/pii/S0002870331904110`.

[125] Writing Group Members, W Rosamond, K Flegal, K Furie, A Go, K Greenlund, N Haase, S M Hailpern, M Ho, V Howard, B Kissela, S Kittner, D Lloyd-Jones, M McDermott, J Meigs, C Moy, G Nichol, C O'Donnell, V Roger, P Sorlie, J Steinberger,

T Thom, M Wilson, Y Hong, and for the American Heart Association Statistics Committee and Stroke Statistics Subcommittee. Heart Disease and Stroke Statistics–2008 Update: A Report From the American Heart Association Statistics Committee and Stroke Statistics Subcommittee. *Circulation*, 117(4):e25–e146, January 2008. doi: 10.1161/CIRCULATIONAHA.107.187998. URL `http://circ.ahajournals.org/cgi/doi/10.1161/CIRCULATIONAHA.107.187998`.

[126] Writing Group Members, D Lloyd-Jones, R Adams, M Carnethon, G De Simone, T B Ferguson, K Flegal, E Ford, K Furie, A Go, K Greenlund, N Haase, S Hailpern, M Ho, V Howard, B Kissela, S Kittner, D Lackland, L Lisabeth, A Marelli, M McDermott, J Meigs, D Mozaffarian, G Nichol, C O'Donnell, V Roger, W Rosamond, R Sacco, P Sorlie, R Stafford, J Steinberger, T Thom, S Wasserthiel-Smoller, N Wong, J Wylie-Rosett, Y Hong, and for the American Heart Association Statistics Committee and Stroke Statistics Subcommittee. Heart Disease and Stroke Statistics–2009 Update: A Report From the American Heart Association Statistics Committee and Stroke Statistics Subcommittee. *Circulation*, 119(3):e21–e181, January 2009. doi: 10.1161/CIRCULATIONAHA.108.191261. URL `http://circ.ahajournals.org/cgi/doi/10.1161/CIRCULATIONAHA.108.191261`.

[127] Writing Group Members, V L Roger, A S Go, D M Lloyd-Jones, E J Benjamin, J D Berry, W B Borden, D M Bravata, S Dai, E S Ford, C S Fox, H J Fullerton, C Gillespie, S M Hailpern, J A Heit, V J Howard, B M Kissela, S J Kittner, D T Lackland, J H Lichtman, L D Lisabeth, D M Makuc, G M Marcus, A Marelli, D B Matchar, C S Moy, D Mozaffarian, M E Mussolino, G Nichol, N P Paynter, E Z Soliman, P D Sorlie, N Sotoodehnia, T N Turan, S S Virani, N D Wong, D Woo, M B Turner, on behalf of the American Heart Association Statistics Committee and Stroke Statistics Subcommittee, and On behalf of the American Heart Association Statistics Committee and Stroke Statistics Subcommittee. Heart Disease and Stroke Statistics–2012 Update: A Report From the American Heart Association. *Circulation*, 125(1):e2–e220, January 2012. doi: 10.1161/CIR.0b013e31823ac046. URL `http://circ.ahajournals.org/cgi/doi/10.1161/CIR.0b013e31823ac046`.

[128] A Yadollahi and Z. Moussavi. Acoustic obstructive sleep apnea detection. *Engineering in Medicine and Biology Society, 2009. EMBC 2009. Annual International Conference of the IEEE*, pages 7110–7113, 2009. URL `http://ieeexplore.ieee.org/xpls/abs_all.jsp?arnumber=5332870`.

[129] CM Yu, L Wang, E Chau, RHW Chan, SL Kong, MO Tang, J Christensen, RW Stadler, and CP Lau. Intrathoracic impedance monitoring in patients with heart failure: correlation with fluid status and feasibility of early warning preceding hospitalization. *Circulation*, 112(6): 841, 2005.

[130] S Zlochiver, M Radai, D Barak-Shinar, and T Ben. Monitoring lung resistivity changes in CHF patients using bio-impedance technique. *Congest. Heart* ..., 2005. URL `http://www.cardio-inspect.com/chf_journal.pdf`.

[131] S Zlochiver, M Arad, M Radai, and D Barak-Shinar. A portable bio-impedance system for monitoring lung resistivity. *Medical Engineering and* ..., 2007. URL `http://linkinghub.elsevier.com/retrieve/pii/S1350453306000427`.

Appendix A

DOSFS Patch

```
--- dosfs.c.bak 2008-01-14 00:26:10.000000000 -0800
+++ dosfs.c 2008-07-29 00:48:45.000000000 -0700
@@ -8,8 +8,12 @@
   You cannot re-copyright or restrict use of the code as released by Lewin Edwards.
  */

+#include "common.h"
 #include <string.h>
 #include <stdlib.h>
+#include "fat.h"
+
+#define div(a,b) ldiv(a,b)

 #include "dosfs.h"

@@ -24,7 +28,7 @@
  */
 uint32_t DFS_GetPtnStart(uint8_t unit, uint8_t *scratchsector, uint8_t pnum, uint8_t *pactive,
      uint8_t *pptype, uint32_t *psize)
 {
- uint32_t result;
+ uint32_t result=0;
  PMBR mbr = (PMBR) scratchsector;

  // DOS ptable supports maximum 4 partitions
@@ -69,7 +73,9 @@
  PLBR lbr = (PLBR) scratchsector;
  volinfo->unit = unit;
  volinfo->startsector = startsector;
-
+#ifdef DEBUG_DOSFS
+          printf("DFS_GetVolInfo\r\n");
+#endif
  if(DFS_ReadSector(unit,scratchsector,startsector,1))
    return DFS_ERRMISC;

@@ -106,7 +112,7 @@

  // tag: OEMID, refer dosfs.h
  //     memcpy(volinfo->system, lbr->ebpb.ebpb32.system, 8);
-//     volinfo->system[8] = 0;
+//     volinfo->system[8] = 0;
  }
  else {
    memcpy(volinfo->label, lbr->ebpb.ebpb.label, 11);
@@ -114,7 +120,7 @@

  // tag: OEMID, refer dosfs.h
```

```
 //     memcpy(volinfo->system, lbr->ebpb.ebpb.system, 8);
-//     volinfo->system[8] = 0;
+//     volinfo->system[8] = 0;
   }

   // note: if rootentries is 0, we must be in a FAT32 volume.
@@ -161,8 +167,11 @@
  */
 uint32_t DFS_GetFAT(PVOLINFO volinfo, uint8_t *scratch, uint32_t *scratchcache, uint32_t cluster)
 {
- uint32_t offset, sector, result;
+ uint32_t offset=0, sector=0, result=0;

+#ifdef DEBUG_DOSFS
+        printf("DFS_GetFAT\r\n");
+#endif
   if (volinfo->filesystem == FAT12) {
     offset = cluster + (cluster / 2);
   }
@@ -256,7 +265,10 @@
  */
 uint32_t DFS_SetFAT(PVOLINFO volinfo, uint8_t *scratch, uint32_t *scratchcache, uint32_t cluster, uint32_t new_contents)
 {
- uint32_t offset, sector, result;
+ uint32_t offset=0, sector=0, result=0;
+#ifdef DEBUG_DOSFS
+ printf("DFS_SetFAT (%lu->%lu)\r\n",cluster,new_contents);
+#endif
   if (volinfo->filesystem == FAT12) {
     offset = cluster + (cluster / 2);
     new_contents &=0xfff;
@@ -366,7 +378,7 @@
     scratch[offset] = (new_contents & 0xff);
     scratch[offset+1] = (new_contents & 0xff00) >> 8;
     result = DFS_WriteSector(volinfo->unit, scratch, *scratchcache, 1);
-    // mirror the FAT into copy 2
+    // mirror the FAT into copy 2 - XXX
     if (DFS_OK == result)
       result = DFS_WriteSector(volinfo->unit, scratch, (*scratchcache)+volinfo->secperfat, 1);
   }
@@ -428,6 +440,11 @@
 uint32_t DFS_GetFreeFAT(PVOLINFO volinfo, uint8_t *scratch)
 {
   uint32_t i, result = 0xffffffff, scratchcache = 0;
+
+
+#ifdef DEBUG_DOSFS
+         printf("DFS_GetFreeFAT\r\n");
+#endif

   // Search starts at cluster 2, which is the first usable cluster
   // NOTE: This search can't terminate at a bad cluster, because there might
@@ -445,6 +462,7 @@
 /*
   Open a directory for enumeration by DFS_GetNextDirEnt
   You must supply a populated VOLINFO (see DFS_GetVolInfo)
+        ** you must also make sure dirinfo->scratch is valid in the dirinfo you pass it** //reza
   The empty string or a string containing only the directory separator are
   considered to be the root directory.
   Returns 0 OK, nonzero for any error.
@@ -453,7 +471,9 @@
 {
   // Default behavior is a regular search for existing entries
   dirinfo->flags = 0;
-
+#ifdef DEBUG_DOSFS
```

```
+         printf("DFS_OpenDir\r\n");
+#endif
  if (!strlen((char *) dirname) || (strlen((char *) dirname) == 1 && dirname[0] == DIR_SEPARATOR)
      ) {
    if (volinfo->filesystem == FAT32) {
      dirinfo->currentcluster = volinfo->rootdir;
@@ -562,12 +582,15 @@
 {
  uint32_t tempint; // required by DFS_GetFAT

+#ifdef DEBUG_DOSFS
+         printf("DFS_GetNext\r\n");
+#endif
  // Do we need to read the next sector of the directory?
  if (dirinfo->currententry >= SECTOR_SIZE / sizeof(DIRENT)) {
    dirinfo->currententry = 0;
    dirinfo->currentsector++;

-   // Root directory; special case handling
+   // Root directory; special case handling
    // Note that currentcluster will only ever be zero if both:
    // (a) this is the root directory, and
    // (b) we are on a FAT12/16 volume, where the root dir can't be expanded
@@ -588,7 +611,7 @@
         if ((dirinfo->currentcluster >= 0xff7 &&  volinfo->filesystem == FAT12) ||
           (dirinfo->currentcluster >= 0xfff7 &&  volinfo->filesystem == FAT16) ||
           (dirinfo->currentcluster >= 0x0ffffff7 &&  volinfo->filesystem == FAT32)) {
-
+
             // We are at the end of the directory chain. If this is a normal
             // find operation, we should indicate that there is nothing more
             // to see.
@@ -641,8 +664,10 @@
  */
 uint32_t DFS_GetFreeDirEnt(PVOLINFO volinfo, uint8_t *path, PDIRINFO di, PDIRENT de)
 {
- uint32_t tempclus,i;
-
+ uint32_t tempclus=0,i=0;
+#ifdef DEBUG_DOSFS
+         printf("DFS_GetFreeDirEnt\r\n");
+#endif
  if (DFS_OpenDir(volinfo, path, di))
    return DFS_NOTFOUND;

@@ -713,7 +738,10 @@
  uint8_t *p;
  DIRINFO di;
  DIRENT de;
-
+         uint32_t temp;
+#ifdef DEBUG_DOSFS
+         printf("DFS_OpenFile\r\n");
+#endif
  // larwe 2006-09-16 +1 zero out file structure
  memset(fileinfo, 0, sizeof(FILEINFO));

@@ -793,7 +821,7 @@
  // At this point, we KNOW the file does not exist. If the file was opened
  // with write access, we can create it.
  if (mode & DFS_WRITE) {
-   uint32_t cluster, temp;
+   uint32_t cluster;

    // Locate or create a directory entry for this file
    if (DFS_OK != DFS_GetFreeDirEnt(volinfo, tmppath, &di, &de))
@@ -870,11 +898,13 @@
  */
```

```
 uint32_t DFS_ReadFile(PFILEINFO fileinfo, uint8_t *scratch, uint8_t *buffer, uint32_t *
     successcount, uint32_t len)
 {
- uint32_t remain;
+ uint32_t remain=0;
  uint32_t result = DFS_OK;
- uint32_t sector;
- uint32_t bytesread;
-
+ uint32_t sector=0;
+ uint32_t bytesread=0;
+#ifdef DEBUG_DOSFS
+        printf("DFS_ReadFile\r\n");
+#endif
  // Don't try to read past EOF
  if (len > fileinfo->filelen - fileinfo->pointer)
    len = fileinfo->filelen - fileinfo->pointer;
@@ -976,8 +1006,11 @@
  */
 void DFS_Seek(PFILEINFO fileinfo, uint32_t offset, uint8_t *scratch)
 {
- uint32_t tempint;
-
+    uint32_t tempint;
+ uint16_t endcluster=0;  //canny/reza 5/7 fixed
+#ifdef DEBUG_DOSFS
+        printf("DFS_Seek\r\n");
+#endif
  // larwe 9/16/06 bugfix split case 0a/0b and changed fallthrough handling
  // Case 0a - Return immediately for degenerate case
  if (offset == fileinfo->pointer) {
@@ -1006,8 +1039,7 @@

  // Case 3 - Seeking forwards
  // Note _intentional_ fallthrough from Case 2 above
-
- // Case 3a - Seek size does not cross cluster boundary -
+ // Case 3a - Seek size does not cross cluster boundary -
  // very simple case
  // larwe 9/16/06 changed .rem to .quot in both div calls, bugfix
  if (div(fileinfo->pointer, fileinfo->volinfo->secperclus * SECTOR_SIZE).quot ==
@@ -1022,9 +1054,9 @@

    // seek by clusters
    // larwe 9/30/06 bugfix changed .rem to .quot in both div calls
-   while (div(fileinfo->pointer, fileinfo->volinfo->secperclus * SECTOR_SIZE).quot !=
-     div(fileinfo->pointer + offset, fileinfo->volinfo->secperclus * SECTOR_SIZE).quot) {
-
+               // canny/reza 5/7  added endcluster related code
+               endcluster = div(fileinfo->pointer + offset, fileinfo->volinfo->secperclus *
     SECTOR_SIZE).quot;
+               while (div(fileinfo->pointer, fileinfo->volinfo->secperclus * SECTOR_SIZE).quot
     !=endcluster) {
      fileinfo->cluster = DFS_GetFAT(fileinfo->volinfo, scratch, &tempint, fileinfo->cluster);
      // Abort if there was an error
      if (fileinfo->cluster == 0x0ffffff7) {
@@ -1049,8 +1081,11 @@
  PDIRENT de = (PDIRENT) scratch;
  FILEINFO fi;
  uint32_t cache = 0;
- uint32_t tempclus;
+ uint32_t tempclus = 0;

+#ifdef DEBUG_DOSFS
+        printf("DFS_UnlinkFile\r\n");
+#endif
  // DFS_OpenFile gives us all the information we need to delete it
  if (DFS_OK != DFS_OpenFile(volinfo, path, DFS_READ, scratch, &fi))
```

```
    return DFS_NOTFOUND;
@@ -1084,10 +1119,13 @@
  */
 uint32_t DFS_WriteFile(PFILEINFO fileinfo, uint8_t *scratch, uint8_t *buffer, uint32_t *
     successcount, uint32_t len)
 {
- uint32_t remain;
+ uint32_t remain=0;
  uint32_t result = DFS_OK;
- uint32_t sector;
- uint32_t byteswritten;
+ uint32_t sector=0;
+ uint32_t byteswritten=0;
+#ifdef DEBUG_DOSFS
+        printf("DFS_WriteFile\r\n");
+#endif

  // Don't allow writes to a file that's open as readonly
  if (!(fileinfo->mode & DFS_WRITE))
```

Appendix B

Impedance Plethysmography Circuits

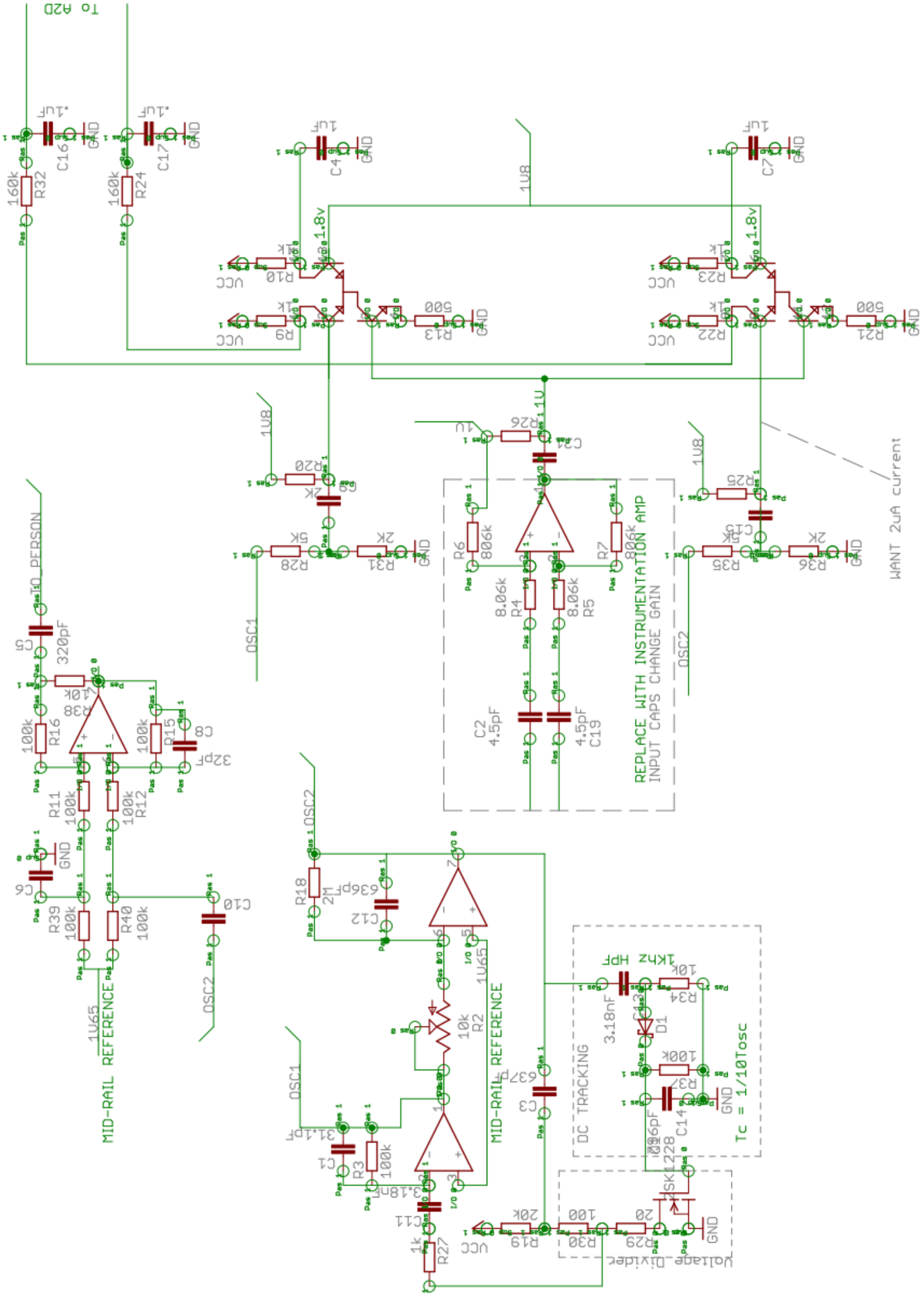

Figure B.1: Analog Oscillator and Demodulator

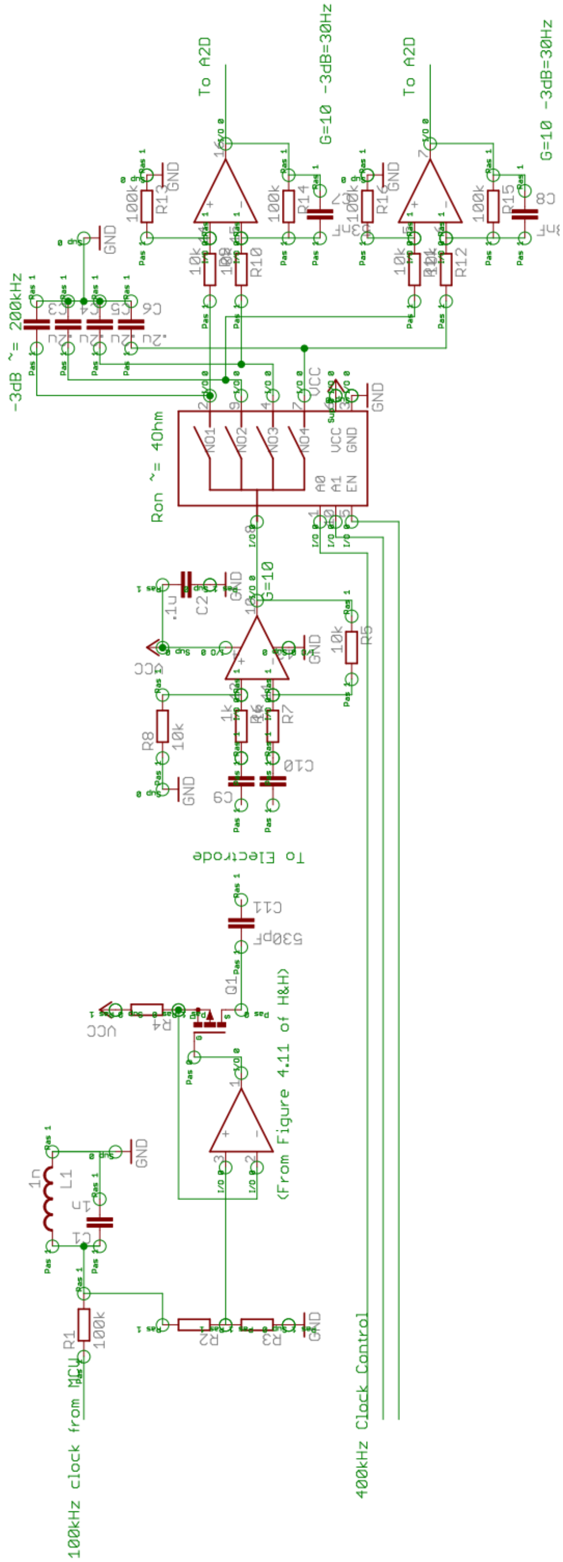

Figure B.2: Digital Oscillator and Demodulator

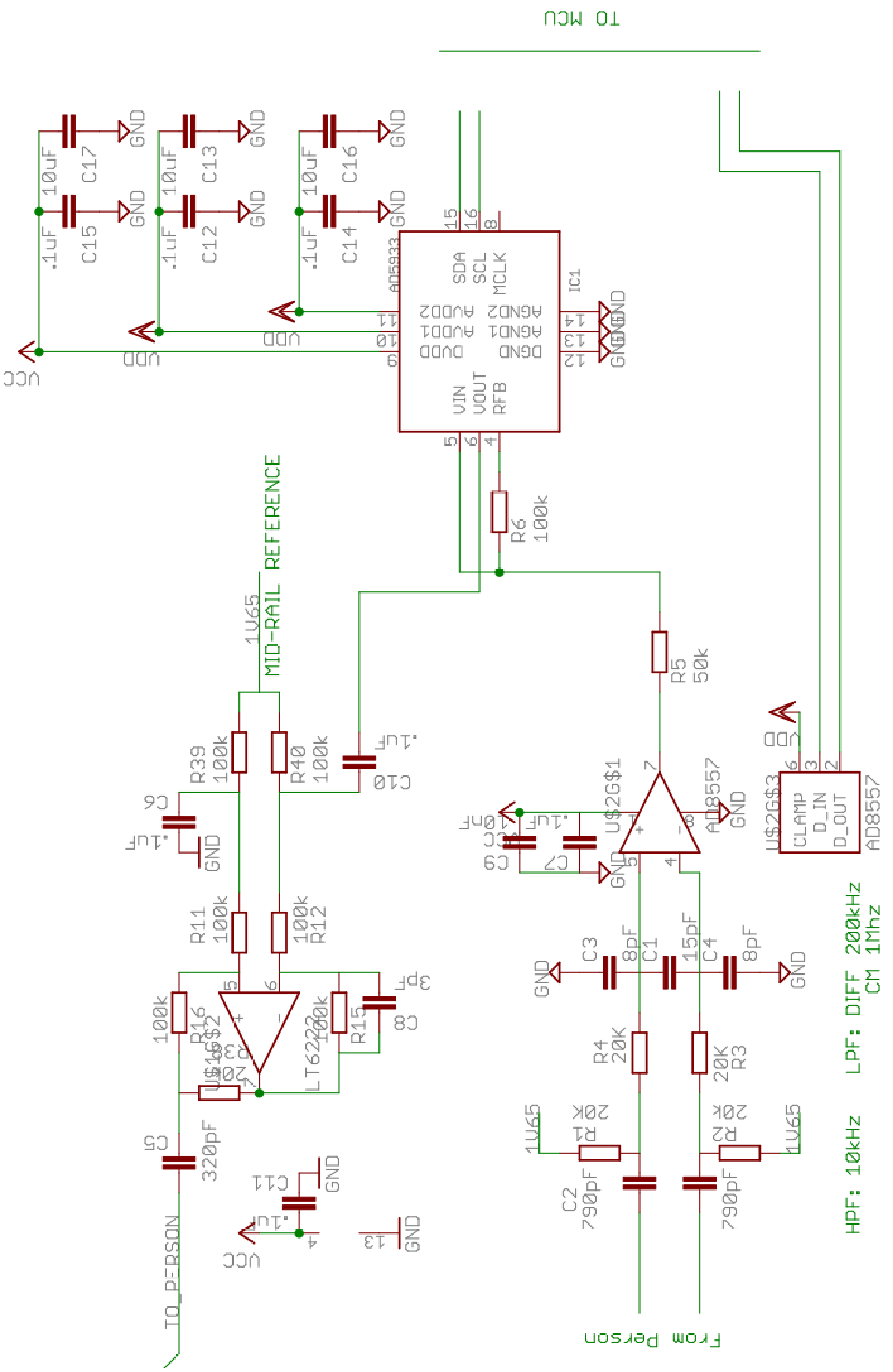

Figure B.3: Dedicated Impedance Measurement Integrated Circuit

]

Appendix C

Radio-Frequency Interference (FRI) Filter

An RFI filter (figure C.1) works by low pass filtering both the differential and common mode signals to an amplifier. The differential and common-mode bandwidth is equal to [63]

$$BW_{differential} = \frac{1}{2\pi(2R_1C_2 + R_1C_1)}$$

$$BW_{common\,mode} = \frac{1}{2\pi(2R_1C_2 + R_1C_1)}$$

Additionally, the following considerations must be made:

- The Johnson noise from the resistor (R_1) must be lower than the noise generated by the amplifier. The noise at room temperature for a range of resistance values is plotted in figure C.2.
- The value for C_1should be 10% the value of C_2. This sets the common mode bandwidth which should be <10% of the instrumentation amplifier's bandwidth at unity gain.

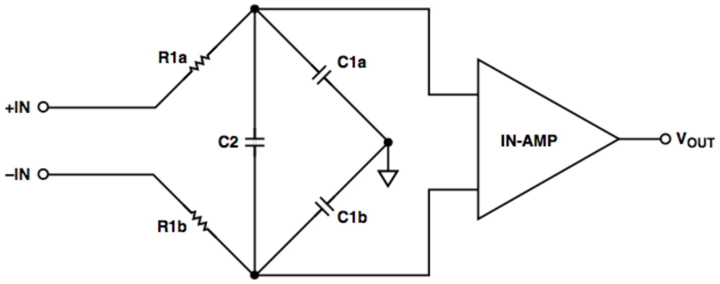

Figure C.1: Radio frequency interference filter. From [63]

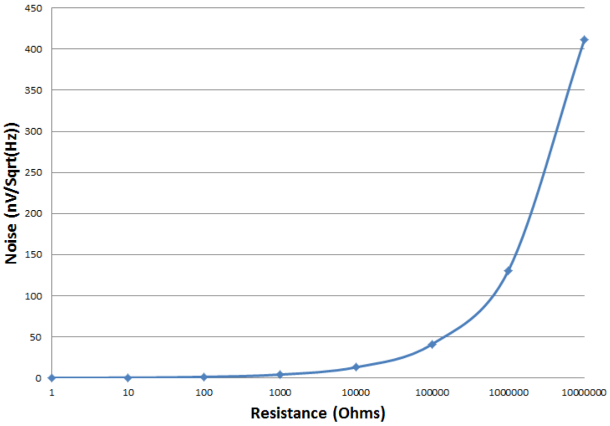

Figure C.2: Johnson Noise for a range of resistance values